Integration of Remote Sensing, Field Observations and Modelling for Ecohydrological Studies in Sonora, Mexico

by

Luis A. Méndez-Barroso

A Dissertation Presented in Partial Fulfillment
of the Requirements for the Degree
Doctor of Philosophy

Approved June 2014 by the
Graduate Supervisory Committee:

Enrique R. Vivoni, Chair
Benjamin L. Ruddell
Enrico A. Yépez
Osvaldo E. Sala
Philip R. Christensen
Kelin X. Whipple

ARIZONA STATE UNIVERSITY

December 2014

ABSTRACT

Ecohydrological responses to rainfall in the North American monsoon (NAM) region lead to complex surface-atmosphere interactions. In early summer, it is expected that soil properties and topography act as primary controls in hydrologic processes. Under the presence of strongly dynamic ecosystems, catchment hydrology is expected to vary substantially in comparison to other semiarid areas, affecting our understanding of ecohydrological processes and the parameterization of predictive models. A large impediment toward making progress in this field is the lack of spatially extensive observational data. As a result, it is critical to integrate numerical models, remote sensing observations and ground data to understand and predict ecohydrological dynamics in space and time, including soil moisture, evapotranspiration and runoff generation dynamics.

In this thesis, a set of novel ecohydrological simulations that integrate remote sensing and ground observations were conducted at three spatial scales in a semiarid river basin in northern Sonora, Mexico. First, single site simulations spanning several summers were carried out in two contrasting mountain ecosystems to predict evapotranspiration partitioning. Second, a catchment-scale simulation was conducted to evaluate the effects of spatially-variable soil thickness and textural properties on water fluxes and states during one monsoon season.

Finally, a river basin modeling effort spanning seven years was applied to understand interannual variability in ecohydrological dynamics. Results indicated that ecohydrological simulations with a dynamic representation of vegetation greening tracked well the seasonal evolution of observed evapotranspiration and soil moisture at two measurement locations. A switch in the dominant component of evapotranspiration from soil evaporation to plant transpiration was observed for each ecosystem, depending on the timing and magnitude of vegetation greening. Furthermore, spatially variable soil thickness affects subsurface flow while soil texture controls patterns of surface soil moisture and evapotranspiration during the transition from dry to wet conditions. Finally, the ratio of transformation of precipitation into evapotranspiration (ET/P) and run off (Q/P) changed in space and time as summer monsoon progresses. The results of this research improve the understanding of the ecohydrology of NAM region, which can be useful for developing sustainable watershed management plans in the face of anticipated land cover and climate changes.

ACKNOWLEDGMENTS

I would like to thank my advisor Dr. Enrique Vivoni for his support during my Master studies and his guidance during the doctoral research. I would also like to thank my committee members: Professor Kelin Whipple, Professor Phillip Christensen, Professor Osvaldo Sala, Dr. Enrico Yépez and Dr. Benjamin Ruddell. I would like to thank CONACYT (Consejo Nacional de Ciencia y Tecnología) for supporting and funding my doctoral studies, NOAA (National Oceanic and Atmospheric Administration) and NSF (National Science Foundation) for funding my research. Likewise, I would like to thank faculty member that collaborate in the development of this research: Professor Arjun Heimsath, Dr. Sri Saripalli, Dr. Zhihua Wang and Dr. Manoochehr Shirzaei.

I would like to thank the members of my research group (The monsoons) and the grad students of Arizona State University and New Mexico Tech. Furthermore, I want to thank a closed group of people that shares joy, sadness and moments of deep reflections (Los terapeutas). Finally, but not last, the best teachers I ever had in my life (La tropa).

TABLE OF CONTENTS

CHAPTER Page

APPENDIX

LIST OF TABLES

Table Page

Table Page

Table Page

LIST OF FIGURES

Figure Page

Figure Page

Figure Page

Figure Page

CHAPTER 1

INTRODUCTION

The North American Monsoon (NAM) is a meteorological phenomenon that increases the summer rain in a large portion of the Southwestern United States and Northwestern Mexico. Although the NAM largely influences the US, especially the state of Arizona, is largely recognized that it is centered in Northwestern Mexico. The combination of seasonally warm land surfaces in both lowlands and high elevation regions along with moisture supplied by the Gulf of California and the Pacific Ocean forms a monsoon system. This system is defined as a seasonal reversal of pressure and wind patterns, energy and mass transfers (Douglas et al., 1993; Adams and Comrie, 1997). There is a general agreement that the main source of moisture at low levels is the eastern Pacific Ocean and the Gulf of California while moisture at high levels is usually provided by the Gulf of Mexico. There is also a common agreement that a mixing of sources occurs in the Sierra Madre Occidental in western Mexico (Carleton, 1986).

The reversal in atmospheric conditions leads to increase precipitation during the summer. This increase in regional rainfall produces a very remarkable change in vegetation greening with impacts in land surface conditions (Méndez-Barroso et al., 2009; Vivoni et al 2010) However, rainfall events are different depending of the location within the NAM domain, for example, high elevation sites, where evergreen woodlands dominate are characterized by more frequent but less intense rains while low elevation sites, where deciduous ecosystems dominate, experience less frequent but more intense rainfalls (Gochis et al., 2006; Gebremichael et al., 2007).

Therefore, vegetation patterns are strongly linked to differences in soil moisture from elevation patterns. Forzieri et al. (2011); found two main vegetation functional groups closely related to precipitation. One consisted in deciduous ecosystems (semiarid grasslands, subtropical scrublands, tropical dry forest) with high seasonality during a short period of intense greening occurring rapidly after the NAM precipitation onset. The other group consisted in evergreen ecosystems (mountain woodlands and conifer forest) with more muted seasonality during a prolonged period of moderate greenness that it is delayed with respect to monsoon onset.

Nowadays, it is well recognized the effect of vegetation on the energy and water balance of the North American Monsoon region. Vegetation can influence heat fluxes, momentum and energy on the land surface. Furthermore, vegetation plays a great role in the partition of energy into sensible and latent, and also by affecting surface albedo and roughness (Watts et al., 2007, Richardson et al., 2013). Such changes in surface conditions can lead to feedbacks mechanisms that can enhance or sustain precipitation in the NAM region. For example; Méndez-Barroso and Vivoni (2010) reviewed and explored the theoretical rainfall-vegetation feedback mechanisms of Eltahir (1998) and Brunsell (2006) and found that subtropical vegetation exhibited large shifts in land surface variables (such as albedo, land surface temperature and NDVI) that could promote vegetation-rainfall feedback only if sunny conditions persist.

Despite the recognition of vegetation in affecting the seasonality of water and energy fluxes in the NAM region, more observations or model predictions are required to test the influence of vegetation on the climatology of the NAM system. To date, only few studies have explored the role of vegetation in rainfall-feedback mechanism in the region with diverse results, e.g., Dominguez et al.,(2008) found that tropical dry forest supported most of the regional evapotranspiration (ET) and enhanced precipitation recycling in the NAM region. Furthermore, continental soil moisture contributions to NAM precipitation were stronger when large scale moisture advection decreases and evaporation provides the moisture to the lower atmosphere enhancing precipitation. Conversely, Notaro and Gutzler (2012) found that a reduction of 0.2 in vegetation cover fraction over the NAM region had considerable impact in surface radiation budget.

Main findings include a decrease in latent heat, increase in upward long-wave radiation and downward shortwave radiation, no considerable changes in albedo and a monsoon was shifted to earlier onset in the US with largest feedback to the atmosphere found in woody vegetation. Clearly, the region requires further studies on the influence of the vegetation on the NAM system. To achieve this, more observations and modeling efforts are required in the NAM domain to understand the temporal and spatial variability of ecohydrological processes especially in Northwestern Mexico.

Another key role of vegetation is the partition of surface evapotranspiration into plant transpiration, soil evaporation and in some cases, evaporation from intercepted water by the canopy. There are many methods and techniques to estimate the fraction of transpiration (T) to total moisture flux from the surface. For example, some methods rely on hydrometric measurement such as sap flow to estimate transpiration rate (Cavanaugh et al., 2011). More recent methods analyzed the isotopic composition of liquid water and water vapor (Yépez et al., 2003; Sutanto et al., 2012; Jasechko et al., 2013). Last approach involves the use of land surface models (Oleson et al., 2004; Dirmeyer et al., 2006) to estimate the components of evapotranspiration from turbulent transfer, moisture limitations and plant physiology. The fraction of transpiration to total ET widely varies among methods but the isotopic method tends to estimate higher transpiration fractions than the other methods. Studies of ET partition encompassed a wide range of ecosystems but only a few studies have addressed in semiarid areas (Reynolds et al., 2000; Scott et al., 2006; Moran et al., 2009).

Under the presence of strongly dynamics ecosystems in this region, catchment hydrology is expected to vary a lot in comparison with other semiarid areas, affecting the understanding of ecohydrological processes and the parameterization of predictive models. However, a large impediment in making progress in hydrological modeling in the region is the lack of spatially-extensive observational datasets and bad representation of basin characteristics (Gochis et al., 2010; Vivoni et al., 2010). Currently, Mexico's National Weather Service (Sevicio Meterológico Nacional, SMN), the Federal Agency in charge of collection and record of historical meteorological data, has 4500 climate stations, 94 automatic meteorological stations and 12 radars nationwide. However, Because Federal budget cuts, only 27% of the stations collect data continuously (Perevochtchivoka, 2013). The National Water Commission (Comision Nacional del Agua, CONAGUA) the Mexican Federal Agency in charge of collecting water data. In 2008, CONAGUA had 499 stream gauges and 211 hydroclimatic stations nationwide. However, because of critical financial and political situation, a large number of stations are not operational today. Notwithstanding, both Federal hydrometeorological networks share common problems such as: heterogeneous, inaccurate and inaccessible data; non-continuous time series due to changes in state and federal governments policies and usually the information is inconsistent when comparing each other agencies ((Perevochtchivoka, 2011). Lack of long-term ground observations in the NAM region within Mexico and it is necessary to have complete time series of climatic data in order to carry out accurate studies (Brunet, 2010)

Furthermore; the effect of soil properties distribution such as soil texture or soil depth in models uncertainty is poorly understood (Weiler et al., 2006; Lanni et al., 2013). Basin representation can be improved by incorporating seasonal land surface changes and realistic subsurface and surface topography into hydrological model framework. One way to account for land surface changes is by incorporating vegetation dynamics, albedo seasonality and subsurface topography such as soil thickness (Gochis et al., 2010).

Poor understanding of hydrological processes in the NAM region leads to poor model parameterization. Global land surface models in the NAM region have shown limitations in the North American Monsoon region to properly simulate surface energy and water fluxes (Unland et al., 1999; Vivoni et al., 2008). Conversely, a better understanding of the complex interactions and feedbacks between seasonal shifts in vegetation greening and soil moisture with temporal spatial variability of water and energy fluxes can help us to design better water management policies and planning. Nowadays, water management has been dominated by a mechanistic-predatory approach with severe degradation of the biota that is the most important and dynamic regulatory component of the water cycle. For this reason, there is an urgent need to incorporate ecosystem properties as management tool. Ecohydrology, the study of functional interrelations between hydrology and the plants at catchment scale, is a new approach to develop sustainable water management (Zalewski, 2000). Furthermore, ecohydrology offers a scientific basis for designing more holistic and integrative approaches better suited to the complexity of environmental problems at the interaction between hydrology and ecology (Wagener et al., 2010; Wilcox at al., 2010). However, more research is required in semiarid areas with emphasis on those with monsoonal regime exhibiting complex interactions between vegetation and hydrological processes. In this context, this research work is an important contribution to the understanding of ecohydrological processes within the NAM region.

Remote sensing is a tool that can be used to understand land surface conditions at basin or regional scales. Remote sensing data generally have better geographical coverage than in situ observations that generally are based upon point sources. For this reason, remote sensing has opened a new opportunity for the development of fully distributed hydrologic and land-surface models. Remote sensing and hydrologic modeling are two key approaches to evaluate and predict hydrologic processes. However, due to the complexity of the land surface with several interconnected processes is not possible that one single waveband can effectively explain them. For this reason is essential to use information from several sources in order to have a better representation of basin characteristics or processes

In general, remote sensing data can be applied to hydrologic or land surface modeling through three different strategies. The first approach includes the use of remote sensing data as model inputs. Usually remote sensing provides input information into models such as digital elevation model and land cover. Furthermore, distributed remote sensing data can be used for forcing hydrologic models (Andersen et al., 2002).

The second approach includes the application of remote sensing data for parameter estimation. Most of hydrological models contain conceptual parameters that are hard to measure in reality. Therefore, these parameters need to be calibrated in order to have a good match between estimated and observed variables. The third strategy involves state estimation that it is also known as data assimilation. Data assimilation refers to the process to constrain the model simulations with observations to improve estimation of the state variable. This research work used a multi-platform remote sensing approach integrated with scarce ground observations to characterize land surface properties in novel ways, including soil classes, surface and subsurface topography and seasonal changes in vegetation conditions. Secondly, remote sensing-based variables and basin topography was incorporated to ecohydrological simulations at different scales to estimate water and energy fluxes. Finally, some remote sensing observations were used to calibrate model estimations.

Recently, incorporation of vegetation dynamics in hydrological simulations has made a big improvement in representation of basin conditions (Droogers and Kite, 2002). Leaf Area Index

(LAI) is one of the critical variables linked to vegetation dynamics. This variable is directly linked to intercepted rainfall by canopy and evapotranspiration. Over the last decade, estimated LAI from the Moderate Resolution Imaging Spectroradiometer (MODIS) has been utilized as one of the inputs that account for vegetation structure and dynamics in hydrological model. The incorporation of MODIS-LAI in hydrological models has improved the estimation of land surface evapotranspiration (ET). There are several examples of successfully incorporation of MODIS-LAI in hydrological modeling (Zhang and Wagehenkel, 2006; Andersen, 2008; Boegh et al., 2009) ranging from natural systems to agricultural fields. However, only few studies have coupled MODIS vegetation indices or LAI in arid or semiarid areas around the world (Vivoni et al., 2010, Mendez-Barroso et al., 2014).

This dissertation includes a set of novel ecohydrological simulation that integrates remote sensing data and ground observations to a semiarid basin in Northwestern Mexico. The mathematical simulations were carried within the domain of the North American Monsoon region at three different spatial scales. In particular, this research focus on the differences between water and energy fluxes among the ecosystems found in a semiarid basin with high response to rainfall pulses. Furthermore, this research evaluates the effect of subsurface topography and spatial distribution of soil properties on water and energy fluxes within the domain of the North American Monsoon. This latter statement has not been deeply explored in hydrological modeling and the uncertainty in computation of fluxes and states with varying properties distribution are poorly understood. Finally, we used the integration of different tools to explore the inter-annual and intra-seasonal variation of hydrological importance variables such as runoff ratio (Q/P) and fraction ET/P at river basin scale. This latter coefficient is considered a proxy of the capacity of the ecosystems found in semiarid basins to return water to the atmosphere, define by other authors as the recycling precipitation ratio. A summary of chapters (2-4) is given in the next section. Each chapter has been prepared and formatted for publication in scientific journals.

1.1 Overview of chapters

Chapter two describes the most important findings in single site hydrological simulations spanning several summer seasons on two contrasting mountain ecosystems to predict evapotranspiration and its partition with the incorporation of dynamic vegetation parameters. The scientific questions for Chapter two are the following:

1. Does the incorporation of vegetation dynamics in modeling tracks the seasonality of observed water fluxes?
2. Does the incorporation of vegetation seasonality help us to understand ET partitioning and its seasonal evolution?

To answer these questions we use a distributed model with the incorporation of vegetation seasonality expressed in model parameters that account for rainfall interception, plant evapotranspiration and partition of energy. Model vegetation parameters are estimating from MODIS products such as leaf area index (LAI), normalized difference vegetation index (NDVI), short wave albedo and fraction of photosynthetic active radiation (fPAR) by applying empirical equations. The hydroecological simulations are focused on the monsoon seasons (June through September) of the years 2004 and 2006 through 2009. The period of simulations include contrasting years in terms of precipitation and vegetation cover allowing to observed differences in water and energy fluxes. We calibrated the model using two eddy-covariance towers for one summer season in two contrasting ecosystems along a mountain front within the NAM region. Model simulations are focused on the capabilities to track site observations by incorporating vegetation seasonality and its effect on ET partitioning.

Ecohydrological simulations tracked well the seasonal evolution of observed *ET* and soil moisture (*SM*). Results suggest that transition from dominant soil evaporation to dominant plant transpiration depends on timing and magnitude of rainfall pulses. Furthermore, partition behaves differently on both ecosystems (Madrean woodland and Sinaloan thornscrub) suggesting differences in water efficiency. For example, in the Sinaloan thornscrub site transpiration was the dominant component of total evapotranspiration while soil evaporation dominates on Madrean woodland. Sinaloan thornscrub follows an intensive water use strategy with a rapid and robust transpiration response to water availability. In contrast, Madrean woodland has delayed and attenuated transpiration, suggesting an extensive water use strategy persisting beyond the North American monsoon.

Chapter three evaluates the effect of spatially variable soil thickness and textural properties on model estimated water fluxes and states during a monsoon season. These set of hydrological simulations are performed at catchment-scale incorporating seasonal vegetation greening. The scientific questions for Chapter three are the following:

1. How large is the impact of variable soil thickness and textural properties on simulated fluxes?
2. How is the spatial representation of these simulated fluxes?

To answer these questions, we utilize the hydrological model Triangulated Irregular Network (TIN)-based Real time Integrated Basin Simulator (tRIBS) to investigate the effect of spatially variable soil thickness and soil textural properties on water fluxes and states. Models simulations allow also investigating the effect on spatial patterns of water fluxes at catchment scale. Our simulations focus on the variability of water fluxes by incorporating three different spatial distribution of soil thickness and three different distribution of soil texture. Distributed soil thickness was estimated using: 1) A linear function between observed soil thickness and local elevation, 2) A linear function between surface slope and observed soil thickness, 3) A multi-linear relation between soil thickness, topographic wetness index (TWI) and surface curvature (Gessler et al., 1995) and 4) the relation between curvature and soil thickness (Heimsath et al., 1999). One novel way to know the spatial distribution of soil textural properties was estimated by using measured radiance at the Advance Spaceborne Thermal Emission and Reflection Radiometer (ASTER) based on the emission properties of different soil classes. We perform a total of twenty-one simulations including uniform soil depth (1.5 m) and uniform soil texture. Results suggest that soil texture exert a strong control in surface soil moisture and the hydrological model is very sensitive to the spatial variation of soil thickness. Soil depressions caused by the high variability in the estimation of soil thickness, especially in the Heimsath and Gessler methods, are the responsible of increasing groundwater fluxes leading to wetter soils and higher evapotranspiration.

Finally, Chapter four describes the inter-annual variability in ecohydrological dynamics by performing a seven-year simulation period on the entire San Miguel River Basin. The scientific questions for Chapter four are the following:

1. How is the spatial and temporal evolution of the run off coefficient in San Miguel basin?
2. Is vegetation cover impacting the variability of runoff and ET?
3. How is the spatial and temporal evolution of the ratio ET/P over the San Miguel Basin?

To answer this question, we used the Triangulated Irregular Network (TIN)-based Real time Integrated Basin Simulator (tRIBS) to evaluate the differences in water fluxes and states among the ecosystems found in the San Miguel Basin. Furthermore, we utilize the hydrological model to explore the temporal and spatial evolution of the run off coefficient (Q/P) and the ratio ET/P which both are a proxy of the capacity of the land surface to support precipitation recycling (Savenije, 1996). Ecohydrological simulations span a period of seven years starting in January 2004 and finishing in December 2010. Results suggest that accounting for incorporation of seasonal vegetation greening allows to see clear differences among ecosystems in water fluxes, for example; grasslands and sparse woodlands to return water to the atmosphere, which suggest that these two ecosystems are important to sustain rainfall within the basin. In general, there is an increasing capacity of the basin to return water tit he atmosphere as ET as summer monsoon progresses as well as produce runoff. Finally, hydrological model allow us to understand regions or ecosystems that highly support the conversion of precipitation into evapotranspiration or runoff. These later statement is very important for the design of water resources management as well as decisions for stakeholders in water use planning.

CHAPTER 2

A MODELING APPROACH REVEALS DIFFERENCES IN EVAPOTRANSPIRATION AND ITS PARTITIONING IN TWO SEMIARID ECOSYSTEMS IN NORTHWEST MEXICO

2.1 Introduction

Vegetation is a key dynamical factor that modifies the water, energy and momentum fluxes occurring at the land surface (e.g., Arora, 2002; Van den Hurk et al., 2003; Vivoni et al., 2008). Plant canopies affect the water balance through rainfall interception and plant water uptake during transpiration, while playing a role in the energy balance through radiation attenuation and modifications of surface roughness and albedo (e.g., Eltahir, 1998; Méndez-Barroso and Vivoni, 2010). Nevertheless, the impact of vegetation greening on land-atmosphere exchanges is not well understood, in particular during seasonal changes induced by radiation or water availability. This problem is exacerbated when plant transpiration (*T*) is lumped with soil evaporation (*E*) and evaporation of intercepted water (*I*) into a single term, evapotranspiration (*ET*), as this mixes vegetation- and soil-mediated processes occurring over disparate temporal and spatial scales. The ability to partition *ET* into its underlying components would improve our understanding of plant water uptake and its feedback to the carbon and water cycle (e.g., Newman et al., 2006; Yépez et al., 2007). To date, only a few studies have addressed *ET* partitioning and consensus has not been achieved across different methodologies on the relative importance of each component, even for similar ecosystems (Reynolds et al., 2000; Stannard and Weltz, 2006; Scott et al., 2006; Moran et al., 2009; Raz-Yaseef et al., 2012; Yang et al., 2013).

One approach for estimating *ET* and its components is through the use of models that incorporate vegetation greening either through prognostic equations (e.g., Kucharik et al., 2006; Lawrence et al., 2007; Ivanov et al., 2008) or via remote sensing observations (e.g., Matsui et al., 2005; Cleugh et al., 2007; Vivoni, 2012). Satellite-derived products, such as the Normalized Difference Vegetation Index (NDVI) and Leaf Area Index (LAI), have been used to provide vegetation parameters for land-atmosphere models instead of the direct simulation of plant processes, at a range of scales from regional to global (Yan et al., 2012). Thus, a first step to include vegetation greening in simulation models has been through comparisons of static and seasonally-varying vegetation parameters. Van den Hurk et al. (2003), for example, conducted climate simulations to investigate the impact of seasonally-varying LAI on evapotranspiration, finding a larger range of values due to increases in summer *ET* and decreases in winter *ET*, as compared to static conditions. Furthermore, Tang et al. (2012) showed that the interannual variability of seasonal (summer) changes in LAI were important to account for when predicting spatiotemporal patterns of evapotranspiration using a hydrologic model, in particular during periods of vegetation green-up. While promising, open questions remain with respect to the seasonal and interannual variations of *ET* and its components and how these are linked to readily-available information about an ecosystem, such as precipitation or vegetation greening. Furthermore, few studies have accounted for the complete set of changes to plant processes (e.g., radiation, interception, transpiration) that simultaneously occur during vegetation greening.

In a recent study, Vivoni (2012) conducted hydrologic simulations using the Triangulated Irregular Network (TIN)-based Real-time Integrated Basin Simulator (tRIBS, Ivanov et al., 2004; Vivoni et al., 2007a) that accounted for seasonal variations in vegetation parameters. The study was focused on an intermediate-sized watershed (~100 km^2) experiencing dramatic vegetation greening during the North American monsoon (NAM). The NAM is a summertime atmospheric circulation occurring in the southwestern U.S. and northwestern Mexico that leads to increased precipitation, soil moisture, evapotranspiration and stream flow in the arid and semiarid areas. A large number and variety of ecosystems respond to the rainy season through biomass production, leading to regional patterns in vegetation greenness (Watts et al., 2007; Méndez-Barroso et al., 2009; Lizárraga-Celaya et al., 2010; Forzieri et al., 2011). Vivoni (2012) found that ecosystem-specific variations in vegetation greening were responsible for the simulated spatiotemporal patterns of *ET* components. For example, subtropical scrubland ecosystems, such as Sinaloan thornscrub (ST), exhibited early greening in the summer season that favored high plant transpiration, whereas oak savanna ecosystems, such as Madrean woodland (MW), had a more delayed and prolonged green-up with sustained plant transpiration into the early fall. However, the focus of Vivoni (2012) on a single summer did not permit an assessment of the interannual variations in evapotranspiration and its partitioning or on the differences among ecosystems.

In this study, we seek to understand how variations in vegetation greening affect *ET* partitioning in two semiarid ecosystems (ST and MW) in northwestern Mexico. By virtue of their organization along semiarid mountain fronts, these ecosystems occupy specific niches related to climate conditions and water availability that also likely occur in other semiarid regions. To do so, we utilize the tRIBS model applied to an eddy covariance tower site in each ecosystem, while accounting for the impact of seasonal greening on the vegetation parameters in the model. For the first time, this approach allows a direct comparison between the ST and MW ecosystems, arranged from intermediate (~600 to 1200 m for ST) to high (~1200 to 1700 m for MW) elevations, in terms of both observations and simulations. Based on data availability, multiple summer periods are studied in each ecosystem to cover a range of seasonal precipitation amounts. We are interested in answering the following questions that are broadly applicable to other ecosystems: How do seasonal variations in vegetation greening in the different ecosystems affect *ET* partitioning? and Do interannual differences in rainfall and vegetation greening affect *ET* and its components? While we focus primarily on *ET*, the surface soil moisture and sensible heat flux are also inspected due to its importance in controlling *ET* rates or serving as a complementary measure of the surface energy balance.

2.2. Methods

2.2.1. Study Region

The study region is located in northern Sonora, Mexico, in a rural, sparsely populated area characterized by north to south trending mountain ranges and valleys that are part of the Sierra Madre Occidental. Ecosystems in the region vary from desert shrublands to conifer pine forests, with a significant proportion of subtropical species (Méndez-Barroso and Vivoni, 2010).

Month or year	*Mean (± 1 std) precipitation [mm]*	
	Sinaloan thornscrub	*Madrean Woodland*
June	28(± 7)	39 (± 21)
July	169 (± 38)	180 (± 113)
August	165 (± 61)	177 (± 59)
September	84 (± 88)	41 (± 12)
2004	278	-
2006	549	-
2007	490	-
2008	519	551
2009	397	321

Table 2.1. Mean Monthly Precipitation and ±1 Monthly Standard Deviation (Std) and Summer Season (JJAS) Precipitation at Sinaloan Thornscrub and Madrean Woodland Sites Over 2004-2009.

Overall, site climate is considered steppe or semiarid (BSh), according to the Köppen-Geiger classification (Peel et al., 2007), characterized by hot, arid conditions and winter temperatures above 0 ºC.

The two study sites are located in the Río San Miguel basin (3796 km^2), which have mean annual precipitation values (±1 standard deviation) ranging from 481 ± 181 mm/yr (Rayón, near ST) to 496 ± 204 mm/yr (Meresichic, near MW), over 1981-2006. Table 2.1 presents the site-specific monthly and summer seasonal precipitation values over the periods with available data. Mean annual air temperatures in the region range from 21.4 ± 6.4 ºC (Rayón, near ST) to 18.9 ± 6.1 ºC (Meresichic, near MW), over 1981-2006. The Sinaloan thornscrub (ST) site is located on top of an alluvial foothill near Rayón (29.74 ºN, 110.54 ºW) at an elevation of 632 m, while the Madrean woodland (MW) site is found on a gentle mountain slope, ~21 km southeast of Meresichic (29.96 ºN, 110.46 ºW) at an elevation of 1314 m. Figure 2.1 depicts the location of the study region and the elevation and ecosystem characteristics of the two sites. Transects A-A’ and B-B’ clearly show how the sites represent intermediate and high elevations along these semiarid mountain fronts (c.f., Vivoni et al., 2007b; 2010). All ecosystems in the region respond by greening to the seasonal precipitation from the NAM extending from July to September and leading to 60-70% of the annual precipitation (Méndez-Barroso et al., 2009).

2.2.2. Field and Remote Sensing Observations

An eddy covariance (EC) tower was deployed at each site in an area of homogeneous vegetation cover within the EC fetch to measure water, energy and carbon fluxes, as well as site meteorology, during the summer season (June 1 to September 30) over multiple years. Figure 2.2 provides details of the characteristics of each site, including a high-resolution (~1 m) terrain model obtained using site surveying and a 1 m satellite image depicting the vegetation patterns. The ST site was installed in 2004 as part of the SMEX04 (Soil Moisture Experiment 2004) experiment (Bindlish et al., 2008) and was operated for summers 2006-2009 as part of this study for five summers of observations. Vegetation at the ST site includes thorny, deciduous trees and shrubs, as well as cacti and succulents, with low amounts of grass cover (see Brown, 1994, for a description of ST). Watts et al. (2007), Méndez-Barroso and Vivoni (2010), Vivoni et al. (2010), Tang et al. (2012) and Tarín et al. (2014) have reported on the EC data at the ST site. On the other hand, the MW site was installed in 2007 and operated in 2008 and 2009 allowing for only two summers (as with ST, the EC system continues to be operated during short periods).

Vegetation at the MW site is primarily oak trees interspersed with grasses and succulents (Brown, 1994). To date, the EC data at the MW site have not been reported on, though Méndez-Barroso et al. (2009) described the precipitation, soil moisture and vegetation at a nearby site, and detailed simulations have not been conducted at the site. Both the ST and MW EC systems form part of a growing network of flux measurements in Mexico (Vargas et al., 2013). Figure 2.3 shows the seasonal evolution of rainfall and surface soil moisture (*SM*, top 10 cm) for the 2004-2009 summers in the ST and MW sites as bi-weekly averages and ±1 standard deviations.

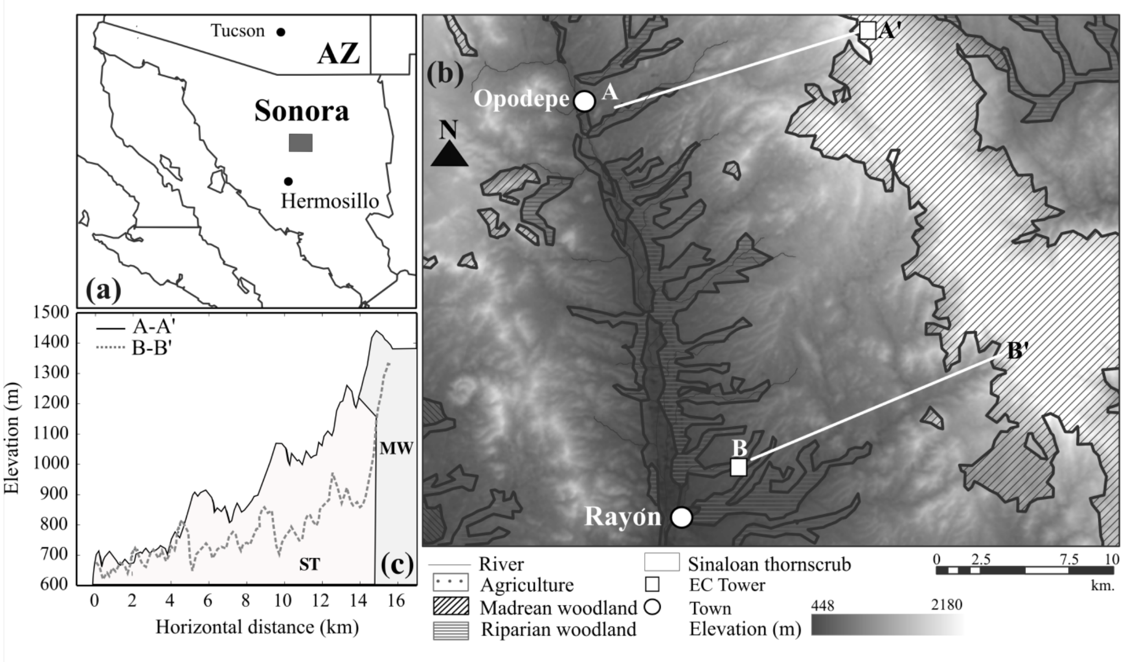

Figure 2.1. (a) Location of the Study Site In Sonora, Mexico. (b) Location of Two Eddy Covariance (EC) Tower Sites and Their Relation to Ecosystem and Topographic Distributions in the Region Note that the Sinaloan Thornscrub is Represented as Transparent. MW is at A' and ST is at B (Square Symbols). (c) Elevation Cross-Sections Along the Mountain Fronts Containing the Two EC Sites With Extents of ST and MW Ecosystems Labeled.

Both EC systems have a standard configuration consisting of a three-dimensional, sonic anemometer (CSAT3, Campbell Scientific, Logan, UT) and an open-path Infrared Gas Analyzer (LI7500, LI-COR, Lincoln, NE) aligned to the dominant wind direction of 225º (Moncrieff et al., 2000). EC sensors were placed at 9 m above ground (installed at 2 m above the canopies). Net shortwave and long-wave radiation were measured (CNR2, Kipp & Zonen, Delft, Netherlands), along with incoming solar radiation (CMP3, Campbell Scientific). Ground heat flux was measured using two soil plates (HFP01SC, Hukseflux, Manorville, NY) placed at 2 cm depth. Site rainfall was measured using a tipping-bucket rain gauge (TB3, Hydrological Services, Sydney, Australia at ST and TR-52USW, Texas Electronic, Dallas, TX at MW), while soil moisture was measured using soil dielectric sensors (Stevens Hydra sensor, Portland, OR) at each site at 5 and 10 cm depths, with MW having additional sensors at 15 and 30 cm. We used here the 5 and 10 cm depth soil moisture sensors due to their greater data availability at both sites. It should be noted that the soil moisture response at MW beyond 10 cm was similar to the shallower sensors (not shown). Sensors were connected to CR5000 data loggers (Campbell Scientific) with the EC sensors operating at 20 Hz and averaging data to 30 min periods. Covariances of vertical wind speed, temperature and water vapor concentration were processed to obtain the sensible (H) and latent heat (λE) flux using EdiRe (University of Edinburgh). Turbulent flux corrections for the EC measurements followed Scott et al. (2004) and included data filtering (i.e., data removal after or during rain events and outliers), the Webb method for density correction (Webb et al., 1980), the quality check method described by Mauder and Foken (2004) and the planar fit as a method of rotation (Wilczak et al., 2001). The planar fit method is deemed appropriate for correcting EC measurements for non-zero mean vertical velocity in the sloping terrain at both sites (Lee et al., 2004), but more markedly at MW (Figure 2.2). Ground heat flux (G) was corrected for heat storage in the upper 2 cm using the change in soil temperature measured by two thermocouples at 2 cm depth (TCAV-L, Campbell Scientific) and the volumetric water content at 5 cm depth (Campbell, 2012). The soil temperature readings from the thermocouples were averaged and then used to calculate the soil heat storage and compute the corrected ground heat flux. Canopy heat storage is expected to be small in short vegetation types (less than 8 meters) and was neglected in this study (Wilson et al., 2002).

Energy balance closure was evaluated for each site using a least squares comparison between turbulent fluxes ($\lambda E + H$) and available energy ($R_n - G$, where R_n is net radiation) and the seasonal energy balance ratio (ENR, defined as the cumulative sums of turbulent fluxes divided by the available energy) obtained for all available summers. The ST site had a slope of 0.75 (± 0.04), an intercept of 16 (± 2) W/m^2, a correlation coefficient (r^2) of 0.93 (± 0.005) and an ENR of 0.83 (± 0.02), while the MW site had a slope of 0.81 (± 0.05), an intercept of 27 (± 18) W/m^2, a correlation coefficient (r^2) of 0.90 (± 0.06) and an ENR of 0.81 (± 0.10), where the errors are computed as interannual standard deviations among the summers.

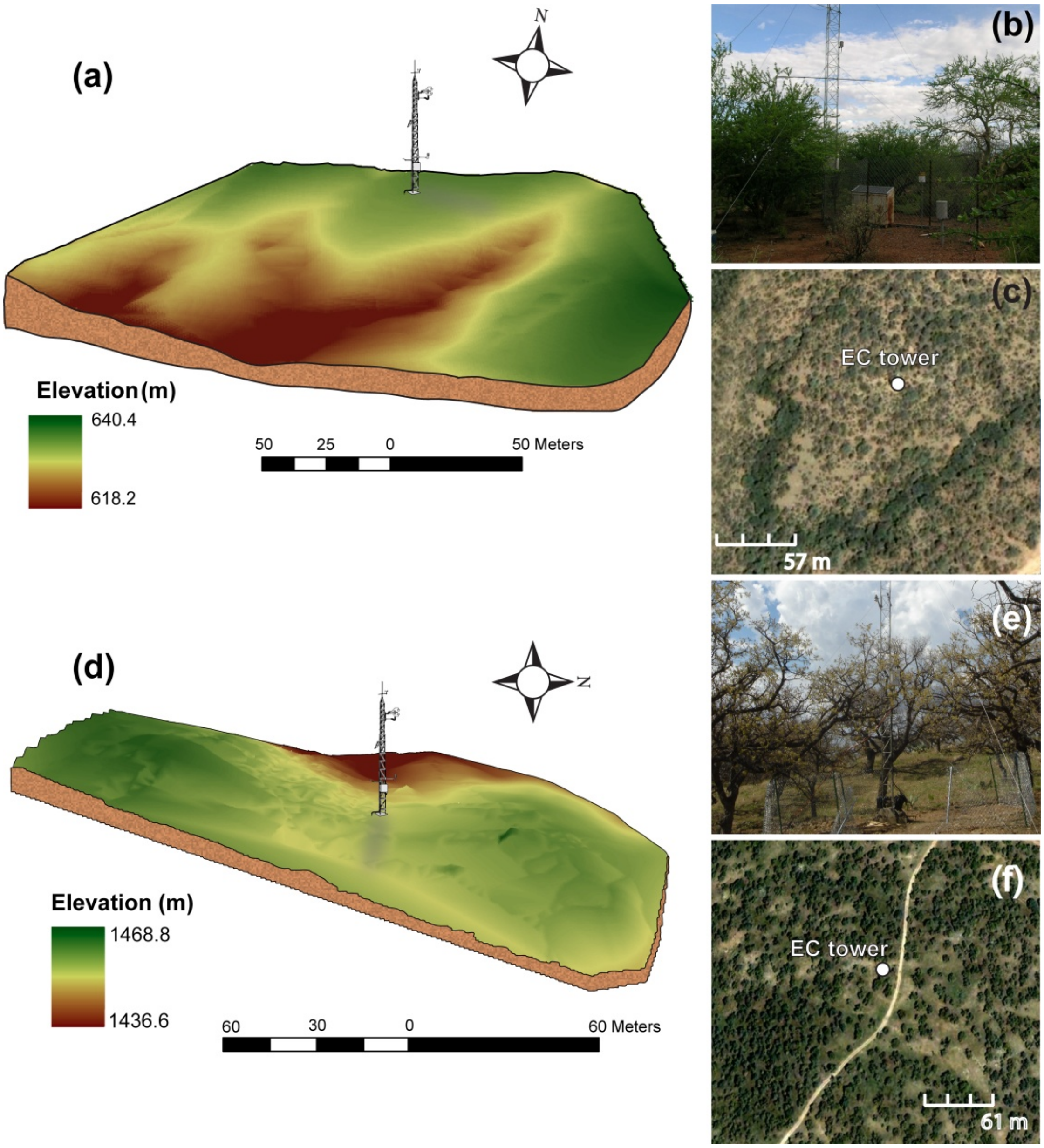

Figure 2.2. Topographic and Vegetation Characteristics at EC Tower Sites. Topographic Survey (a), Tower Photograph (b) and 1 m. IKONOS Image (c) at the Sinaloan Thornscrub Site Near Rayón, Sonora. Topographic Survey (d), Tower Photograph (e) and 1 m. IKONOS Image (f) at the Madrean Woodland, 16.6 km. Northeast of Opodepe, Sonora.

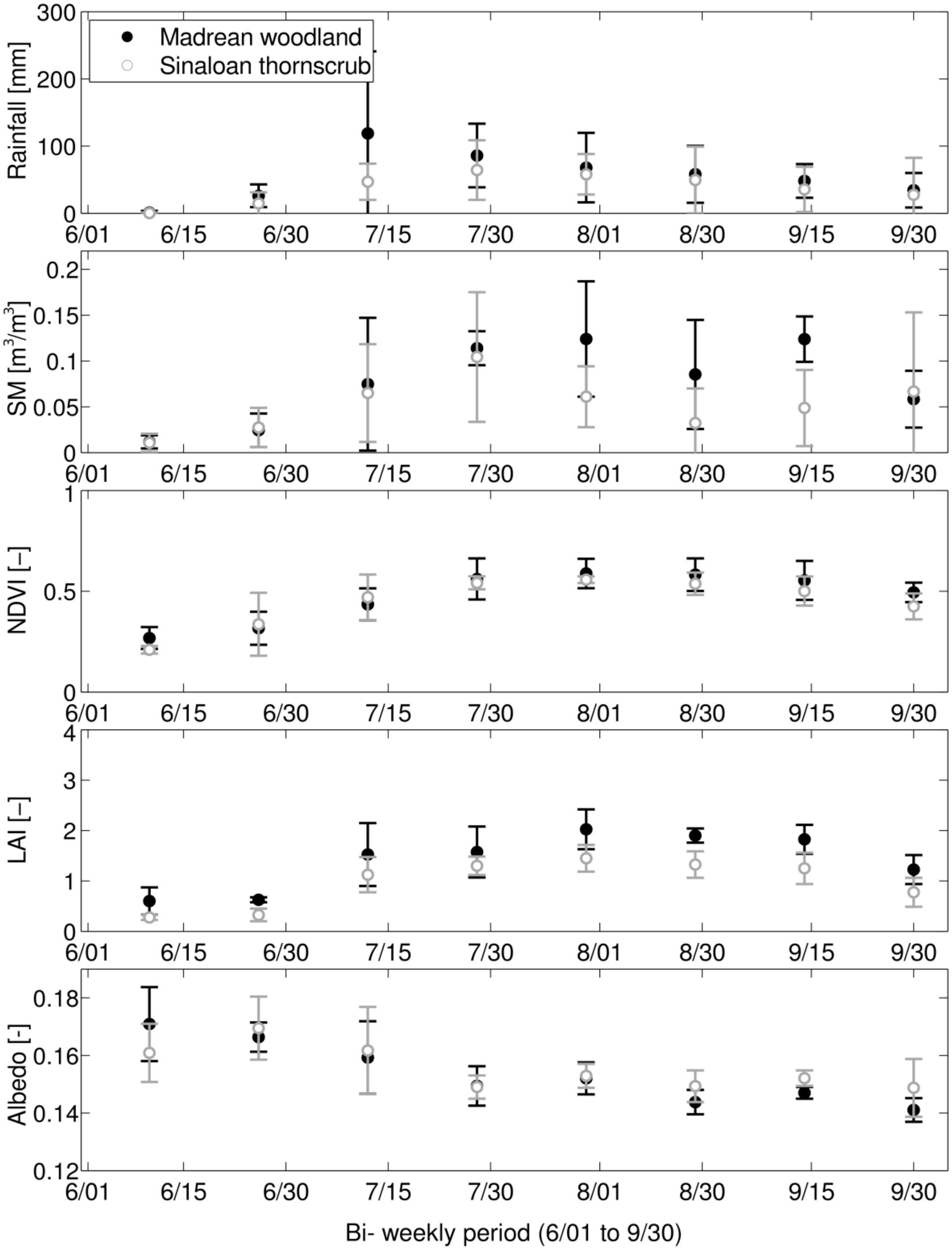

Figure 2.3. Seasonal Evolution of Rainfall, Surface Soil Moisture (*SM*, Top 10 cm), Normalized Difference Vegetation Index (NDVI), Leaf Area Index (LAI) and Albedo Over 2004-2009. Rainfall is Accumulated During Bi-Weekly Intervals, while *SM* is Averaged Over this Period. NDVI, LAI and Albedo Represent 16 Day Composites from MODIS. Symbols Depict Bi-Weekly Averages and Error Bars are ±1 Standard Deviations Across All Years.

Reported values for MW were affected by a net radiometer malfunction in June 2009, after which a replacement sensor led to a large improvement in the energy balance closure (i.e., increase in the slope from 0.60 to 0.81). These metrics are close to values reported for Wilson et al. (2002) for the energy balance closure at FLUXNET sites and as such we opted not to correct the EC turbulent flux measurements to account for ENR in these heterogeneous and open canopies that are subject to larger systematic errors (Baldocchi et al., 2000; Kustas et al., 2000). To validate the simulated fraction of plant transpiration to evapotranspiration (*T*/*ET*), we used a field dataset of *T*/*ET* obtained through the stable isotope method described by Yépez et al. (2003). These daily-integrated values of *T*/*ET* were sampled during July 24 and 27, 2007, and July 15-16, 2008, by Tarín et al. (2014) in the subtropical scrubland. These four days exhibited relatively small measurement errors due to the wet soil conditions experienced at the site from recent storms.

We complemented the field observations with an analysis of remote sensing data on vegetation greening using the MODerate resolution Imaging Spectroradiometer (MODIS) sensors on board the EOS Terra and Aqua satellites, following Méndez-Barroso et al. (2009) and Lizárraga-Celaya et al. (2010). One of the limitations of remote sensing data in the visible and near infrared regions is the presence of cloud cover during the NAM.

To overcome this, we used composite products: 16 day composites of NDVI (MOD13Q1, 250 m spatial resolution) and white-sky shortwave albedo (MOD43B, 1 km), along with 8 day composites of LAI and fraction of Photosynthetically Active Radiation (fPAR, MOD15A2, 1 km). We spatially-averaged the 250 m NDVI data to 1 km to match the resolution of the other products. NDVI, fPAR and LAI from MODIS have been shown to represent vegetation conditions well in semiarid regions as compared to ground measurements (Privette et al., 2002; Fensholt et al., 2004; Ryu et al., 2012). Figure 2.3 illustrates the seasonal evolution of NDVI, albedo and LAI for summer periods at the ST and MW sites as bi-weekly averages and ±1 standard deviations. Datasets spanned from June 1 to September 30 over 2004 to 2009 and included the extraction of the 1 km area around each EC tower using the MODIS Data Subsetting and Visualization Tool.

Parameter	*Variable [Unit]*	*Sinaloan thornscrub*	*Madrean woodland*
Saturated hydraulic conductivity	K_s [mm/h]	55	30
Soil moisture at saturation	θ_s [-]	0.41	0.45
Residual soil moisture	θ_r [-]	0.02	0.04
Pore distribution index	m [-]	0.85	0.50
Conductivity decay parameter	f [mm^{-1}]	0.0001	0.0010
Porosity	n [-]	0.45	0.48
Volumetric heat conductivity	k_s [J/msK]	0.20	0.20
Soil heat capacity	C_s [J/m^{3}K]	1.61×10^6	1.47×10^6

Table 2.2. Soil Parameters Used in the Simulations. For The Sinaloan Thornscrub, Values Were Based on Vivoni et al. (2010) With Minor Adjustment to K_s. For the Madrean Woodland, K_s, θ_s and n Were Estimated Using the Pedotransfer Functions of Rawls et al. (1983) Using Soil Texture Data; θ_r Was Obtained from Van Genuchten (1980); m Was Estimated According to Rawls and Brakensiek (1989); f Was Based on the Logarithmic Relation Between K_s with Soil Depth Following Robles-Morúa et al. (2012); and k_s and C_s Were Determined from Lapham (1989).

Composites were linearly interpolated to daily values to allow for a gradual progression of vegetation changes. In addition, a smoothing technique that included the combination of weighted local regression and a second-degree polynomial model (with a span of 5%) was applied to the raw data to eliminate noise. This also accounts for the uncertainty in the timing of measured values within the composite. The resulting time series of NDVI, LAI, fPAR and albedo at the ST and MW sites constituted the basis for deriving vegetation parameters used in the modeling efforts described next.

2.2.3. Hydrologic Model and its Application

Hydrologic simulations were performed using the tRIBS model applied to the ST and MW sites independently. A single, hexagonal Voronoi polygon (or model element) was generated from a 30 m Digital Elevation Model (DEM) derived from the Advance Space-borne Thermal Emission and Reflection Radiometer (ASTER). A model element with an area of 98.77 m^2, a soil depth of 1 m (based on a soil pit dug at each site) and a gentle slope was used at each location. In this study, tRIBS is used as a one-dimensional model to simulate hydrologic processes that track the response to meteorological forcing, including: (1) rainfall interception, (2) evaporation from bare soil (*E*) and intercepted water (*I*) and plant transpiration (*T*), (3) infiltration and moisture redistribution, and (4) runoff production. Appendix A details the evapotranspiration calculations in tRIBS and how *ET* is partitioned into *E*, *T* and *I*. Ivanov et al. (2004) provides a description of infiltration into the sloped, heterogeneous soil above an impermeable layer. Single infiltration fronts interact with a pre-storm moisture profile, determined from hydrostatic equilibrium, and the water table position. This interaction leads to a range of possible soil moisture states, which influence infiltration and runoff generation via infiltration-excess, saturation-excess, perched return flow and groundwater exfiltration mechanisms. Meteorological forcing to the hydrologic model was obtained from measurements at each site over the study periods (June 1 to September 30 at 30 minute time step). The month of May was also included in each year (2004, 2006-2009 at ST and 2008-2009 at MW) to allow for an initial drying period that helped reduce soil moisture to low values near the residual level (θ_r) prior to the onset of the NAM. This initialization is possible due to the annual resetting of the soil moisture conditions during the dry spring prior to the summer rainy season (Vivoni et al., 2010).

Model forcings consisted of precipitation (mm), atmospheric pressure (Pa), relative humidity (%), wind speed (m/s), air temperature (°C) and incoming solar radiation (W/m^2) with a time resolution of 30 minutes. Gaps in the meteorological observations due to periods of no data collection were filled in with ground-adjusted forcing from the North American Land Data Assimilation System (NLDAS, Mitchell et al., 2004), following Robles-Morúa et al. (2012). The percentage of time with gap-filled forcing ranged from 13 to 67% of the periods, depending on the site and year, with the largest gaps for 2006-2007 (ST, 61 and 67%) and 2008 (MW, 63%).

Parameter	*Variable [Unit]*	*Sinaloan thornscrub*			*Madrean woodland*		
		Dynamic	*Leaf off*	*Leaf on*	*Dynamic*	*Leaf off*	*Leaf on*
Free through fall coefficient	p [-]	0.09 - 0.78	0.75	0.13	0.06 - 0.51	0.51	0.06
Maximum canopy storage	S [mm]	0.07 - 0.75	0.09	0.67	0.23 - 0.94	0.23	0.97
Albedo	a [-]	0.13 - 0.19	0.18	0.15	0.13 - 0.17	0.17	0.14
Vegetation height	h [m]	6	6	6	8	8	8
Optical transmission coefficient	k_t [-]	0.37 - 0.90	0.89	0.42	0.55 - 0.86	0.86	0.55
Minimum canopy stomatal resistance	r_s [s/m]	19.5 - 247	197	23	18 - 94	85	18
Vegetation fraction	v_f [-]	0 - 0.95	0.00	0.76	0 - 0.68	0.00	0.61
Soil evaporation stress factor	β_E [-]	0.55	0.55	0.55	0.55	0.55	0.55
Plant transpiration stress factor	β_T [-]	0.10	0.10	0.10	0.55	0.55	0.55

Table 2.3. Vegetation Parameters at the Sinaloan Thornscrub and Madrean Woodland Sites for the Three Simulation Scenarios. Constant β_E And β_T were Obtained from Model Calibration. For the Dynamic Scenario, Parameter Ranges Shown Represent Minimum and Maximum Values.

Soil parameters were obtained through a manual calibration process that focused on the 2006 and 2008 summer periods for ST and MW sites, respectively. In this process, the soil parameters remained constant in time for each site. Initial parameter values were obtained from soil pedotransfer functions based on particle size fraction and bulk density (Van Genuchten, 1980; Rawls et al., 1983; Rawls and Brakensiek, 1989; Lapham, 1989). At the ST site, soil analyses indicated a sandy loam texture in the top 30 cm and sandy clay in the lower profile down to about 75 cm. At the MW site, soil analyses revealed a sandy loam texture in the upper 40 cm of soil and a sandy clay loam down to the 55 cm of sampling depth. Manual adjustments to soil parameters within feasible ranges were performed independently at each site for the calibration periods only, based on the comparison of observed and simulated surface soil moisture (*SM*, top 10 cm) and evapotranspiration (*ET*) using the Mean Absolute Error (MAE), Correlation Coefficient (CC) and Bias (B, see Appendix B). Sensible heat flux (*H*) was inspected for model validation purposes only using similar metrics, while root zone soil moisture (top 1 m) was not used in the model calibration or testing due to a lack of similar observations. Table 2.2 presents the soil parameters for each site and their source. Note the manual procedure allowed us to retain well-constrained values from pedotransfer functions, while focusing on parameters with higher uncertainty, such as the pore distribution index. Model testing was then performed for the remaining summer periods (2004, 2007-2009 at ST and 2009 at MW).

Vegetation parameters were specified as time-varying quantities based on relationships to remotely-sensed data from MODIS. Appendix C describes the empirical equations used to transform the linearly-interpolated, daily MODIS observations of LAI, NDVI, fPAR and albedo into the vegetation parameters defined in Table 2.3. The implemented relations are considered more sophisticated than the methods presented by Vivoni (2012), in particular with respect to S, p and r_s. Three scenarios were considered to examine the effects of vegetation greening on the simulated *ET* and *SM*: (1) Dynamic (time-varying plant parameters for each year), (2) Leaf off (fixed or time-constant vegetation parameters with no leaves) and (3) Leaf on (fixed vegetation parameters under full canopy conditions). For each scenario, the vegetation parameters apply to the vegetation fraction or green cover (v_f) of the model element occupied by a subtropical tree species at ST and an oak tree at the MW site, while the 1-v_f fraction is treated as bare soil. Note that the green vegetation fraction of a model element varies from near zero (Leaf off) to values near 0.7 or 1 (Dynamic) in Table 2.3. To obtain the Leaf off values, the mean of the minimum values of v_f and S were calculated for each site over the 2004 to 2009 period, while the mean of the maximum values of a, k_t, p and r_s where utilized to represent dormancy. In contrast, Leaf on conditions were based on the mean of the maximum v_f and S and the mean of the minimum a, k_t, p and r_s over 2004-2009. This selection implies that Leaf off and Leaf on scenarios are representative of average minimum and maximum greenness over five summers. As a result, care must be taken when interpreting results from each summer at each site relative to this selection. Note that the Dynamic scenario varies for each summer, thus effectively capturing interannual variations in vegetation greening and its impact on all correlated plant processes.

Evapotranspiration partitioning depends on the ability of *E* and *T* to extract soil water from the surface and root zones, respectively (e.g., Newman et al., 2006). In the model, this is parameterized using piecewise linear relations between *E* and surface soil moisture (top 10 cm) and *T* and root zone soil moisture (top 1 m), which are controlled by stress factors (Appendix A, Ivanov et al., 2004). The selection of the soil evaporation (β_E) and plant transpiration (β_T) stress factors (Table 2.3) was based on a manual parameter sensitivity analysis for the calibration periods in each ecosystem, as opposed to the fixed and equal factors used by Vivoni (2012). The sensitivity analysis systematically varied β_E and β_T within the 0 to 1 range to explore all possible combinations at each site. We selected the pair of β_E and β_T that minimized the simulated errors in *ET* and *SM* with respect to the observations at each site using the MAE, CC and B metrics. The resulting values indicate that soil evaporation stress factors are similar in each ecosystem ($\beta_E = 0.55$), which is consistent with the sandy loam texture at each site. The plant transpiration stress factor, on the other hand, varied with plant functional type with β_T having smaller values at ST ($\beta_T = 0.1$), as compared to MW ($\beta_T = 0.55$), due to the greater capacity of ST to sustain plant *T* under lower soil moisture conditions (Vivoni et al., 2008). This is also consistent with the more rapid green-up in the subtropical scrubland, which suggests a more efficient use of soil water by transpiration (Méndez-Barroso et al., 2009; Forzieri et al., 2011).

2.3. Results

2.3.1. Seasonal Evolution of Vegetation Parameters

Figure 2.4 depicts the seasonal evolution of the vegetation parameters averaged over all simulation periods, including ± 1 standard deviations to represent interannual variability.

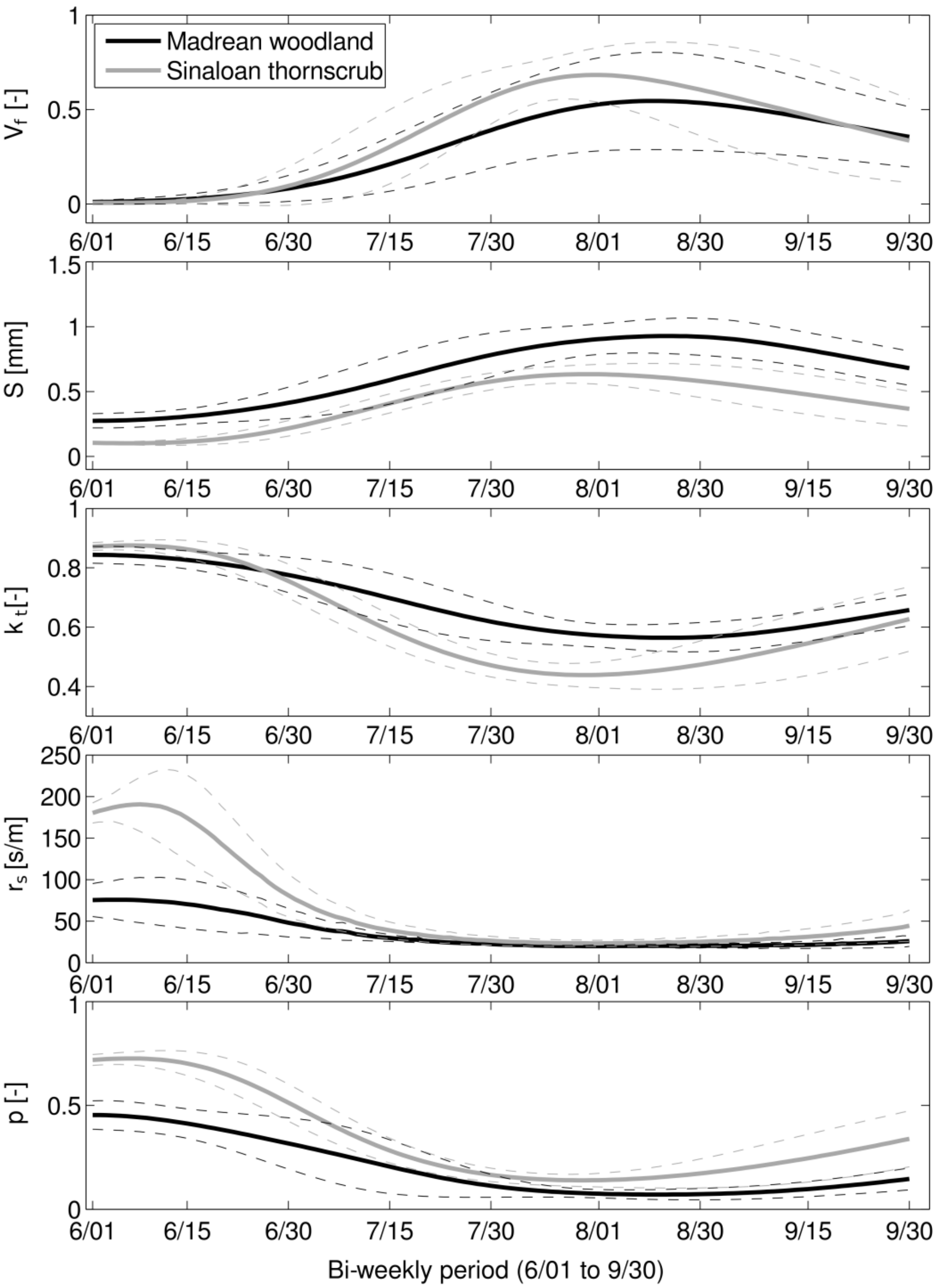

Figure 2.4. Seasonal Evolution of Vegetation Parameters from MODIS for the Sinaloan Thornscrub (Gray Solid Line, 2004, 2006-2009) and Madrean Woodland (Black Solid Line, 2008-2009) Sites. Dashed Lines Depict ±1 Standard Deviation in Time for Each Ecosystem Across All Summers. Vegetation Parameters Were Estimated Based on Empirical Relations that Link Vegetation Fraction (V_f), Maximum Canopy Storage (*S*), Optical Transmission Coefficient (K_t), Minimum Canopy Stomatal Resistance (R_s) and Free Through Fall Coefficient (*P*) With Leaf Area Index (LAI), Fraction of Photosynthetically Active Radiation (fPAR) and Normalized Difference Vegetation Index (NDVI).

Clearly, the onset of vegetation greening in early July leads to large changes in the representation of vegetation parameters in the model. For example, the vegetation fraction (v_f) increases from values near zero to an average of 0.6 in the subtropical scrubland and 0.5 in the oak savanna.

The interannual variability in v_f is higher at the MW site, in particular near the peak values. Overall, note that the ST site typically has earlier maximum or minimum values in vegetation parameters (mid-July) as compared to MW (mid-August). Since vegetation parameters were derived from remote sensing data, these all exhibit internally consistent temporal variations. Furthermore, differences between the two sites are consistent with field evidence (Vivoni et al., 2010; Tarín et al., 2014), indicating that ST has a higher vegetation cover (higher v_f) and shading (lower k_t), but a lower interception capacity (lower S and higher p). Overall, the time-varying v_f is a major difference between the ecosystems since it has a strong control on *ET* partitioning (Vivoni, 2012). Furthermore, the fraction 1- v_f is considered in the model as bare soil in both ecosystems, where grasses and forbs, cacti or succulents may actually occupy these understory spaces.

2.3.2. Seasonal and Interannual Variations in *ET* and *SM*

The multiple summer periods at the ST and MW sites allow for a comparison of the seasonal evolution of *ET* and *SM* for varying interannual conditions. As shown in Table 2.1, total summer precipitation (JJAS) can vary substantially in the region, in accordance with the strength of the NAM (Higgins and Shi, 2001; Gutzler, 2004; Forzieri et al., 2011). As compared to long-term averages at Rayón (near ST site) and Meresichic (near MW site but at lower elevation), the study periods fall into below-average (2004 and 2009) and average (2006-2008) categories. Soil moisture, vegetation greenness and evapotranspiration are expected to vary in response to year-to-year differences in precipitation (e.g., Tang et al., 2012). Furthermore, the onset and demise of the NAM varies interannually, leading to changes in the timing and duration of greening and its associated effects on water and energy fluxes. As such, we first present the comparison of model simulations that capture vegetation seasonality in each summer to the observations in each site.

For reference, the smoothed, daily NDVI time series is presented along with the composite NDVI values placed at the mid-point of the compositing period.

Figure 2.5 presents the seasonal evolution and interannual differences in observed rainfall, vegetation greening (NDVI) and surface soil moisture (average of top 10 cm of soil) as derived from available observations (average of sensors at 5 and 10 cm) and model simulations using the Dynamic scenario at the ST site. Note how precipitation pulses affect the rapid vegetation green-up and their coincident influence on the surface soil moisture. Diurnal fluctuations are due to a temperature-dependence of the sensors when installed at shallow depths (Seyfried and Murdock, 2004; Vivoni et al., 2007b) and not a diurnal redistribution of soil moisture. The observed and simulated soil moisture (depicted volumetrically as m^3/m^3 at 30 min intervals) match well, in particular with respect to average conditions and the peak and recession characteristics of each wetting event across all summers.

Model performance was inferior during periods when: (1) meteorological forcings from the tower was missing and NLDAS products were used in their place (i.e., 2006 had a high percentage of missing tower forcing, 67%), and (2) soil moisture sensors did not operate correctly (i.e., 2009 had issues with soil moisture data availability and quality). Note that the same soil parameters (Table 2.2) were used for each summer based on the calibration period, such that only meteorological forcing and vegetation parameters vary in time each summer in accordance with the observed conditions. Table 2.4 provides a quantitative evaluation of *SM* at the 30 minute resolution for the Dynamic scenario at the ST site, showing a low MAE of 0.02 m^3/m^3, a B near 1.1 and a CC greater than ~0.7 across all summers. Model performance varies depending on the metric and variable inspected, but is generally consistent across calibration and testing periods, suggesting the model is transferable across the different summer periods. In addition, the model performance in terms of soil moisture is robust with respect to the time scale of evaluation, as shown by the daily-averaged statistics in Table 2.4.

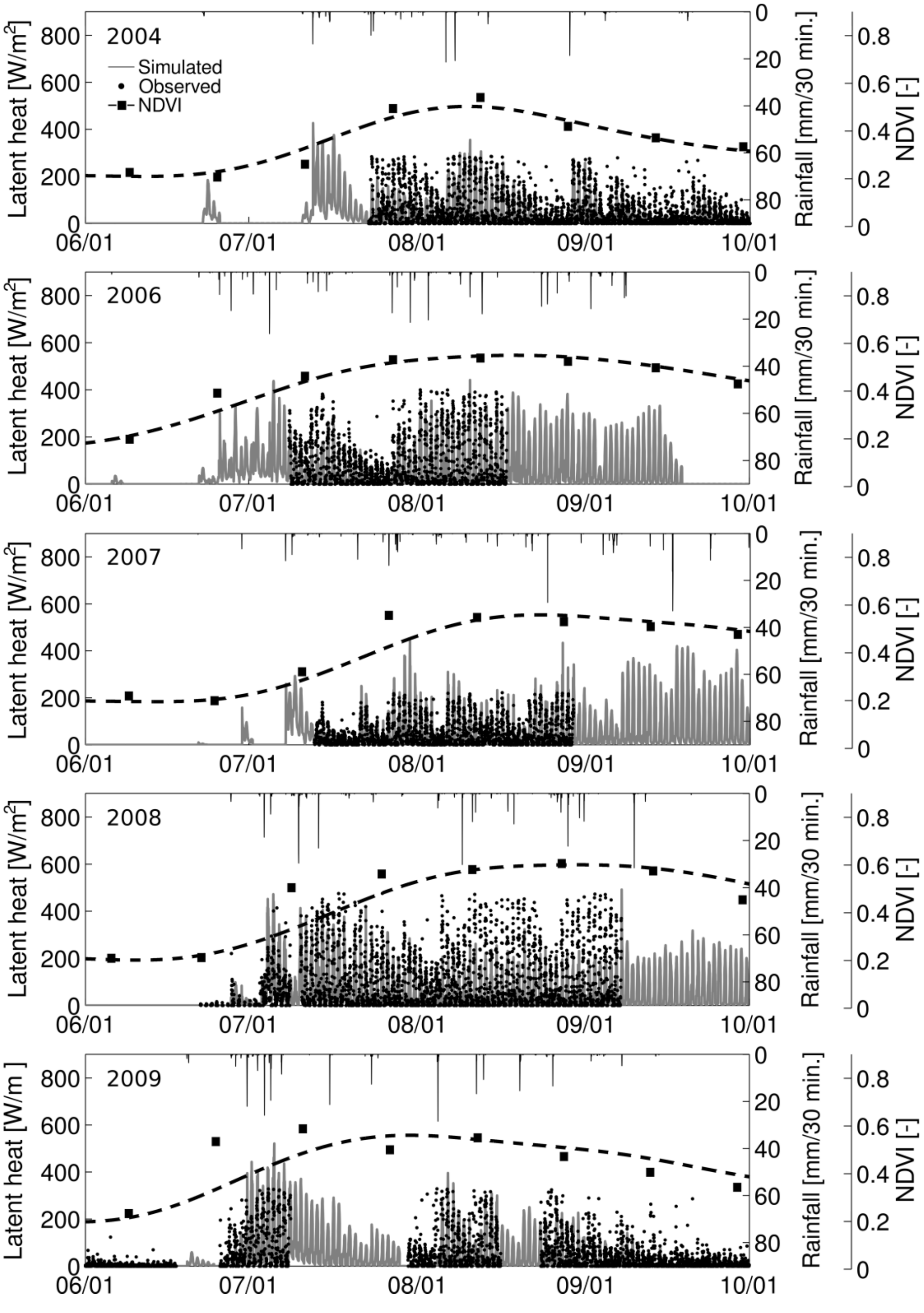

Figure 2.5. Comparison of Observed and Simulated Soil Moisture (*SM* At 10 cm Depth) at the Sinaloan Thornscrub Site for 2004 And 2006-2009. Model Simulations Account for the Dynamic Scenario. For Reference, NDVI Shows the Vegetation Greenness Variations at the Site With the Squares Indicating the Composite Data With the Smoothed Series as Dashed Lines. Gaps in the Observations Due to Sampling Protocols or Equipment Malfunction are Depicted by Missing Data.

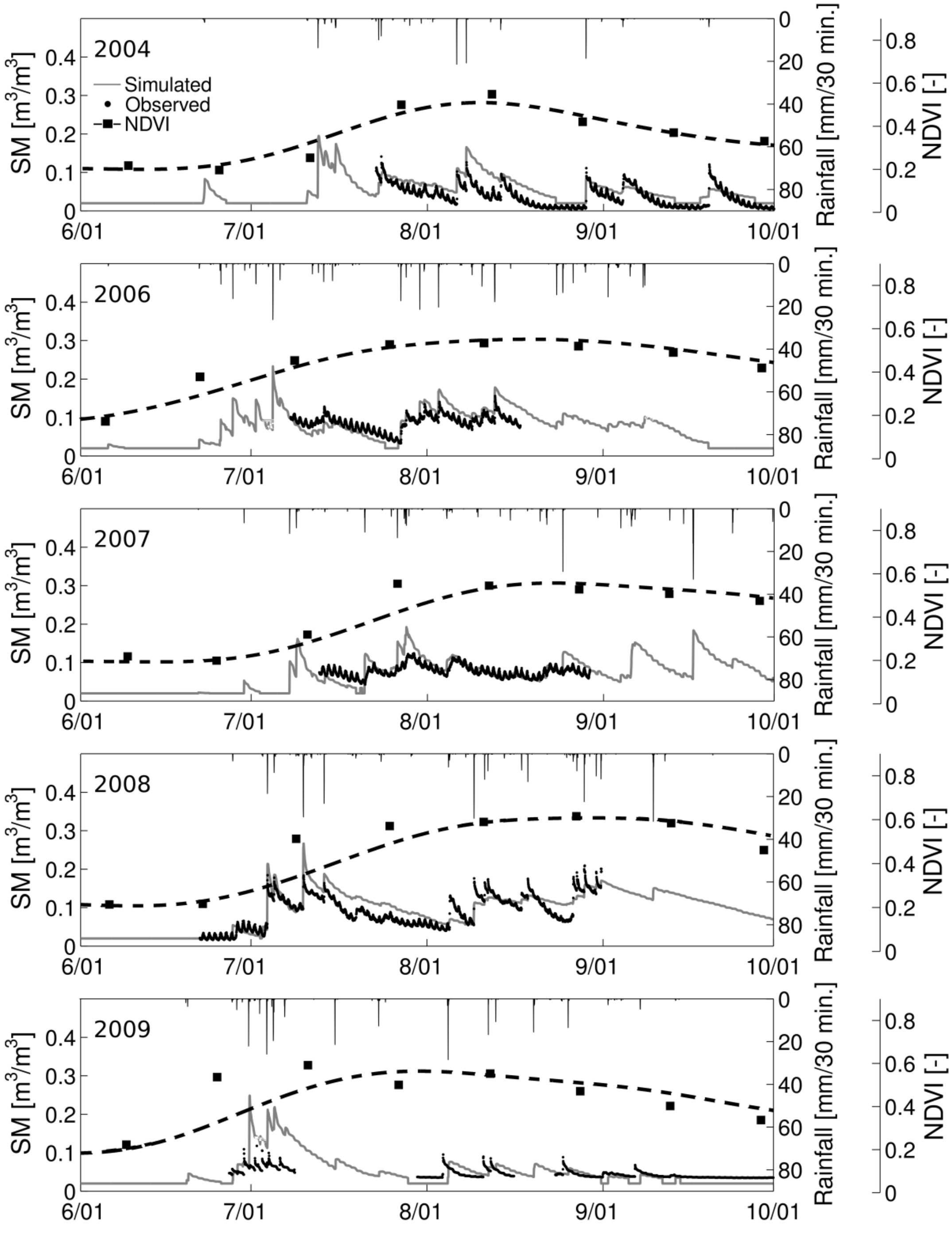

Figure 2.6. Comparison of Observed and Simulated Latent Heat Flux at the ST Site for 2004 and 2006-2009 Under the Dynamic Scenario. Gaps in the Observations are Depicted by Missing Data. For Reference, NDVI Shows the Vegetation Greenness Variations at the Site With the Squares Indicating the Composite Data With the Smoothed Series as Dashed Lines.

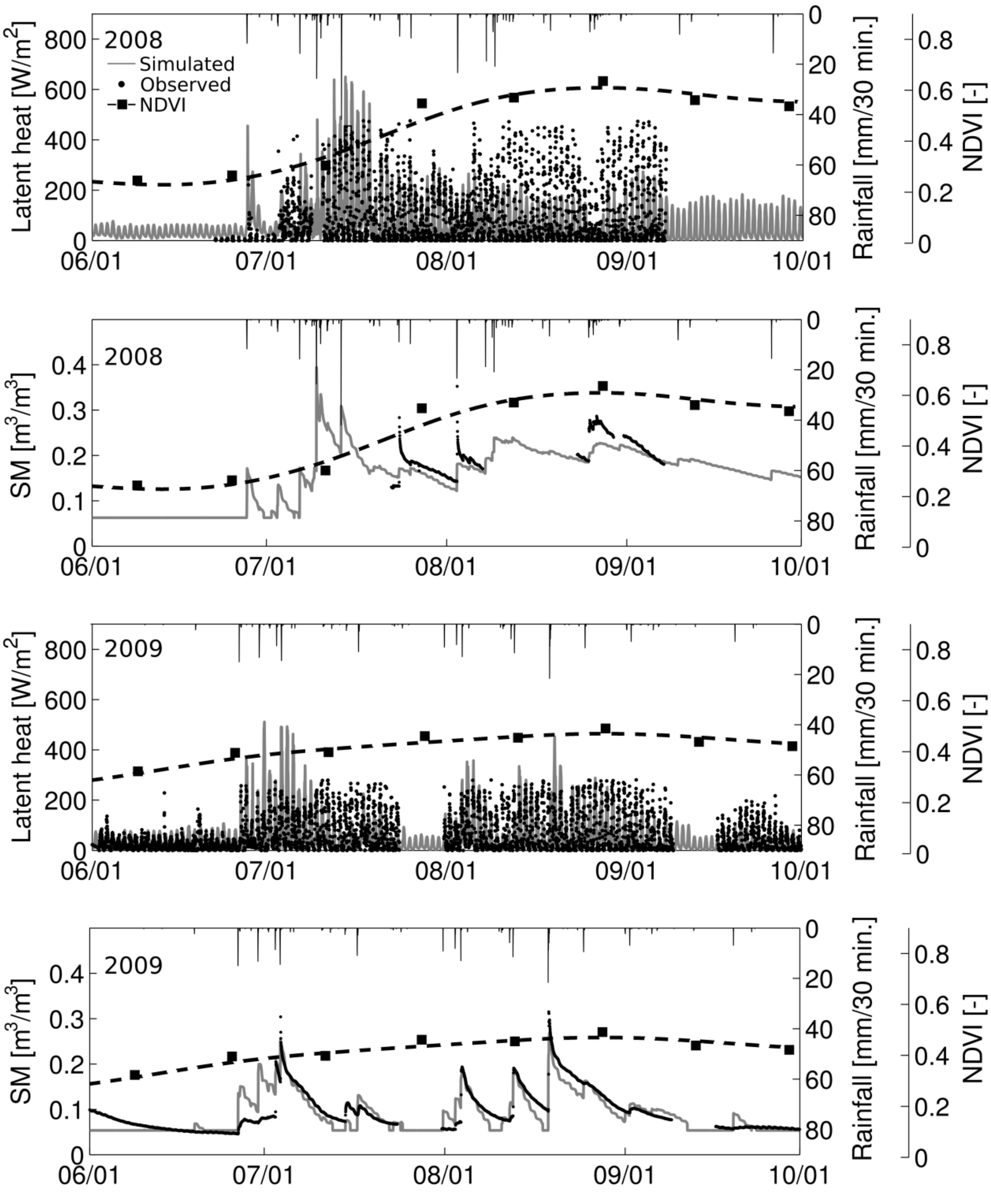

Figure 2.7. Comparison of Observed and Simulated Latent Heat Flux and Surface Soil Moisture (*SM*, Top 10 cm) at the MW Site for 2008-2009. Missing Data are Due to Observational Gaps. For Reference, NDVI Shows the Vegetation Greenness Variations at the Site With the Squares Indicating the Composite Data With the Smoothed Series as Dashed Lines.

Overall, the model captures the major features of the soil moisture data at the ST site, including how certain summer periods have sustained levels of high soil water content (2006-

2008), while others experience long interstorm periods with low soil moisture levels (2004, 2009). The seasonal progression of soil wetting induces a vegetation green-up that increases *ET* in the subtropical scrubland, as depicted across all summers in Figure 2.6. Only daytime periods are included in the comparison. Latent heat flux (*λET,* where *λ* is the latent heat of vaporization) is low prior to the NAM onset (June) in both the observations and model simulations (see 2008 and 2009). As *SM* and NDVI increase, the Dynamic scenario captures well the gradual rise in *ET* and its temporal variations in response to individual storms and dry periods. Reductions in *ET* during late summer are also captured well in response to lower water availability and radiation, as well as the start of vegetation senescence.

Table 2.4 shows the model performance metrics with respect to latent and sensible heat flux (W/m^2) at the ST site at both 30 minute and daily scales. For the 30 minute statistics, we obtained an average MAE of 41 W/m^2, average B of 0.62 and average CC of 0.68 for *λE* and an average MAE of 53 W/m^2, average B of 0.53 and average CC of 0.61 for *H* across all summers, consistent with daily total fluxes. Focusing on *λE*, the Bias indicates that under certain conditions in mid-summer the model underestimates *ET* with respect to observations, as seen in 2008, likely due to an inability of the model to account for transpiration emanating from plant water uptake from deep (> 1 m) soil layers occurring when the modeled (1 m) root zone has dried. Despite this, the major features of the seasonal evolution of *ET* and its interannual variation are nevertheless captured with reasonable accuracy to warrant a closer analysis of the underlying soil and vegetation contributions to the total *ET*.

Figure 2.7 presents the comparison of *ET* and *SM* observations and model simulations at the MW site for 2008 and 2009 using the Dynamic scenario. Only daytime periods are included in the comparison. The wetter summer in 2008 (551 mm) leads to a higher NDVI than in the drier 2009 summer (321 mm), with vegetation greenness slowly increasing during the NAM onset and peaking in mid-August in both periods.

Year	*Latent heat flux*			*Sensible heat flux*			*Surface soil moisture*		
	B [-]	*MAE [W/m^2] or [MJ/m^2/day]*	*CC [-]*	*B [-]*	*MAE [W/m^2] or [MJ/m^2/day]*	*CC [-]*	*B [-]*	*MAE [m^3/m^3]*	*CC [-]*
Sinaloan thornscrub, ST (30 minute statistics)									
2004	0.53	31.46	0.71	0.72	58.40	0.69	0.90	0.02	0.75
2006	*0.60*	*45.35*	*0.78*	*0.84*	*37.85*	*0.66*	*1.06*	*0.02*	*0.79*
2007	0.87	28.52	0.68	0.46	47.33	0.61	1.05	0.02	0.65
2008	0.51	71.28	0.58	0.13	50.19	0.45	1.08	0.02	0.86
2009	0.58	30.32	0.66	0.48	71.10	0.63	1.14	0.02	0.66
Sinaloan thornscrub, ST (daily statistics)									
2004	0.48	76.63	0.85	0.77	90.73	0.67	0.90	0.02	0.78
2006	*0.64*	*105.32*	*0.94*	*0.84*	*73.87*	*0.78*	*1.05*	*0.02*	*0.84*
2007	0.92	53.02	0.84	0.46	138.66	0.72	1.04	0.02	0.76
2008	0.49	257.79	0.16	0.13	188.14	0.23	1.08	0.02	0.88
2009	0.56	37.47	0.91	0.48	206.36	0.72	1.12	0.02	0.79
Madrean woodland, MW (30 minute statistics)									
2008	*0.75*	*62.38*	*0.67*	*0.17*	*62.26*	*0.49*	*0.78*	*0.04*	*0.90*
2009	0.91	39.86	0.57	0.91	74.04	0.59	1.00	0.02	0.74
Madrean woodland, MW (daily statistics)									
2008	*0.75*	*135.33*	*0.46*	*0.18*	*170.60*	*0.31*	*0.77*	*0.05*	*0.93*
2009	1.03	64.00	0.73	0.91	107.84	0.48	0.99	0.02	0.76

Table 2.4. Model Performance for Periods With Simultaneous Observations and Simulations of Latent Heat Flux, Sensible Heat Flux and Surface Soil Moisture at the ST and MW Sites for the Dynamic Scenario for Both 30 Minute and Daily Intervals. Italicized Years Represent the Model Calibration Periods. The Statistical Metrics Used to Measure Model Performance Were Bias (B), Mean Absolute Error (MAE) and Correlation Coefficient (CC). The Units of MAE Depend on 30 Minute (W/M^2) or Daily (MJ/M^2/Day) Statistics for the Latent and Sensible Heat Fluxes.

Differences in time-varying vegetation parameters in the Dynamic scenario (under the same soil properties of Table 2.2) are able to capture well the interannual variations in *ET* and *SM*, with wetter soils and higher evapotranspiration losses in 2008 than in 2009. Table 2.4 shows that the model performance at the Madrean woodland is comparable to the ST site in terms of latent and sensible heat fluxes and surface soil moisture, with a better match during the drier 2009 period, at both 30 minute and daily scales. This suggests that model performance may improve in terms of certain variables above the calibration results depending on the meteorological forcing and its subsequent vegetation response. For this ecosystem, the seasonal evolution of *ET* and *SM* are also captured well, as are the hydrologic responses to individual storms and subsequent dry-down periods. It is interesting to note that the MW site experiences higher soil moisture values with lower recession rates as compared to the ST ecosystem. The more frequent, smaller rainfall events at the higher elevation MW site (Gebremichael et al., 2007) also permit sustained *ET* throughout the summer season. Although the model captured well the observations overall, it is important to note an underestimation in *ET* in August and September 2008, which are likely related to the high precipitation that year leading to plant water uptake from deep (> 1 m) soil layers.

In addition, high rainfall conditions and the presence of fog or dew during this period may have interfered with the EC measurements causing unusually large and sustained *ET* observations that were not removed during standard data processing using the quality control method of Mauder and Foken (2004). Among other identified sources of EC measurement error (e.g., Kochendorfer et al., 2012; Frank et al., 2013), the effects of standing water from fog, dew or precipitation on the LI7500 sensor are well known and occur by obstructing passage of the infrared beam (e.g., Massman and Lee, 2002).

2.3.3. Comparisons of *ET-SM* Relation for Vegetation Scenarios

The two static scenarios (Leaf off and Leaf on) allow analyzing the effects of seasonal and interannual variations of vegetation on the hydrologic conditions at the ST and MW sites. For simplicity, these scenarios are described through a comparison of the relation between daily total *ET* and daily-averaged *SM* for the top 10 cm. Figure 2.8 presents the *ET*-*SM* relation for each summer period from the three scenarios as well as the available daily data (not used in the relations). For clarity, the simulations for all summer days are presented as piecewise linear regressions, such that the lines are a visualization tool to compare the scenarios.

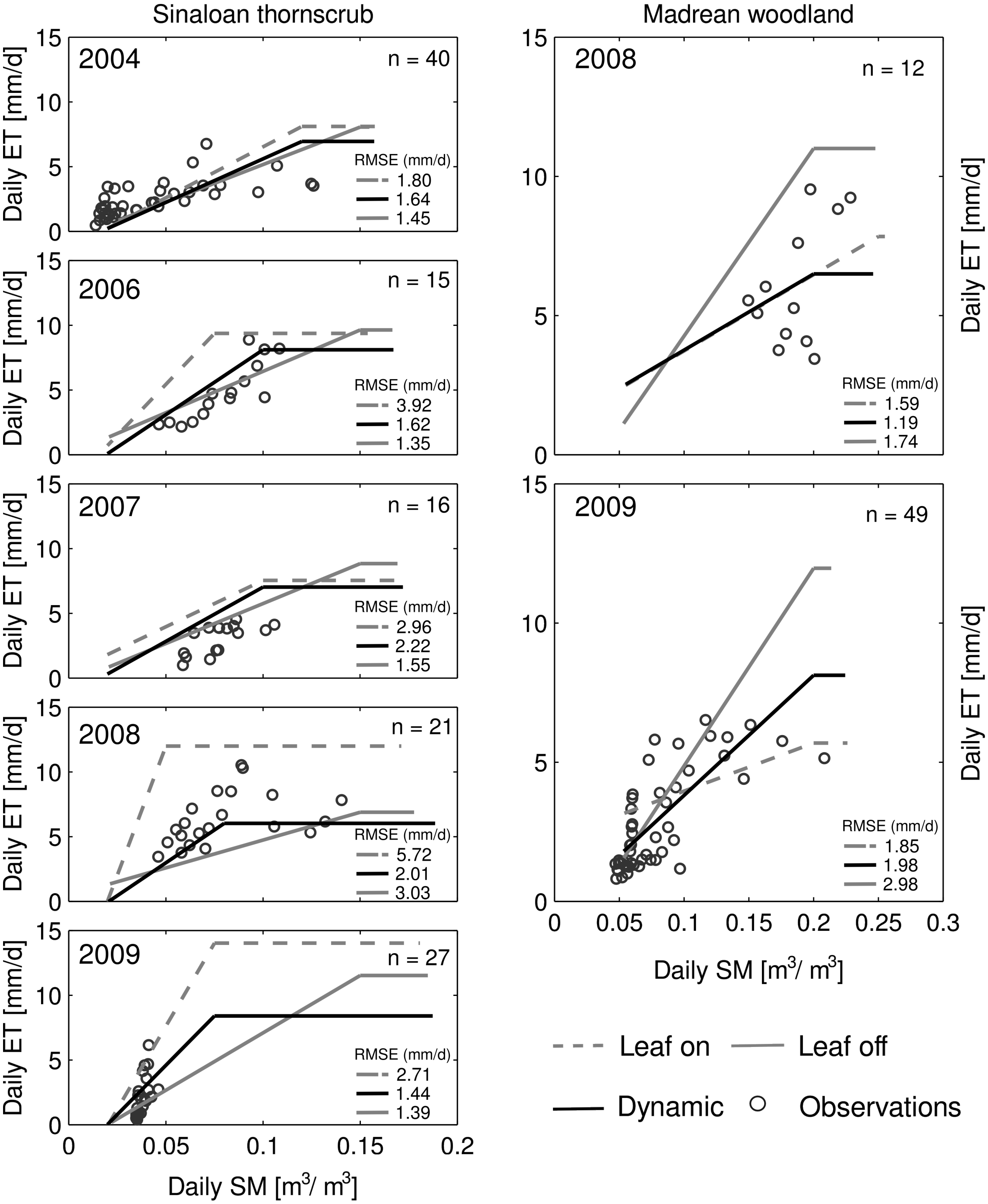

Figure 2.8. Interannual Variability of the Relation Between Daily Evapotranspiration and Surface Soil Moisture (*SM*, Top 10 Cm) for Three Vegetation Scenarios at the ST and MW Sites. Daily Observations (*n* Is The Number Of Available Days) are Included for Comparison (Circles) Along With the Root Mean Square Error (RMSE) in Evapotranspiration (Mm/Day) for the Piecewise Linear Regression in Each Scenario.

The regression parameters were identified through a semi-automatic procedure aimed at minimizing the root mean square error (RMSE) between the pair of points (*SM*, *ET*) of the model simulations and the regression lines. Note that the *ET*-*SM* relations are determined based on all simulated days, while the observations are limited to only days (*n*) with available data. The regressions allow depicting the stressed *ET* (region with positive slope) and the maximum *ET* (region with constant values) corresponding to low and high *SM*. From the observations, it is clear that interannual variations exist in the *ET* and *SM* ranges at both sites, with wetter summers (2006-2008) exhibiting higher values. Due to its adjustment of vegetation parameters each summer, the Dynamic scenario shows interannual differences in the *ET*-*SM* relation that visually match the observations better than the Leaf off and Leaf on scenarios. This is corroborated by the lower RMSE in daily *ET* between observations and the piecewise linear regressions for the Dynamic scenario. When averaged over all summers and both sites, the Dynamic case has an RMSE of 1.73 mm/day, as compared to 1.93 mm/day and 2.93 mm/day for the Leaf off and Leaf on scenarios. The *ET*-*SM* relation for the Dynamic scenario generally has better performance relative to observations for the calibration periods (2006 at ST and 2008 at MW), with a lower skill in the testing periods.

The Leaf on and Leaf off cases present an interesting comparison to the Dynamic scenario in each ecosystem. For the ST site, the Leaf on scenario has the highest *ET* for most *SM* values across all summer periods, indicating the full canopy development in the subtropical scrubland maximizes *ET* losses to the atmosphere and thus lowers *SM*. This suggests that plant transpiration is a more efficient means to extract soil moisture since it acts over a deeper (1 m) profile and has a lower stress factor, β_T (Table 2.3). In contrast, the Leaf off scenario has the lowest *ET* and highest *SM*, indicating that bare soil conditions at the ST site have lower losses, primarily due to a higher soil evaporation stress factor, β_E (Table 2.3). Interestingly, the Dynamic scenario has a behavior that suggests that time-varying parameters result in an *ET* bounded by the two other cases, in particular for intermediate soil moisture values (i.e., 0.05 to 0.125 m^3/m^3). In the oak savanna, comparisons between vegetation scenarios are limited to two summers.

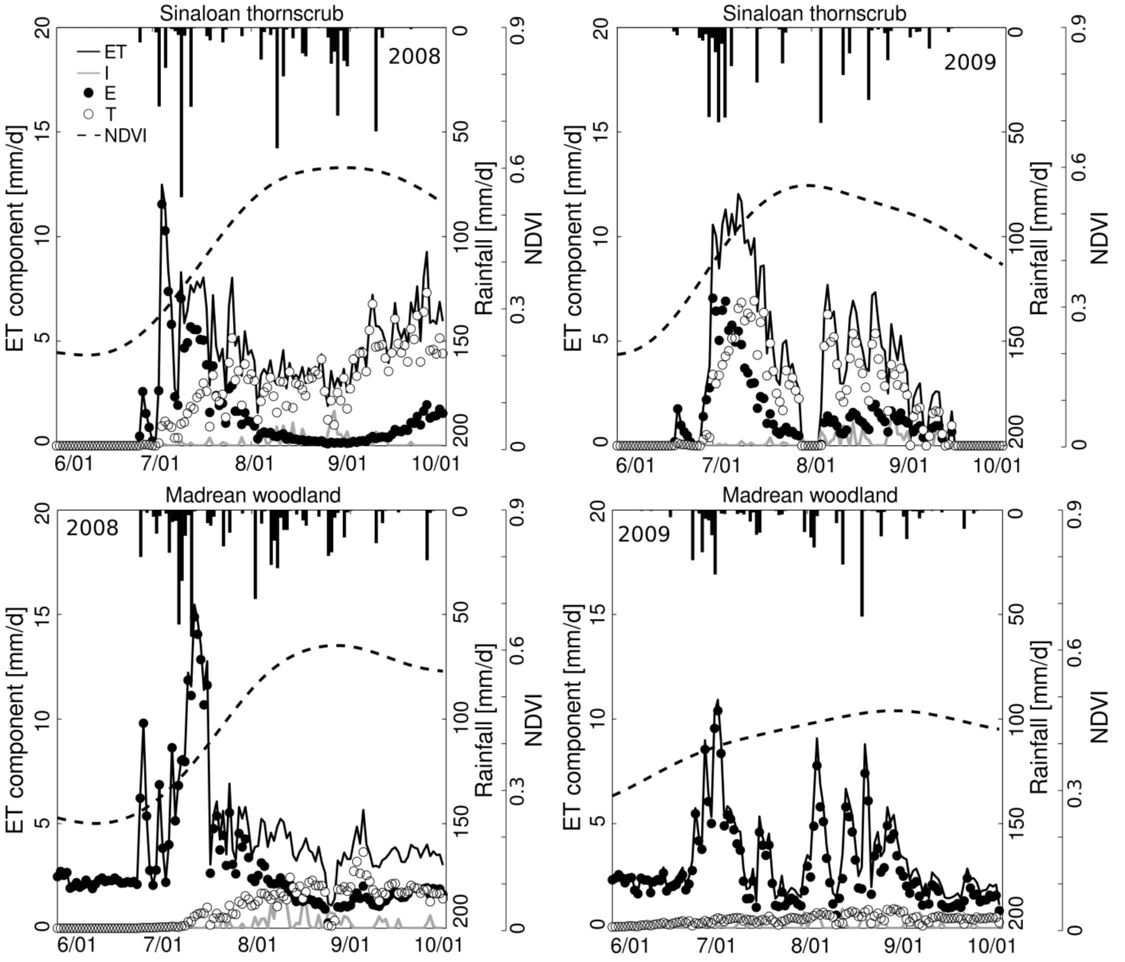

Figure 2.9. Simulated Evapotranspiration Partitioning Under the Dynamic Scenario at the ST and MW Sites for 2008 and 2009. For Reference, NDVI Shows the Observed Vegetation Greenness Variations at the Sites.

The Leaf on and Leaf off scenarios were selected from observations over a period of five summers and as a result represent conditions not necessarily experienced in 2008 and 2009. In contrast to the ST site, the minimum greenness in the Leaf off scenario leads to high *ET* and low *SM*, while the maximum greenness in the Leaf on scenario leads to a lower *ET* and higher *SM*. Here, the Dynamic scenario also exhibits an intermediate *ET*-*SM* relation as compared to the bounds presented by the other cases and matches the field data better when averaged over the two seasons, as shown by the RMSE. Differences between MW and ST in the relative performance of the Leaf off and Leaf on scenarios can be attributed to: (1) Higher incoming solar radiation that favors greater *ET* at MW and (2) Lower vegetation fraction in the oak savanna. Interestingly, the ability of the Dynamic scenario to adjust the *ET-SM* relation to match the available data indicates that vegetation greening plays a crucial role in modulating losses to the atmosphere in the oak savanna ecosystem. It also reveals that lower vegetation fractions at MW leads to a different behavior as compared to the ST site, with respect to the partitioning of *ET* between vegetation canopies and surrounding bare soil, as will be explored in the following.

2.3.4. Temporal Variations of *ET* Partitioning

The simulated partitioning of evapotranspiration (Appendix C) permits an evaluation of the effect of vegetation greening on soil- and vegetation-mediated processes. Figure 2.9 presents the simulated *ET* partitioning for two contrasting summers, the wetter 2008 and drier 2009 periods, at the ST and MW sites under the Dynamic scenario. Both summers received rainfall events in late June and early July, but 2008 had more sustained precipitation in late August and September that allowed NDVI to remain higher. Prior to green-up, *ET* is dominated by soil evaporation (*E*) at both sites, as bare soil fractions ($1-v_f$) are greater than 50%. In the subtropical scrubland, a switch to transpiration (*T*) dominance was simulated after early to mid-July, reaching values of 5 to 7 mm/day in each summer, with an earlier green-up and a quicker transition to transpiration in 2009. In contrast, the oak savanna exhibited this switch only in the wetter 2008 period. The late greening and low NDVI at MW in 2009 resulted in higher soil evaporation rates throughout the season. During the late summer, precipitation determines whether *ET* is sustained (as in 2008) or rapidly decays (as in 2009), while the partitioning begins to favor *E* as NDVI decreases in response to lower radiation. Overall, transpiration rates at MW were consistently lower than at ST and contributed a lower fraction of the total *ET*. Since total *ET* averaged over all summers was higher at MW (465 mm) than at ST (422 mm), *E* plays a dominant role in the oak savanna due to a sparser plant cover. As expected, the evaporation of intercepted water (*I*) had a small contribution to *ET* with maximum values of 2 mm/day during periods of higher v_f.

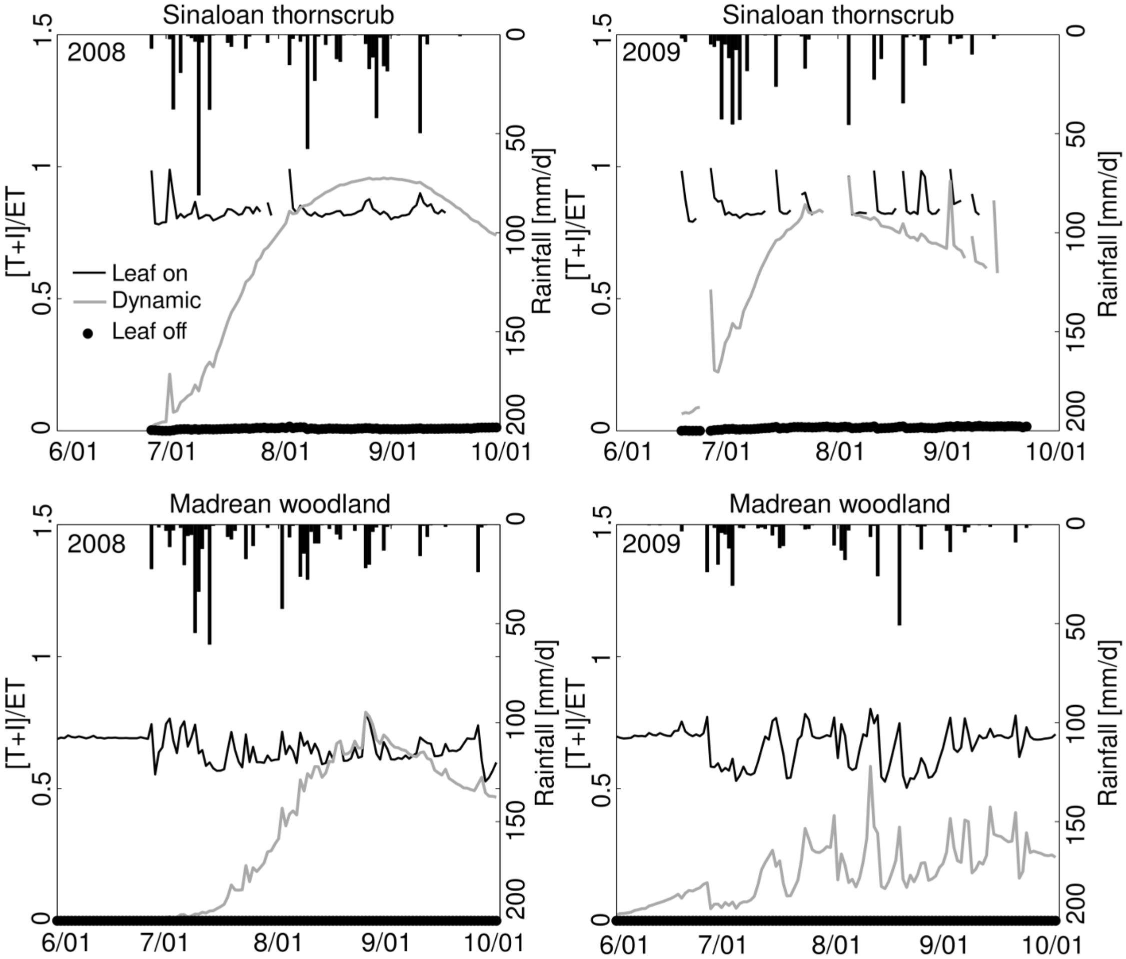

Figure 2.10. Vegetation-Mediated Fraction, (T+I)/ET, Under Three Vegetation Scenarios at the ST and MW Sites for 2008 and 2009.

The impact of the vegetation greening on the *ET* partitioning is presented in Figure 2.10 by comparing the vegetation scenarios in terms of the vegetation-mediated fractions or (*T*+*I*)/*ET*. Vegetation-mediated processes are typically dominated by transpiration and *E*/*ET* can be obtained as 1 - (*T*+*I*)/*ET*. The comparison in Figure 2.10 includes both the ST and MW sites for the wetter 2008 and drier 2009 summer periods. Note that the Leaf off scenario was entirely dominated by *E*/*ET* such that (*T*+*I*)/*ET* was near zero for all cases.

Similarly, the Leaf on scenario exhibited (*T*+*I*)/*ET* primarily between 0.8 and 1 (ST) and 0.5 and 0.7 (MW), indicating a significantly lower contribution of *E/ET* at ST and a larger *E*/*ET* at

MW. As such, the Leaf off and Leaf on scenarios are considered as hypothetical bounds on the actual *ET* partitioning for each ecosystem under variable (day-to-day) meteorological forcing.

The Dynamic scenario, on the other hand, represents well the seasonal evolution and interannual variations in *ET* partitioning. $(T+I)/ET$ exhibits a gradual increase in response to vegetation green-up and a peak amount and timing that varies according to the seasonal distribution of rainfall events. During peak greenness, $(T+I)/ET$ can range from 0.5 to 1, with higher contributions at ST and for wetter periods. Interestingly, the day-to-day variations in $(T+I)/ET$ seem to be higher for the drier 2009 period at both sites, indicating that lower vegetation greenness leads to higher susceptibility to decreases in vegetation-mediated processes during interstorm periods. The drier summer also has a lower seasonal recession of $(T+I)/ET$ in each ecosystem. This indicates that *ET* partitioning is highly variable within and across summer seasons in response to vegetation differences.

2.3.5. Comparison of *ET* Partitioning in Two Ecosystems

The analysis over multiple summers in the two ecosystems allows determining the impact of seasonal rainfall amounts on the partitioning of evapotranspiration. Establishing this relation would allow for a simple approach for estimating the vegetation effects on *ET* based on available rainfall data for the two different ecosystems. Figure 2.11 shows the relation between the monthly vegetation-mediated losses to the atmosphere, $(T+I)/ET$, and the cumulative rainfall over the current and previous months (P_{accm}) and the best-fit regressions obtained over a range of possible models. The ST site shows an asymptotic relation between $(T+I)/ET$ and P_{accm} over the five summer periods ($n = 20$ based on 4 months in five summers; $(T+I)/ET = -2.0\times10^{-6}P_{accm}^{2} + 2.5\times10^{-3}P_{accm} - 2.4\times10^{-2}$, $R^2 = 0.95$). In contrast, the MW site exhibits a linear increase in $(T+I)/ET$ with the cumulative rainfall ($n = 8$ for 4 months in 2 summers; $(T+I)/ET = 9.2\times10^{-4}P_{accm} - 5.7\times10^{-2}$, $R^2 = 0.92$). In both cases, higher accumulated precipitation leads to a greater amount of vegetation-mediated processes due to the production of biomass supporting transpiration and evaporation of intercepted rainfall.

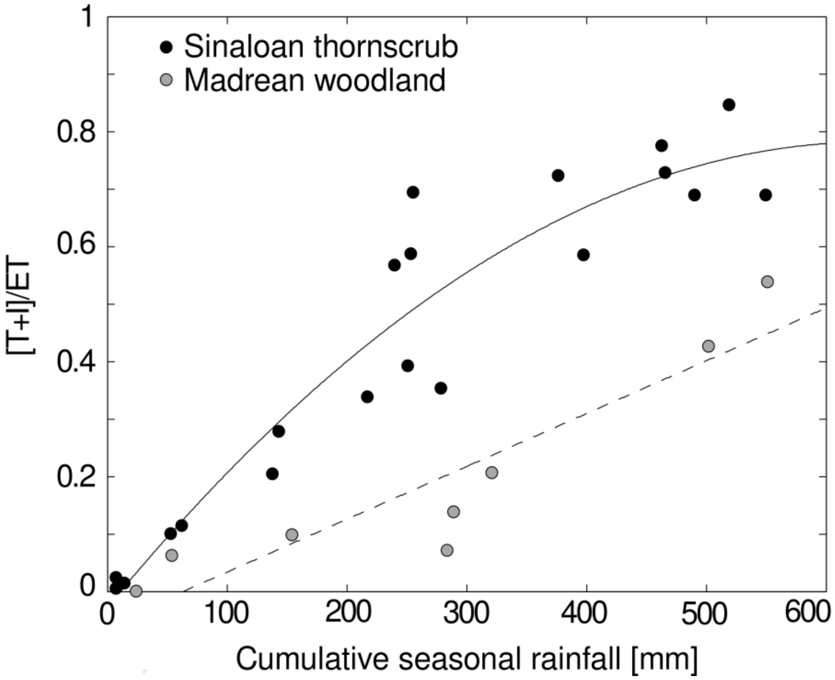

Figure 2.11. Relation of Vegetation-Mediated Fraction, (T+I)/ET, With Cumulative Seasonal Rainfall, Defined as the Current and Prior Month Totals. The Black Solid Line is a Regression for ST, While the Gray Dashed Line is a Regression for MW.

For the subtropical scrubland, however, a threshold of 390 mm in two-month total rainfall yields a change in the slope of the (*T+I*)/*ET* relation with P_{accm}, as compared to the linear increase in the MW site, indicating that additional rainfall does not appreciably increase vegetation-mediated losses. Nevertheless, the ST site sustains higher (*T+I*)/*ET* than the MW site at all rainfall amounts, indicating that subtropical scrublands have a greater ability to return soil moisture back to the atmosphere through (*T+I*)/*ET*. Since plant interception is larger at the MW site, this implies that transpiration at the ST site is more sensitive to low rainfall (higher slope for P_{accm} < 390 mm), while being less sensitive at higher accumulations (lower slope for P_{accm} > 390 mm), as compared to MW. The differences in *ET* partitioning in the two ecosystems are further explored in Figure 2.12 as the time-averaged seasonal evolution of T/T_{max} and E/E_{max}, where normalization is performed with maximum values over all summers. Time-averaged NDVI/NDVI_{max} is also shown to indicate vegetation green-up onset and duration.

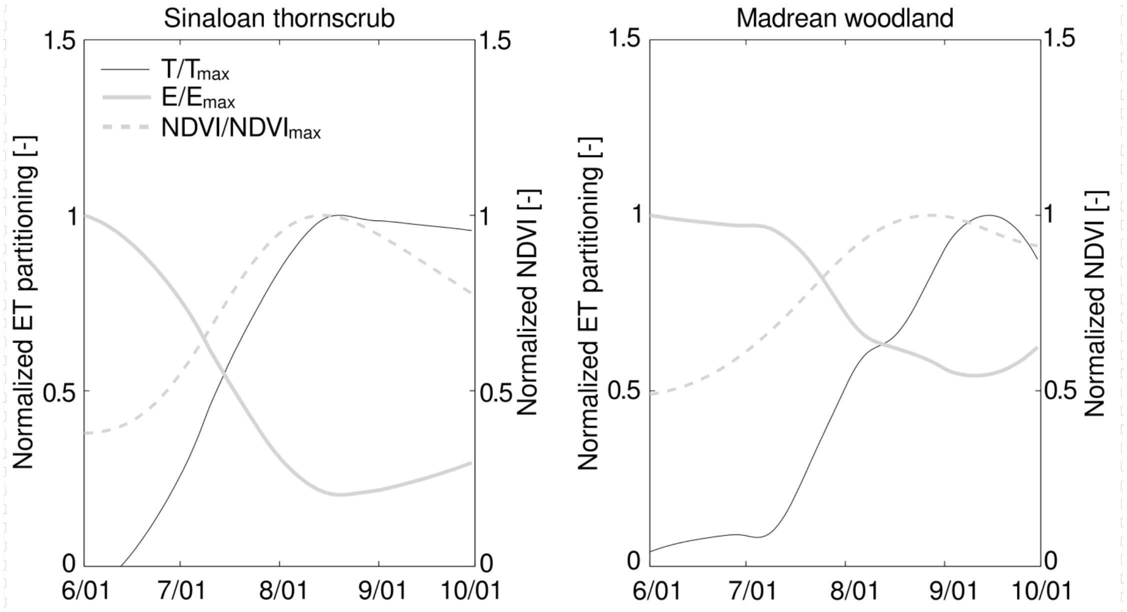

Figure 2.12. Seasonal Evolution of Normalized Evapotranspiration Components (T/T_{max} and E/E_{max}) and NDVI/Ndvi_{max} at the ST and MW Sites Averaged over Available Seasons.

Note that the seasonal evolution of E/E_{max} and T/T_{max} are inversely related since these losses represent the primary *ET* components (Table 2.5). The subtropical scrubland and oak savanna are both characterized by high E/E_{max} in the early summer prior to the onset of greening. At the ST site, the earlier and faster increase in NDVI to maximum canopy development ($\mathrm{NDVI}/\mathrm{NDVI}_{max} = 1$) yielded a quicker transition towards high T/T_{max} that is sustained throughout the summer. In contrast, the delayed green-up at the MW site results in high T/T_{max} only towards the end of the season, indicating that soil-mediated processes are significant in the oak savanna during a larger fraction of the summer as compared to the ST site (Table 2.5). As expected, the peak transpiration losses, $T/T_{max} = 1$, occur after the peak NDVI in both ecosystems as it takes times for vegetation greening to impact water and energy fluxes at each site. Interestingly, the delay between peak $\mathrm{NDVI}/\mathrm{NDVI}_{max}$ and peak T/T_{max} is on the order of five days in the subtropical scrubland and nearly three weeks (20 days) in the oak savanna.

Month	*Sinaloan thornscrub*			*Madrean woodland*		
	E/*ET* [%]	*T*/*ET* [%]	*I*/*ET* [%]	*E*/*ET* [%]	*T*/*ET* [%]	*I*/*ET* [%]
June	90.3	7.8	1.9	96.4	3.3	0.3
July	58.3	38.9	2.8	89.8	8.2	1.9
August	23.7	70.8	5.6	64.3	26.8	8.9
September	26.4	70.8	3.7	53.8	41.9	4.3
Total	39.0	57.4	3.7	77.4	18.6	4.0

Table 2.5. Evolution of Monthly *ET* Partitioning Into Soil Evaporation (*E*), Plant Transpiration (*T*) and Evaporation of Intercepted Rainfall (*I*) for the ST and MW Sites. Seasonal Totals are Shown as 'Total'. Values Represent Averages over All Summer Periods

This indicates that the MW site has a slower transpiration response to rainfall during the North American monsoon leading to a higher proportion of soil-mediated losses, as summarized in Table 2.5. Toward the end of the summer, E/E_{max} begins to increase in both ecosystems in response to the beginning of vegetation senescence, which lasts for different periods of time in each ecosystem (Méndez-Barroso et al., 2009; Forzieri et al., 2011).

2.4. Discussion and Conclusions

Seasonal vegetation greening affects the partitioning of water and energy fluxes in arid and semiarid ecosystems under the influence of the North American monsoon (e.g., Reynolds et al., 2000; Yépez et al., 2003, 2007; Scott et al., 2006; Watts et al., 2007; Vivoni, 2012). As a result, modeling applications that assume constant parameters or represent each summer with a fixed seasonal cycle can miss important vegetation impacts. In this study, we compared simulations that capture seasonally-varying parameters inferred from remotely-sensed data to static scenarios representing no canopy and full canopy conditions for two ecosystems that are representative of intermediate and high elevation landscapes along mountain fronts in the North American monsoon region. We found good agreement between field observations of evapotranspiration and soil moisture and simulations from Dynamic scenarios, indicating that the hydrologic model can represent interannual differences in the water and energy fluxes in the two ecosystems. In contrast, the Leaf off and Leaf on scenarios had a limited ability to track the seasonal evolution and interannual differences in *ET* and *SM* responding to precipitation-induced vegetation variations. While this result is robust over the five-summer period in the subtropical scrubland (ST site), additional data in the oak savanna (MW site) would be valuable for quantifying interannual ecosystem adjustments.

Precipitation events during the North American monsoon wet surface soils and induce a vegetation response that varies substantially across the two ecosystems. Early in the monsoon season, however, both ecosystems have dormant plants and soil evaporation is the dominant *ET* component. The switch toward transpiration dominance occurs differentially in each ecosystem such that it takes 2-3 weeks for the full transition to take place in the subtropical scrubland and 6-8 weeks in the oak savanna. These model-based estimates are consistent with field data in arid and semiarid ecosystems that respond to the North American monsoon (e.g., Mielnick et al., 2005; Scott et al., 2006; Yépez et al., 2007; Cavanaugh et al., 2011). Furthermore, the model identified, for the first time, which the peak transpiration losses are delayed by five days and twenty days, on average, from the peak NDVI at the ST and MW sites, respectively. A longer lag time between peak NDVI and transpiration at the MW site as compared to the ST site is likely due to the slower production of more costly leaves and ensuing activation of the photosynthetic process. This also suggests that rapid and robust vegetation greening in subtropical scrublands is linked directly to the dominance of vegetation-mediated losses, where *T*/*ET* was found to be 56 ± 9% over the five summer periods, well within the range of values at shrubland sites with a high vegetation cover (e.g., Scott et al., 2006). Recent efforts by Tarín et al. (2014) using an isotopic partitioning method found *T*/*ET* = 59 ± 6% at ST for four specific days. Model comparisons for these days revealed a standard error of estimates (SEE) of 0.16, with the match varying from a 16% to a 40% difference for individual days. To illustrate this, figure 2.13 shows the comparison between observed and estimated T/ET (fraction of evapotranspiration from plant transpiration).

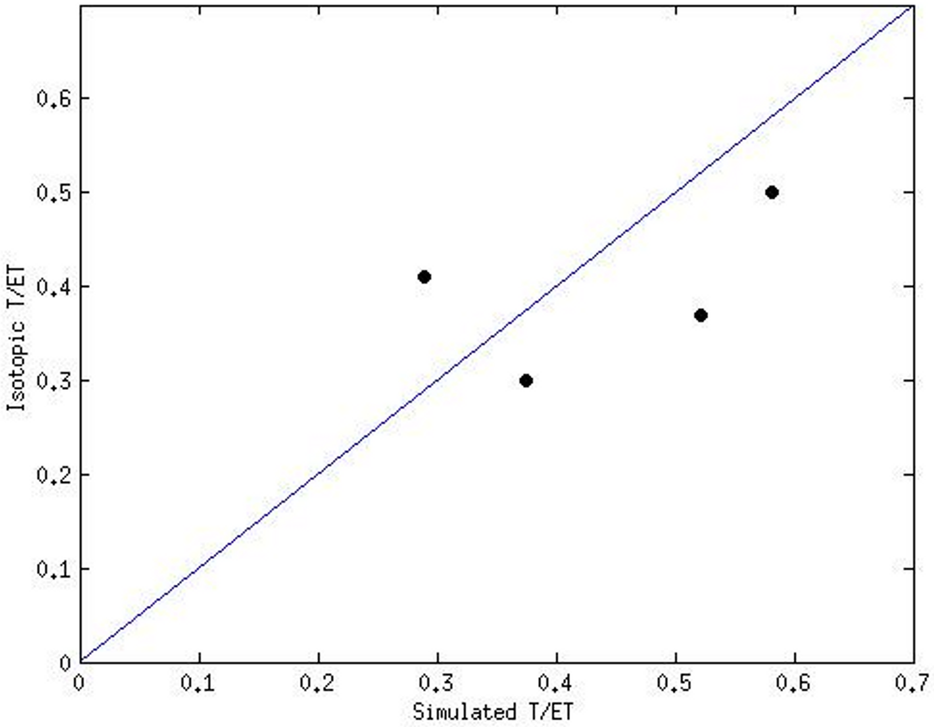

Figure 2.13. Comparison of Observed and Simulated T/ET (Fraction of Evapotranspiration from Plant Transpiration), Depicted as Black Circles. The Blue Line is a 1:1 Line. Observed Isotopic Fractions Were Obtained for July 24 and 27, 2007 and July 15-16, 2008.

This suggests that the model is capturing *ET* partitioning well under the limited conditions of the available data for the study periods. In contrast, delayed and attenuated vegetation greening in the oak savanna is responsible for soil-mediated losses having a dominant role throughout the season, with *T*/*ET* of only 18 ± 8%. The important role of soil evaporation in oak savannas has been recognized previously by Baldocchi and Xu (2007) and Pereira et al. (2009), but not placed in the context of summer vegetation greening.

Overall, the seasonal evolution of *ET* components indicates that transpiration is in-phase with vegetation greenness at the ST site, but out-of-phase (or delayed) at the MW site, a significant new insight provided through the model. This is consistent with a stronger link between cumulative precipitation and vegetation-mediated losses, (*T*+*I*)/*ET*, in subtropical scrublands as compared to oak savannas.

Based on long-term analyses of vegetation greening, Forzieri et al. (2011) found that deciduous subtropical ecosystems in the NAM region have high seasonality with a short period of intense greening occurring rapidly after precipitation onset. Mountain woodlands including oak savannas, on the other hand, were found to have more a prolonged period of moderate greenness that was delayed with respect to the precipitation onset but continued well into the fall season. Results described in this study identify the implications of the two ecosystem types on the water and energy fluxes, specifically on evapotranspiration and its partitioning, which have not been previously known. Intermediate-elevation subtropical scrublands have a high sensitivity to precipitation, primarily during the early development of the NAM, which allow them to quickly transition from soil- to vegetation-mediated losses to the atmosphere. These intensive water users rapidly deplete available soil moisture through transpiration, subsequently leading to decreases in vegetation greenness and transpiration near the end of the summer. In contrast, high-elevation oak savannas, with a lower sensitivity of canopy development to precipitation, have a slower transition from evaporation- to transpiration-dominated periods. As a result, these extensive water users slowly deplete soil moisture during the NAM, preserving it for subsequent use to maintain greenness and transpiration during the fall. As discussed by Rodríguez-Iturbe et al. (2001), variations in plant water use between intensive and extensive strategies may allow different ecosystems to occupy specific niches along the mountain front.

The noted variations in seasonal and interannual dynamics of *ET* and its components in the two ecosystems have a number of implications on the ecological and hydrologic properties of semiarid mountain fronts in the NAM region. First, the switch from soil- to vegetation-mediated losses affects soil moisture storage since evaporation is primarily sourced from shallower layers. The delayed transition at higher elevations implies that deeper soil water is preserved for longer periods, potentially leading to mountain recharge (Wilson and Guan, 2004). Second, the rapid transition towards transpiration in subtropical scrublands implies these sites are more likely to be responsible for the precipitation-soil moisture-vegetation feedback mechanism (Dominguez et al., 2008; Méndez -Barroso and Vivoni, 2010). Thus, the local precipitation recycling that sustains vegetation greening during the NAM may be sourced primarily from intermediate elevations along mountain fronts rather than higher elevations. Finally, spatially-variable consumption of precipitation in the different ecosystems through *ET* may have implications on runoff production (Robles-Morúa et al., 2012). However, the underlying processes that could distinguish runoff in subtropical scrublands and oak savannas have yet to be elucidated. Further, the model findings on the interannual variations of *ET* partitioning in the two ecosystems need to be corroborated by additional field studies, in particular at high elevation oak savannas. As demonstrated in this work, the comparative analysis of evapotranspiration and its partitioning in different ecosystems through the use of field observations, remote sensing estimates and hydrological modeling is a fruitful avenue of future work.

CHAPTER 3

IMPACT OF SPATIALLY VARIABLE SOIL TEXTURE AND THICKNESS ON SIMULATED ENERGY AND WATER FLUXES IN A SEMIARID BASIN

3. 1 Introduction

Soil depth exerts a strong control on the water and energy balance. It is widely accepted that thin soils can lead to the production of saturated overland flows while thicker soils can have more water storage capabilities affecting ecosystem processes (Boer et al., 1996; Bertoldi et al., 2006; Tromp-Van Meerveld and McDonnell, 2006, Gochis et al., 2010). Although, the controlling effect of soil depth and aspect could be important in semi-arid areas where water is the most limiting resource. Because soil depth acts as the main reservoir for water in semiarid ecosystems, it affects the partition of energy fluxes into sensible and latent heat at the land surface. Furthermore, it affects plant transpiration and carbon fixation depending on the temporal and spatial availability of soil moisture. For this reason, an accurate spatial representation of soil thickness at catchment scale is important to identify not only the spatial patterns in soil moisture, evapotranspiration rates and connectivity but also their persistence in time and space. Hydrological models can be an excellent tool to identify such patterns but requires an accurate representation of the spatial variability of soil thickness (Saulnier et al., 1997; Pelletier et al., 2009; Catani et al., 2010, Nicótina et al., 2011).

Soil depth mapping is not a feasible procedure because it requires a large number of sampling points and consumes a considerable amount of time; thus, we need to rely on models that can accurately predict the spatial patterns of soil depth. One widely used approach to estimate distributed soil depth is to develop empirical relationships between terrain attributes, such as slope and curvature with a limited number of soil thickness observations (Moore et al., 1993; Gessler et al., 1995; Heimsath et al., 1999, Catani et al., 2010). A less commonly used approach includes the assumption of a linear decreasing function between soil thickness with site elevation and topographic slope (Saulnier et al., 1997). Today is widely accepted that the relationship between soil depth and terrain curvature, assuming steady state conditions, is one of the most accurate ways to infer soil thickness (Heimsath et al., 1999; Dietrich et al 2003).

On the other hand, the piedmonts of the Sierra Madre Occidental, located in the North American Monsoon region (NAM), show complex topography. Consequently, this rugged topography produces large variations in both soil thickness and physical properties that may influence the spatial distribution and storage of water. Therefore, the semiarid basins located in the NAM region represent an opportunity to explore the effects of the variability of soil depth on water fluxes and states. Previous modeling studies in the region have found that simulated sensible and latent heat were considerably affected by soil thickness; thus, resulted in the improvement of model performance when observed soil depth was used instead of the standard 2 meters soil column from the Noah model (Gochis et al., 2010). Although this study represents an important contribution understanding the effect of soil thickness on water and energy fluxes in the region, this was performed at point scale and did not consider the spatial distribution of soil depth at basin scale.

In this study we evaluate the impact of variable soil thickness and soil texture in the temporal and spatial variability of basin evapotranspiration and soil moisture in a semiarid mountain basin under monsoonal regime. To do so, we performed ecohydrological simulations using the distributed model TIN-based Real-time Integrated Basin Simulator (tRIBS) during July through September of the year 2004. This year was selected in particular because the large change in vegetation greening and the high availability of ground data as part of the soil moisture experiment 2004 (SMEX04). We are interested to answer the following questions: How large is the impact of variable soil thickness and textural properties on model estimated water fluxes? How is the spatial representation of these simulated fluxes?

Finally, this research represents an unexplored pathway to evaluate model sensibility. Previous modeling efforts did not take into consideration the effect of spatially variable soil thickness on simulated fluxes. For this reason, this research work makes an important contribution to model users to evaluate model sensitivity. However, it is necessary to expand the soil sampling and evaluate the sensitivity analysis to different scales.

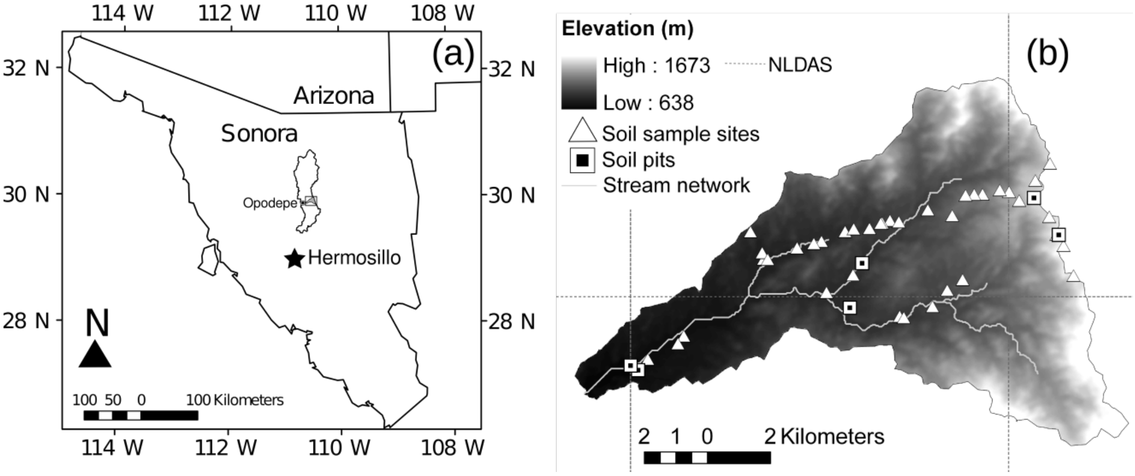

Figure 3.1. Location of the Sierra Los Locos Catchment. (a) Location of the San Miguel Basin Within the Mexican State of Sonora. (b) Sample Sites for Soil Texture Characterization. Triangles Shows the Location of Shallow Soil Samples and Squares Shows the Location of Soil Pits for Profile Analysis. Dashed Lines in (b) Show the Spatial Extension of NLDAS Forcing (North-American Land Data Assimilation).

3.2 Methods

3.2.1 Study Site

In order to evaluate the impact of soil depth on simulated water fluxes and states, we used different tools and sources of datasets that include: (1) a fully operational hydrological model with benchmark simulations in the NAM region, (2) Soil depth observations and a soil texture dataset (3) Raster and vector geospatial data for the region, and (4) an operational network of soil moisture sensors. The study site is located in the Sierra Los Locos basin (93.2 km^2) east of the small rural town of Opodepe and about 150 km northeast of the city of Hermosillo, capital of the Mexican state of Sonora.

Figure 3.1a shows the location of Sierra Los Locos basin that is nested inside the San Miguel River Basin (3796 km^2). Both basins are part of the Rio Sonora System, which is the main source of surface water for the capital Hermosillo, which is important for sustaining economic activities in this region. Figure 3.1b shows the physiographic characteristics of the Sierra Los Locos Basin. Rainfall distribution and local elevation has a large influence in the vegetation types in Sierra Los Locos Basin. The basin relief is 1035 meters with lower elevations dominated by subtropical scrubland; while oak woodlands and grasses dominate higher elevations. Local topography influences rainfall distribution, varying from 500 to 700 mm/year with close to 70 % falling during the North American Monsoon (Xiang et al., 2014). Several studies in the North American Monsoon region have shown that these highly seasonal rainfall pulses lead to a dramatic change in vegetation greening, which affected the surface water and energy partition (Méndez-Barroso et al., 2014). For this reason, this research has incorporated dynamic vegetation during model simulations in order to emulate seasonal surface conditions. Basin boundaries and river networks were delineated using a 30-meter resolution digital elevation model (DEM) from Advance Spaceborne Thermal Emission and Reflection Radiometer (ASTER).

3.2.2 Soil Thickness Observations and Soil Texture Samples

Two soil-sampling activities were carried out in August 2007 at Sierra Los Locos Basin. One of the survey activities consisted of estimation of soil depth and characterization of soil horizons from six soil pits distributed in several sites in the Sierra Los Locos basin. Soil pits database contained soil thickness, number of horizons, horizon depth, color (Munsell color system) and texture. Soil pits sites represented different terrain characteristics such as elevation, slopes, and vegetation cover. The second sampling activity consisted of taking surface soil samples (0-5 cm depth) at forty-two sites distributed from the basin headwaters to the outlet. Soil samples were taken to a laboratory in order to determine particle size (texture) and bulk density. Bulk density was estimated by the clod method (Blake, 1965), while relative masses of sand, silt and clay were determined by the “Pipette” method (Gee and Bauder, 1986). The soil textural class was determined by the USDA triangle method by using the results from the soil particle size analysis. Figure 3.1b shows the location of soil pits (dark squares) and surface soil samples sites (triangles). Soil thickness was correlated with local curvature to estimate the spatial distribution of soil depth while soil textural classes were correlated with surface radiance to infer the spatial distribution of soil textural properties.

3.2.3 Methods to Estimate the Spatial Distribution of Soil Thickness

Surveying soil depth is not a simple task and it requires considerable amount of resources. For this reason, it is feasible to apply simple models to estimate the spatial distribution of soil thickness. Although there is not a consensus about one universal model to estimate soil thickness, there are several empirical models that relate soil depth with topographic features. The first method evaluated in this work used an empirical approach that related soil depth with local terrain elevation (Saulnier et al., 1997). This method assumed a linear decreasing function between soil thickness and elevation and was used to perform a sensitivity analysis to evaluate the effect on soil depth from TOPMODEL outputs for the Maurets Catchment in France. This method will be referred hereafter as the Saulnier-z method:

$$h_i = h_{max} - \left[\frac{z_i - z_{min}}{z_{max} - z_{min}}\left(h_{max} - h_{min}\right)\right] \;; \qquad (3.1)$$

where h_i is depth to bedrock at pixel i, z_i is local elevation estimated by a 30-meter ASTER (Advance Spaceborne Thermal Emission and Reflection radiometer) digital elevation model, z_{min} represents the minimum elevation found in the basin, z_{max} represents the maximum elevation in the basin, h_{max} is the maximum observed soil depth, and h_{min} represents the minimum observed soil depth. Saulnier et al., 1997 also developed an alternative method for soil depth estimation assuming a linear relation between soil thickness and terrain slope. This method is referred hereafter as Saulnier-Slope method:

$$h_i = h_{max} - \left[1 - \frac{tan\theta_i - tan\theta_{min}}{tan\theta_{max} - tan\theta_{min}}\left(1 - \frac{h_{min}}{h_{max}}\right)\right] \;; \qquad (3.2)$$

where $tan\theta_i$ is the local calculated slope using ArcGIS 9.3 Spatial Analyst from 30-meter resolution DEM, θ_{min} is the minimum calculated slope found in Sierra Los Locos basin and θ_{max} is the maximum calculated slope in the basin. The third approach used to estimate the spatial distribution of soil thickness is based on a multi-linear regression approach between plane curvature, topographic index and soil depth (Gessler et al., 1995). The authors performed a multiple regression with Poisson Error Function between several terrain attributes and sixty soil depth observations in a 100-km^2 semiarid basin in Australia. The evaluated terrain attributes included: terrain slope, aspect, elevation curvature and topographic index (TI). However, they found that topographic index and plane curvature were highly significant in predicting soil thickness. We estimated the topographic index in Sierra Los Locos basin based on the idea of Beven and Kirby, 1979:

$$TI = ln\left(\frac{CA}{tan\theta}\right) ; \qquad (3.3)$$

where CA is the upslope contributing area and θ is the local slope gradient. Contributing area was calculated using flow accumulation estimated by the method of Jenson and Domingue (1988) while slope gradient was estimated using spatial analyst in ArcGIS 9.2. Multi-linear regression was performed by using pixel values of curvature and topographic index at the location of the soil pits as independent variables of soil thickness. Regression statistics were obtained in Matlab using the function "regress". This method is named hereafter as the Gessler method. Finally, the last method evaluated to estimate soil thickness relied on the relation between terrain curvature with soil thickness, assuming steady state conditions. Today, this relationship is widely accepted as preferred way to infer soil thickness from terrain attributes (Heimsath et al., 1999; Dietrich et al., 2003). This method is referred later in this work as the Heimsath method. We performed a linear regression analysis by extracting local curvature from the soil pit locations and used this information as independent variables for predicting soil thickness. Local curvature was estimated on ASTER 30-meter resolution digital elevation model using Spatial Analyst tool within ArcGis 9.2. Curvature of the surface is estimated on a cell-by-cell basis using a fourth-order polynomial:

$$Z = Ax^2y^2 + Bx^2y + Cxy^2 + Dx^2 + Ey^2 + Fxy + Gx + Hy + I; \qquad (3.4)$$

This equation is fit to a 3 x 3 pixel window. Then, “Z” is the elevation value corresponding to the local pixel, hence, there are nine values of elevation where Z1 corresponds to the upper left corner of the 3 x 3 matrix and Z9 corresponds to the lower right corner of the 3 x3 matrix. Two coefficients are required for the computation of curvature where Z5 corresponds to the central pixel of the 3x3 window and L corresponds to the dimension of the pixel:

$$J = \frac{\left[\frac{Z4+Z6}{2-Z5}\right]}{L^2} \quad ; \qquad (3.5)$$

$$K = \frac{\left[\frac{Z2+Z8}{2-Z5}\right]}{L^2} ; \qquad (3.6)$$

Then the output of the curvature is the second derivative of local elevation:

$$curvature = -2(J + K) * 100 \quad ; \qquad (3.7)$$

Estimated soil thickness maps by all approaches were smoothed and resampled to a final spatial resolution of 120-meter. The goal of raster smoothing is to reduce the difference between adjacent pixels and avoid large gradients in soil depth that can induce preferential groundwater flows. Raster resampling was performed using ArcGIS 9.3 with the application of the bilinear interpolation method. This method used the values of the four nearest input cell centers to determine the value on the output raster. The new values from the output cell are a weighted average of these four values, adjusted to account for their distance from the center of the output cell.

3.2.4 Remote Sensing Data and Estimation of Soil Textural Classes

Understanding the spatial distribution of soil texture is essential to understand the spatial variability of hydrological properties, such as hydraulic conductivity, porosity and water holding capacity. Recent studies have indicated that soil texture correlates significantly with soil reflectance in the visible and near infrared regions (Zhang et al., 1992 and Sullivan et al., 2005). Much of the research in soil texture estimation involved Landsat images, but the Advanced

Spaceborne Thermal Emission and Reflection Radiometer (ASTER) can offer very high spatial resolution in the visible-near infrared region (15 meters in green, red and near infrared bands), short and long wave infrared (30 and 90 meters respectively). Therefore, ASTER reflectance and/or radiance can be used to explore the spectral signature of soil texture.

We used an ASTER image of Sierra Los Locos Basin during the dry season to allow exposition of bare soil. ASTER overpassed the region on May 15, 2008, and the L1B registered radiance at the sensor was used for image processing. ASTER digital numbers (DN) of all bands (1-14) were converted to radiance by multiplying DN times a unit conversion coefficient, specific for each band. The pixel values of radiance for all ASTER bands were extracted at the locations of the soil surface sampling points (Figure 3.1b). ASTER's radiance was grouped in four dominant textural classes found in Sierra Los Locos Basin: Sandy clay loam, sandy loam, loamy sand and sand. The mean and standard deviation of ASTER's radiance was calculated for every soil class and plotted with their corresponding band number. The scatter plot with band number in the x-axis and band radiance in the y-axis will show the response of ASTER bands to soil composition. The bands that show significant differences in radiance among textural classes were selected to allow image classification. More details about ASTER radiances processing and estimation of textual properties map are described in Appendix D.

Statistical information of the selected bands was obtained by cluster analysis and later was used within an unsupervised classification approach (Maximum Likelihood). Both Analyses were performed using the Spatial Analyst module (Arc-GIS 9.3) and the final soil texture map was identified later as “ASTER”. One of the maps used for the sensitivity analysis was generated by the National Institute of Statistics and Geography (INEGI, for acronym in Spanish). Finally, the last map used in the analysis was generated using a slope ranges criteria. This map was used on previous hydrological simulations in Sierra Los Locos Basin. For further details about this latter map the reader should reference Vivoni et al. (2010).

ID	*Bedrock Data*	*Mean soil depth [m]*	*Soil texture data*	*Simulation ID*
1	Uniform	1.5	Slope-based	B
2	Uniform	1.5	ASTER-based	UB+A
3	Uniform	1.5	INEGI	UB+I
4	Uniform	1.5	Uniform sandy-loam	UB+Sal
5	Uniform	1.5	Uniform sand	UB+Sa
6	Uniform	1.5	Uniform loamy sand	UB+lSa
7	Uniform	1.5	Uniform sandy clay loam	UB+SaCl
8	Gessler	0.80±0.46	Slope-based	G+V
9	Heimsath	0.83±0.50	Slope-based	H+V
10	Saulnier_slp	1.53±0.28	Slope-based	S+V
11	Saulnier_z	1.19±0.42	Slope-based	Z+V
12	Gessler	0.80±0.46	ASTER-based	G+A
13	Heimsath	0.83±0.50	ASTER-based	H+A
14	Saulnier_slp	1.53±0.28	ASTER-based	S+A
15	Saulnier_z	1.19±0.42	ASTER-based	Z+A
16	Gessler	0.80±0.46	INEGI	G+I
17	Heimsath	0.83±0.50	INEGI	H+I
18	Saulnier_slp	1.53±0.28	INEGI	S+I
19	Saulnier_z	1.19±0.42	INEGI	Z+I
20	Uniform	1.0±0.34	Slope-based	U+V
21	Uniform	1.0±0.34	ASTER-based	U+A
22	Uniform	1.0±0.34	INEGI	U+I

Table 3.1. Simulations Carried Out in Sierra Los Locos Basin. The Table Shows All Different Combinations of Distributed Soil Depth and Textural Classes. Furthermore, Two Uniform Soil Depths and 4 Uniform Textural Classes Were Evaluated.

3.2.5 Model Description and Forcing

Numerical simulations of hydrological variables were carried out in Sierra Los Locos basin using a distributed hydrological model. The hydrological model tRIBS (TIN-based Real-time Integrated Basin Simulator) represents the basin by a Triangulated Irregular Network (TIN) consisting of elevation, stream and boundary nodes that captures the basin's geometry and reduces the number of computing elements compared to the original DEM (Vivoni et al., 2004). The model uses Voronoi polygons (associated with TIN node similarly to Thiessen polygons) as a finite volume domain for water and energy calculations. The hydrological model tRIBS has been widely used in the North American Monsoon region and has demonstrated good performance in estimating water fluxes and states (Vivoni et al., 2010) ET partitioning (Méndez-Barroso et al., 2014), and surface temperature (Xiang et al., 2014).

Sierra Los Locos Basin boundaries and TIN were delineated using an ASTER 30-meter resolution digital elevation model producing 49390 Voronoi polygons in the basin. Hydrological simulations were carried out in parallel mode (distribution of tasks over multiple processors at once) on Saguaro high-performance computer at ASU-Advance Computer Center, and encompassed the summer monsoon of the year 2004 (June 1st to September 30). For details of model parallel operation, the reader can refer Vivoni et al. (2011). The domain of the Sierra Los Locos Basin was divided in fifteen processors using reach-based partitioning. We used ground-corrected meteorological grids from the North American Land Data Assimilation System, version 2 (NLDAS-2) as the rainfall and meteorological forcing for model simulations. The spatial resolution of the meteorological forcing grids is 12-km (0.125°), and was converted from the standard GRIdded Binary format (grib) to ESRI ascii format, which is the required format for the hydrological model. Figure 3.1b shows the spatial coverage of NLDAS pixels (gray dashed lines) in relation with basin domain. The NLDAS-2 meteorological variables used to force the model included: Atmospheric pressure (PA), relative humidity (RH), incoming short wave radiation (IS), air temperature (TA), wind speed (US), and precipitation (RA). Our NLDAS datasets were corrected from ground observations using the approach by Robles-Morúa et al. (2012) based on the application of an averaged ratio of means multiplicative factor from Steiner et al. (1999). Soils and land cover attributes followed the model parameterization of Xiang et al. (2014).

It is well know that catchment response to rainfall is non-linear phenomena and a possible cause in non-linearity in runoff production is the difference in response time between surface and subsurface flows. The model tRIBS is able to simulate four basic runoff mechanisms: Infiltration-excess runoff (Horton, 1933), saturation-excess runoff (Dunne and Black, 1970), groundwater-exfiltration (Hursh and Bratter, 1941) and perched return flow (Weyman, 1970). Total runoff is estimated as the sum of these four mechanisms. Saturation and infiltration excess runoff are quick surface response as soil properties allow water to move deeper. Conversely, perched return flow and groundwater exfiltration have slower response as subsurface flow delay the response to rainfall. Furthermore, runoff production from multiple mechanisms will vary with the rainfall and landscape factors that influence the coupling of surface and subsurface flows (Vivoni et al., 2007). Finally, it is important to reiterate that the meteorological forcing, seasonal evolution of vegetation parameters, land cover types and soil parameters did not change in all simulations cases. Only the spatial distribution of soil texture and soil thickness was changed.

3.2.6 Model Initialization and Boundary Conditions

The goal of this research is to evaluate the effect of variable soil thickness and texture on simulated water and energy fluxes. In order to do so, we performed a sensitivity analysis using a previous calibrated hydrological model simulation (Xiang et al., 2014). We evaluated different combinations of data sources and soil depth scenarios, for example: four variable soil depth maps (Saulnier-z, Saulnier-slp, Heimsath and Gessler) with three distributed soil texture maps (INEGI, slope-based and ASTER) resulting in twelve different simulations. Furthermore, we evaluated two uniform soil depths (1.5 and 1.0 meters) with three soil texture maps (6 simulations) and four uniform textural classes (sand, sandy-loam, sandy-clay-loam and loamy sand) at 1.5 meters soil depth (4 simulations). Therefore, we evaluated a total of twenty three different combinations of soil depth and texture. Table 3.1 shows the hydrological simulations evaluated in the sensitivity analysis. Model initialization included a period of dry conditions prior to the calculation of basin fluxes. This dry period is known in modeling as “spin-up” process, which allowed depleting the water table and emulated dry conditions before the monsoon onset. The spin up period occurred from May 1st to May 31st, 2004. For consistency, all model simulations experienced dry conditions at the beginning of the model simulation (water table and bedrock depths had the same value).

3.3. Results and Discussion

3.3.1 Distributed Soil Texture and Thickness

Figure 3.2 shows the differences in the spatial distribution of soil thickness among the methods evaluated in this research. Figure 3.2a shows the estimated spatial distribution of soil depth by applying the method developed by Saulnier et al. (1997), and based on the assumption of a linear relation between elevation and soil depth (Saulnier-z). This method showed the second highest basin-averaged soil depth with a mean value of 1.19 (±0.42 m). Furthermore, it is evident that soil depth mimics the elevation patterns at Sierra Los Locos basin. Shallower soils were found on the highest elevations (south-east and north-east regions of basin), while deepest soil thickness was found in the western region, near the basin. Map accuracy in relation with soil thickness observations was about three times larger in absolute errors than the most accurate map (38.4 cm, see table 3.2 for reference).

Therefore, the assumption of a linear relation between soil depth and elevation is not valid in this semiarid basin, which it is characterized by complex topography. Secondly, figure 3.2b shows the spatial distribution of the estimated soil depth by applying the Saulnier-slope method. This method showed the deepest basin-averaged and the lowest spatial variability with a mean value of 1.53 (±0.28 m). Soil depth distribution is less smooth than the Saulnier-z method resulting in sudden changes in soil depth as observed in the central and western portion of the Sierra Los Locos Basin. Shallower soil thickness was found on steepest surfaces (central, northeast and east of Sierra Los Locos Basin), while deep soils were found in the west region, near the basin outlet. This method showed the least reliable prediction of soil depth with a mean absolute error of 92.4 centimeters (Table 3.2).

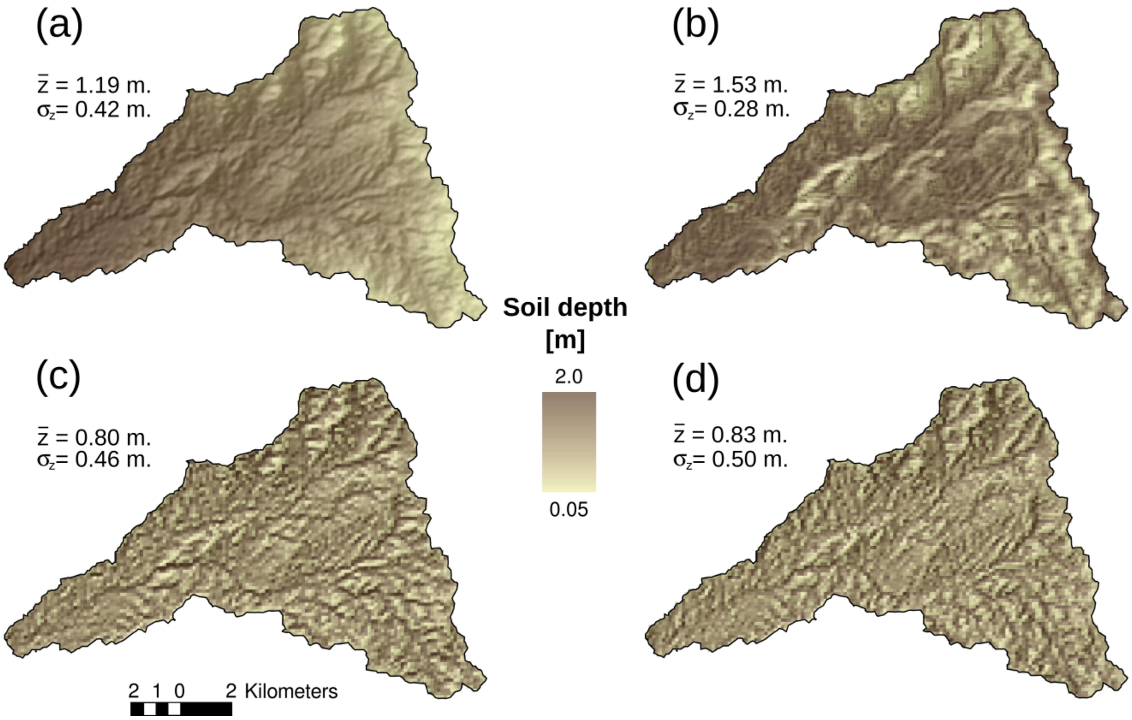

Figure 3.2. Comparison in Soil Depth Estimated With Different Methods. (a) The Saulnier-Z (z=Elevation, Saulnier Et Al., 1995) (b) Saulnier-Slope (Saulnier et al., 1995). (c) Gessler Method (Gessler et al., 1997) and (d) Heimsath Approach (Heimsath et al., 2003).

As indicated in the method developed by Gessler et al., 1995, a multivariable linear correlation between observed soil depths, wetness topographic index and terrain curvature was conducted. It was found that these two later variables were highly correlated ($p < 0.01$, R^2=0.77) to soil depth as expressed in the following regression equation:

$$Soil\ depth\ (cm) = 37.12 + 3.31TWI - 242.19curv + 5.98TWIcurv\ ; \qquad (3.8)$$

where *TWI* is wetness topographic index and *curv* is terrain curvature expressed as 1/100 m, and calculated from 30-m digital elevation model.

Soil texture map	*Correct pixels (%)*
ASTER-based	68
Slope-based	56
INEGI	53
Soil depth map	*Absolute error (cm)*
Gessler	11.6
Heimsath	15.5
Saulnier-z	38.4
Saulnier-slope	92.4

Table 3.2. Accuracy of Estimated Soil Texture and Thickness Maps. Pixel Value of Soil Depth and Texture at the Sampling Sites Were Compared to Ground Observations.

The Gessler method (figure 3.2c) obtained the shallowest basin-averaged soil depth with a value of 0.80(±0.46 m). Furthermore, this method showed the most reliable performance in estimated soil depth with an absolute error of 11.6 centimeters. Finally, we performed a linear relation between terrain curvature and observed soil depth as suggested in the method of Heimsath et al., 1999. We found that curvature had a significant and close relation with soil depth ($p < 0.01$, $R^2=0.71$), and it can be used as a proxy for soil depth as expressed in the following regression equation:

$$Soil\ depth\ (cm) = -198.82curv + 79.9\ ; \qquad (3.9)$$

where *curv* is terrain curvature calculated from 30-m digital elevation model. Both methods of Heimsath and Gessler showed similar spatial representation of soil depth in Sierra Los Locos Basin. Nevertheless, the Gessler method has a slightly clearer representation of the stream network and floodplains, however; basin average soil depth is quite similar between these two methods. The Heimsath method obtained the second shallowest basin averaged soil depth with a mean value of 0.83 (±0.50 m).

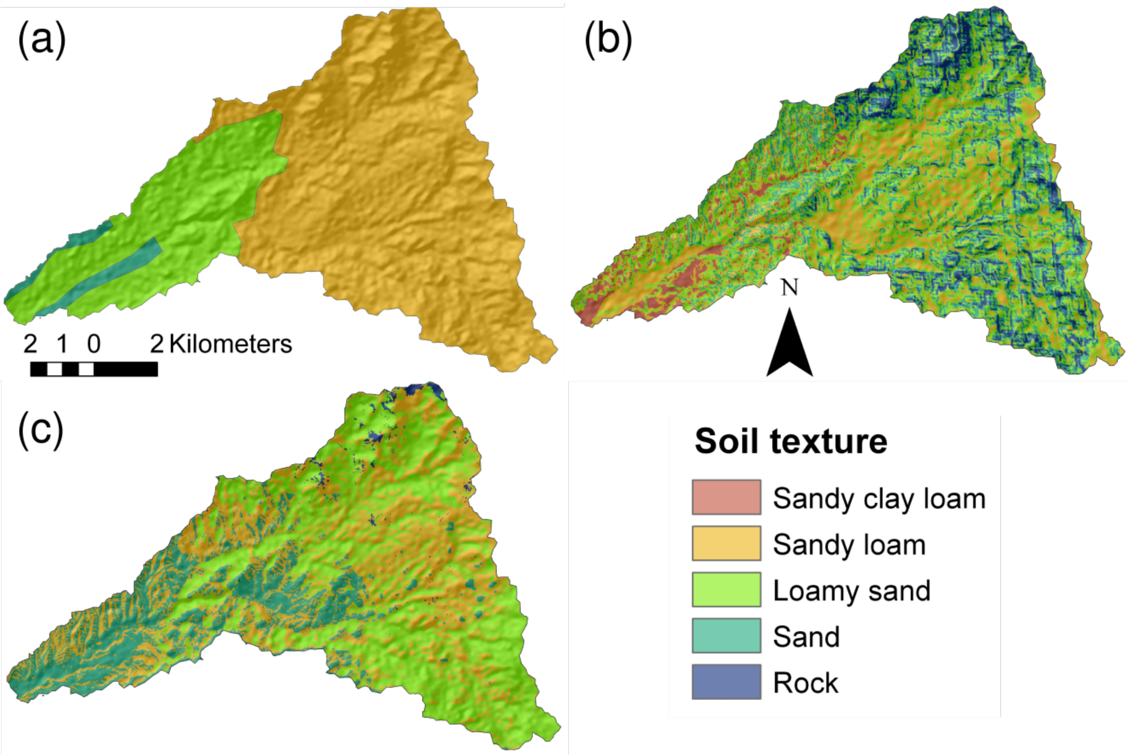

Figure 3.3. Comparison of Different Soil Texture Products. (a) Soil Texture Distribution From INEGI (Mexican Institute Of Geography and Statistics). (b) Slope-Derived Soil Texture Map from Vivoni et al., 2010 And (c) ASTER (Advance Spaceborne Thermal Emission and Reflection) Based Map.

Accurate spatial representation of basin or catchment properties such as soil texture, which it is the major factor influencing hydrological properties, is still a challenge in semiarid areas due to the lack of observations and the coarse information of the midsize basins or small catchments. For instance, INEGI's soil map (figure 3.3a) illustrates three soil textural classes with a clear pattern moving from coarser textural soil in the east (sandy loam) to finer soil texture near the basin outlet in the west (loamy sand) including some coarser material in the main floodplain (sand). However, the coarser resolution of INEGI map does not capture the variability in soil texture along the stream network and local topography. One attempt to improve the spatial distribution of soil texture in Sierra los Locos was carried out by Vivoni et al., 2010. This map relied on the assumption that soil texture is closely related to terrain attributes such as slope under the assumption that high gradient have shallow soils.

In this research, the approach of Apan et al., 2002 and Liao et al., 2014 was used to infer spatial patterns of soil texture using remote sensing data. This approach accounted for the emission, absorption or reflectance of electromagnetic energy at several wavelengths, thus is related to target composition or structure. We found that ASTER's visible and thermal bands showed large differences in radiance (emission) among the soil textural classes found in Sierra Los Locos Basin. For example: sandy-loam and sand had larger differences in radiance on bands 1 (green), 2 (red) and 3 (near infrared), whereas thermal bands 12 and 13 helped to distinguish between loamy sand and sand. Such bands were used as input for cluster analysis and for maximum likehood classification with four classes. Figure 3.3c shows the spatial distribution of soil textural types generated with ASTER radiance. Similarly to Vivoni et al., 2010 map, we found that the upper part of the basin was dominated by sandy loam and/or loamy sand. However larger discrepancies among the maps were found in the lower part of the basin (west) with sand dominating the ASTER-based textural distribution whereas INEGI was dominated by sandy loam with sand in the flood plains. In the map of Vivoni et al., 2010 there is not a particular soil type dominating the lower part of the basin. The results validated that ASTER had the highest accuracy in comparison with ground samples (68 % of correct pixels, see table 7), whereas Vivoni and INEGI had 56% and 53 % of correct pixels respectively.

3.3.2 Basin-Scale Water Balance in Sierra Los Locos

Figure 3.4 shows the basin-scale components of the water balance at the Sierra Los Locos Basin. Benchmark simulation was already calibrated using ground observations of soil moisture and MODIS land surface, according to the methods of Xiang et al. (2014) and Vivoni et al. (2010). Figure 3.4a shows the temporal evolution of surface soil moisture (5 cm. depth) and root zone soil moisture (1 m. depth). The model was able to represent the transition from extreme dry conditions at the beginning of the monsoon season to relative humid conditions during the monsoon onset. Soil moisture responded to rainfall pulses in June and mid-July as expected. Surface soil moisture during this period increased significantly due to rainfall pulses with large inter-storm periods.

Parameter	*Variable (unit)*	*Rock*	*Sand*	*Loamy sand*	*Sandy loam*	*Sandy clay loam*
Saturated hydraulic conductivity[1]	K_s [mm/h]	9.0	25	36.3	25.0	4.7
Saturated soil moisture content[1]	θ_s *[-]*	25	1662	598	241	98
Residual soil moisture content[2]	θ_r*[-]*	0.009	0.010	0.005	0.015	0.058
Pore size distribution index[3]	*m [-]*	0.17	0.60	0.45	1.50	0.32
Air entry bubbling pressure[3]	ψ_b *[mm]*	0	0	0	0	0
Conductivity decay parameter[4]	*f* $[mm^{-1}]$	0.01	0.01	0.025	0.001	0.001
Conductivity anisotropy ratio[4]	A_s *[-]*	600	600	600	600	600
Soil porosity[1]	*N [-]*	0.385	0.437	0.437	0.453	0.398
Soil heat conductivity-dry[5]	k_s *[J/msK]*	1.2	1.2	1.2	1.2	1.2
Soil heat conductivity-wet[5]		1.3	1.3	1.3	1.3	1.3
Soil heat capacity-dry[5]	C_s $[J/m^3K]$	6×10^5	6×10^5	6×10^5	6×10^5	6×10^5
Soil heat capacity-wet[5]		1.3×10^6	1.3×10^6	1.3×10^6	1.3×10^6	1.3×10^6

Table 3.3. Model Parameters for Soil Types in Sierra Los Locos Basin. Source of Model Parameters are as Follows: (1) Rawls et al. [1983] and Schaap et al [2003] With Modifications During Calibration. (2) Minimum Observed Soil Moisture. (3) Vivoni et al. [2010]. (4) Model Calibration. (5) Ivanov et al. [2008] And Vivoni et al. [2010] With Modifications During Calibration.

Furthermore, soil moisture rapidly decreases leading to pronounced recession limbs caused by sudden drying periods. In contrast, soil moisture decays slowly during August and September as a result of a continuous rainfall that led to higher soil moisture. In general, the model represents well the soil-drying period during the late-monsoon (Mid-August through early September) season in which vegetation is fully developed (high values of NDVI, figure 3.4a).

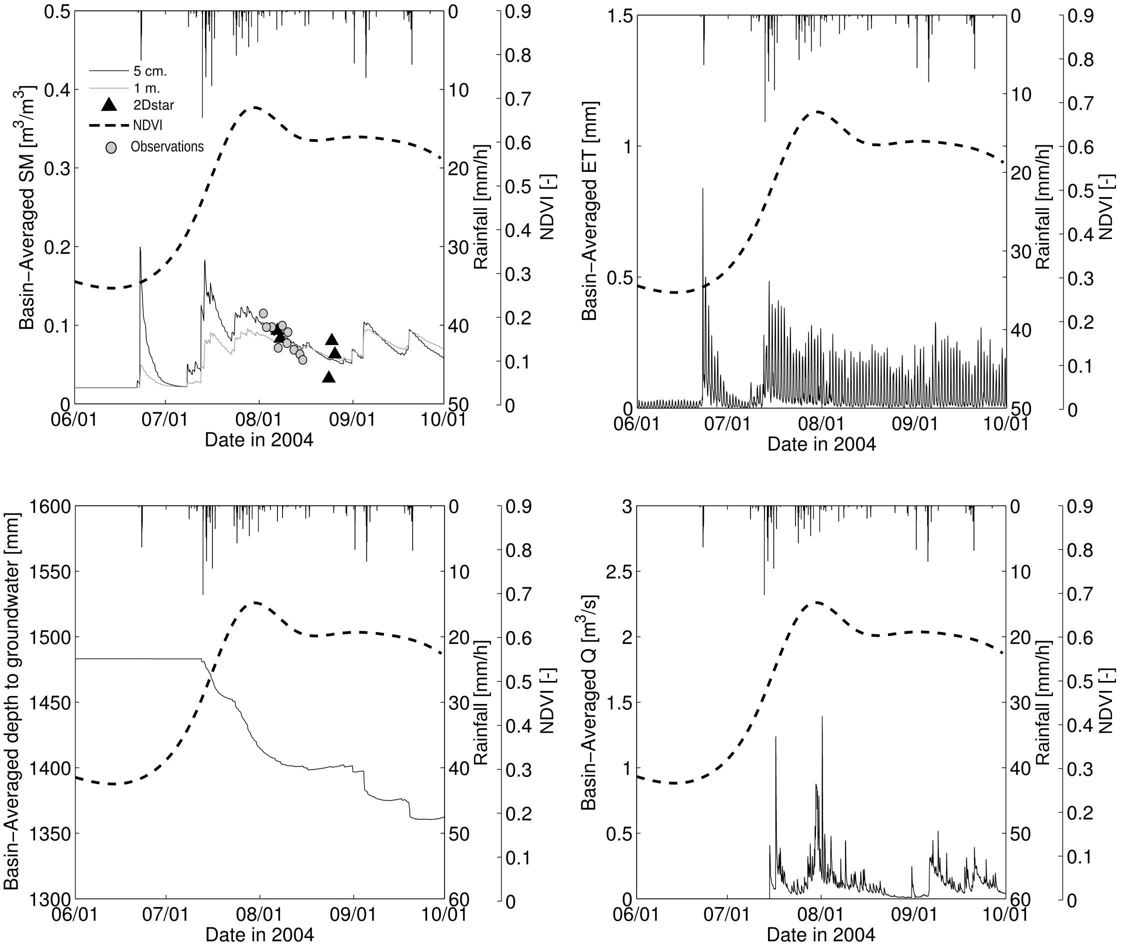

Figure 3.4. Basin-Average Water Balance During the Monsoon Season 2004 (July to September). (a) Basin Average Estimate Soil Moisture at Two Different Depths (Five Centimeters and One Meter) in Relation With Remotely Sensed Surface Soil Moisture (2D-STAR) and Daily Observations Along a Transect (Grey Dots). (b) Basin-Average ET. (c) Basin-Averaged Depth to Groundwater and (d) Basin Average Discharge at the Catchment Outlet. The Dashed Lines Presents the Time Series of Vegetation Greening Expressed as Basin-Averaged Normalized Vegetation Index (NDVI) from MODIS.

This later statement can be demonstrated by the comparison between basin- average estimated surface soil moisture and basin-average readings of shallow soil moisture retrieved from the L-band radiometer of the 2D Synthetic Aperture Radar (2DSTAR) that overflew the San Miguel Basin in 2004 (Ryu et al., 2010). In particular, there is a moderate correlation between estimated and observed soil moisture during the relatively wet period in mid-August (R^2 = 0.54). The soil moisture observations from 2DSTAR tend to have drier soil moisture in late August and early September leading to larger discrepancies. Evapotranspiration (ET) also responded rapidly to rainfall, specifically before the monsoon onset. Similarly to soil moisture, ET responded quickly to rainfall pulses in late-June early July with a sudden increase in ET fluxes (largest ET fluxes during the season) but also experienced a fast recession which is a typical behavior of water fluxes at the beginning of the monsoon season. Figure 3.4b also shows how vegetation exerts a strong control in evapotranspiration fluxes in this site. As observed, there is a transition in ET from spike-like fluxes in late June to steady fluxes from mid-July to the rest of the monsoon season. In addition, there is a small peak in ET fluxes in mid-July that coincides with the rising limb in the NDVI curve. After NDVI reached its maximum, there was an in-phase relation between NDVI and ET; for example, the clear decrease in NDVI during mid-July to mid-August coincides with the reduction in ET fluxes during the same period and later entering to quasi-stable conditions in September.

As shown in figure 3.4c, basin-averaged depth to groundwater slightly increased at the end of the monsoon season with a small ten centimeters increase in the groundwater table. Despite the sporadic rainfall events in late June and early July, the groundwater level remained static during the first month of the period of simulation. Notwithstanding, there was a steady increase in groundwater level during July ($\Delta h = 75$ mm) as a result of continuous rainfall events that occurred within this month. There was a small intra seasonal drought period in August that led to the return of stable groundwater levels. There was a brief period of drought (consecutive days without rain) within the monsoon season and had a considerable impact on surface water fluxes and vegetation greening that is clearly confirmed with a sudden drop in NDVI and ET values in mid-August. Again, groundwater level decreased in September as a result of increased precipitation, which led to a final groundwater depth of 1375 mm. Similarly to groundwater levels, surface discharge at the basin outlet remained without base flow during the first month of the study period although there were some rainfall events.

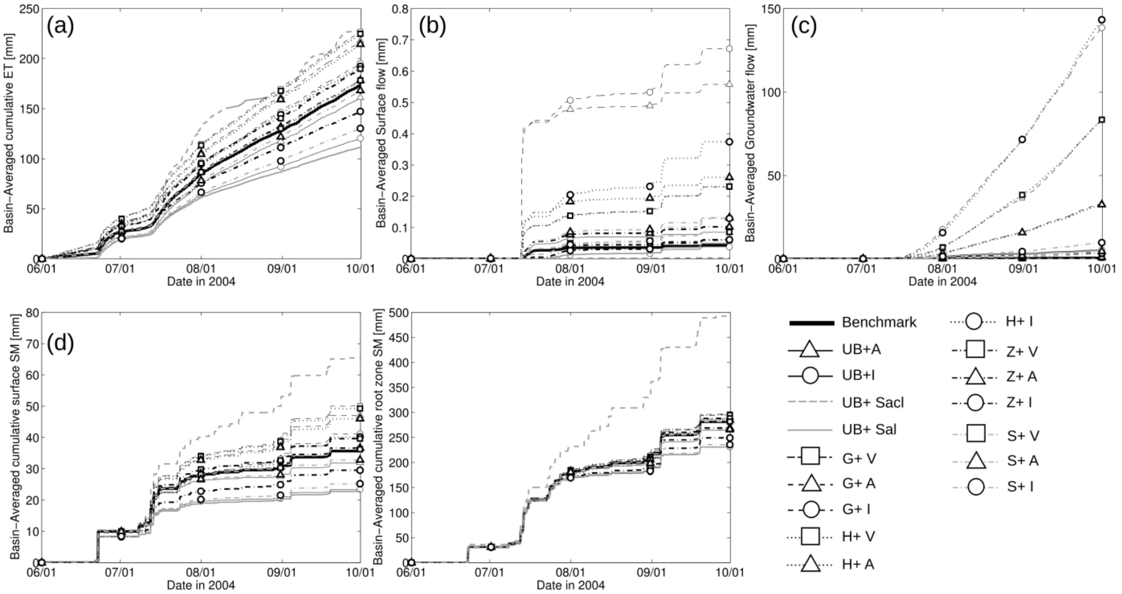

Figure 3.5. Comparison of Hydrological States Between the Benchmark Simulation (Solid Bold Black Line) With a Set of Alternative Model Simulations. The Simulations are: Benchmark+ASTER Soil Depth (UB+A), Benchmark+INEGI Soil Depth (UB+I), Gessler Soil Depth+Vivoni Soil Texture (G+V), Heimsath Soil Depth With Vivoni Soil Texture (H+V), Saulnier-Slp Soil Depth+ Vivoni Soil Texture (S+V) and Saulnier-Z Soil Depth+ Vivoni Soil Texture (Z+V).

Surface runoff was observed during mid-July when precipitation events exceeded an intensity of 10 mm/h. Antecedent soil moisture conditions in early August was a product of continuous precipitation events, which lead to peak discharge within this month followed by a fast recession and lack of basin base flow in late August-early September (which it coincides with intra-seasonal drought). Low surface discharge was observed in September with the arrival of slight rainfall events.

3.3.3 Differences in Water Fluxes and States among Simulations

Seventeen out of a total number of twenty-two simulations are shown in this section. The simulations with the most contrasting results were included in this analysis. Two cases with uniform soil texture (UB+S and UB+ISa) and three with shallower-uniform soil thickness (U+V,U+A and U+I) were excluded due to similarity to other simulations.

Figure 3.5 shows the differences in water fluxes and states among all hydrological simulations. Figure 3.5a shows the basin-averaged (averaged in space within the boundaries of Sierra Los Locos basin) evapotranspiration accumulated during the monsoon season. Figure 3.5b shows the cumulative basin-averaged surface flow expressed as the sum of infiltration and saturation excess runoff flow. Figure 3.5c shows the cumulative subsurface flow, expressed as the sum of perched return flow and groundwater exfiltration flow. Figure 3.5d shows the cumulative infiltrated surface soil moisture (ignoring soil moisture losses) whereas Figure 3.5e explores the temporal evolution of cumulative infiltrated root zone soil moisture.

It is evident that subsurface flow, expressed in this research as the combination of perched return and groundwater exfiltration flows, which dominated the partition of the basin runoff throughout the simulation, but it was remarkably higher on those simulations that had abrupt changes in bedrock depth. For instance, soil thickness estimated by the Heimsath and Gessler methods, regardless the soil texture source had an impact in the generation of groundwater flow with cumulative seasonal values ranging from 40 to 148 mm. In all simulations, cumulative basin groundwater flows were similar at the beginning of the monsoon season until deviations occurred in August where the impact of groundwater to run off partition was evident. Furthermore, these methods showed a reasonable effect in surface flow (infiltration excess + saturation excess). Once again, soil thickness calculated by Heimsath and Gessler had a significant effect in the seasonal cumulative surface flow. Conversely, the hydrological simulations that used Saulnier-z soil thickness with INEGI soil data (Z+I) and the uniform 1.5 soil thickness with INEGI soil data (UB+I) were similar to the Benchmark case (solid bold black line).

A more detailed evaluation of the performance of hydrological simulations in comparison with the model benchmark will be mentioned later. On the other hand, basin averaged-ET was affected more directly by soil texture than soil thickness. Hydrological simulations assuming uniform soil texture, established the upper and lower boundaries in seasonal cumulative ET (figure 17a) and the rest of the simulation fluctuated between these two limits. Uniform sandy clay loam texture on Sierra Los Locos basin set up the upper limit in seasonal cumulative ET fluxes while uniform sandy loam texture showed the lower ET fluxes. It is well known that soil texture highly influences water retention and infiltration in soils; as a matter of fact, previous studies in arid and semiarid areas have demonstrated that clay-rich soils have more water availability in the surface, which may enhance evaporation from the soil, and transpiration for shallow rooted plants (Noy-Meir, 1973; Sala et al., 1988; Rodriguez-Iturbe et al., 1999). Conversely, sandy-rich soils can rapidly infiltrate water to deeper soil layers and could not be available for soil evaporation or transpiration of plants (English et al., 2005). In a like manner, estimated soil thickness with high spatial variability increased the rates of cumulative seasonal evapotranspiration. For instance, estimated soil thickness by the Heimsath and Gessler method obtained higher seasonal ET fluxes than the benchmark simulation. However, the differences between Heimsath-Gessler simulations and the benchmark were higher when the soil texture data of Vivoni et al. (2010) was used and decreased with the other soil texture sources. In contrast, the hydrological simulations similar to the model benchmark included Saulnier-z method with ASTER soil texture (Z+A), Saulnier-z with Vivoni soil texture (Z+V) and the Saulnier-slope soil thickness with ASTER soil texture (S+A). Later, these simulations did not show extreme soil thickness gradients and its spatial variability was much smoother compared to the Heimsath and Gessler methods.

Seasonal cumulative surface and root zone soil moisture had a similar temporal distribution compared to evapotranspiration. Likewise, soil texture established the lower and upper limits of the basin-average soil moisture with uniform sandy clay loam simulation resulted in the highest soil moisture values, whereas uniform sandy loam texture yield the lowest soil moisture values. This suggested that soil moisture exerted a strong control in basin-average evapotranspiration. High variability soil thickness tended to accumulate more soil moisture than smoother soil thickness variability. Similar modeling studies have found that spatially-variable soil depth and bedrock topography play an important role in subsurface hydrology, for example; Lanni et al. (2013) have found that soil bedrock interface, in particular bedrock depressions, played a key role in the sustaining of wetter soil conditions acting as an impedance for downslope drainage and developing a temporary perched water table. If basin connectivity exists, then subsurface flow can increase and dominate runoff flow (Tromp-Van Meerveld and McDonnell, 2006). Therefore the spatial and temporal variations of the spilling and filling of bedrock gaps are essential to the soil-bedrock interface. Lately, the effect of gaps in subsurface have received more attention in hillslope hydrology (Weiler et al., 2006).

3.3.4 Effect of Spatial Distribution of Soil Thickness on Water Fluxes and States: Constant Mean Soil Thickness but Different Spatial Distribution

In this section, we have evaluated the effect of having a mean soil thickness of 1.5 meters in all methods on water fluxes. In this set of hydrological simulations, we attempted to eliminate the possible effect of shallower or deeper soil moisture in the increase of surface soil moisture leading to high fluxes of ET. All soil thickness methods (Heimsath, Salnier-z, Salnier-slope and Gessler) had the same mean soil thickness (1.5 meters) but the spatial distribution id completely different among methods (figure 3.2). The depth value of 1.5 meters was selected in order to have a similar depth to the one used in the benchmark simulation. It is important to remark we kept the meteorological forcing, soil parameters and vegetation parameters unchanged for all simulations; only the spatial distribution of soil thickness was changed. Similarly to the other cases, the total hours of simulation was 3672 hours during the monsoon season 2004 (June 1 to September 30).

In order to evaluate the statistical difference with the model benchmark, we performed a t-test to paired datasets, in this case model benchmark to any other soil thickness method. Table 3.4 shows the results of the t-test using the value of the probability (p). This latter variable is the probability of observing a test statistic as extreme as, or more extreme than, the observed value under the null hypothesis. Small values of p cast doubt on the validity of the null hypothesis.
We found statistical significance in basin evapotranspiration (ET) in all methods with the exception of Saulnier_slp. Figure 3.5a confirms this statement because the cumulative seasonal ET obtained in the Saulnier_slope method closely tracks the benchmark simulation.

Soil thickness method	ET		SM		SM root zone		Runoff	
	p	p < 0.01	p	p < 0.01	p	p < 0.01	p	p < 0.01
Gessler	$7.07 e^{-7}$	****	0.19	-	$<7.07 e^{-23}$	****	$<7.07 e^{-23}$	****
Heimsath	$2.59 e^{-7}$	****	0.11	-	$<7.07 e^{-23}$	****	$<7.07 e^{-23}$	****
Saulnier_slope	0.41	-	0.08	-	0.0019	****	$<7.07 e^{-23}$	****
Saulnier_z	0.01	**	0.66	-	$7.07 e^{-23}$	****	0.254	-

Table 3.4. Results of T-Test Statistical Analysis for the Hydrological Simulations With Variation in Soil Thickness. In All Cases, Hydrological Simulations Were Compared to Benchmark Simulations. The P<0.01 Column Indicates the Statistical Significance, For Example; Highly Statistically Significant (****), Statistically Significant (**) and No Statistically Significant (-).

Curiously, none of the evaluated soil thickness methods showed statistical difference with the model benchmark when soil moisture is used as variable of evaluation. Conversely, root zone soil moisture was highly significant in all cases suggesting that subsurface topography has a role in the overestimation of total soil moisture in one-meter profile. Finally, Saulnier_z was not statistical different from the model benchmark on runoff. This statement is confirmed with figure 3.2b and c where surface and subsurface flow were very similar to model benchmark. However the rest of methods were highly significant. In summary, although we had similar mean soil thickness in Sierra Los Locos Basin, its spatial distribution highly affects the basin-averaged values of hydrological variables such as evapotranspiration, soil moisture and runoff.

3.3.5 Effect of Soil Thickness and Soil Texture in Basin-Averaged Water Fluxes and States

Soil thickness and soil texture was evaluated separately to evaluate the impact of these variables on the magnitude of basin-averaged evapotranspiration (ET) and soil moisture (SM). In order to isolate separately the effect of soil thickness and soil texture, we have separated two subsets of hydrological simulations. In both subsets, soil parameters, meteorological forcing and vegetation seasonality remained without changes.

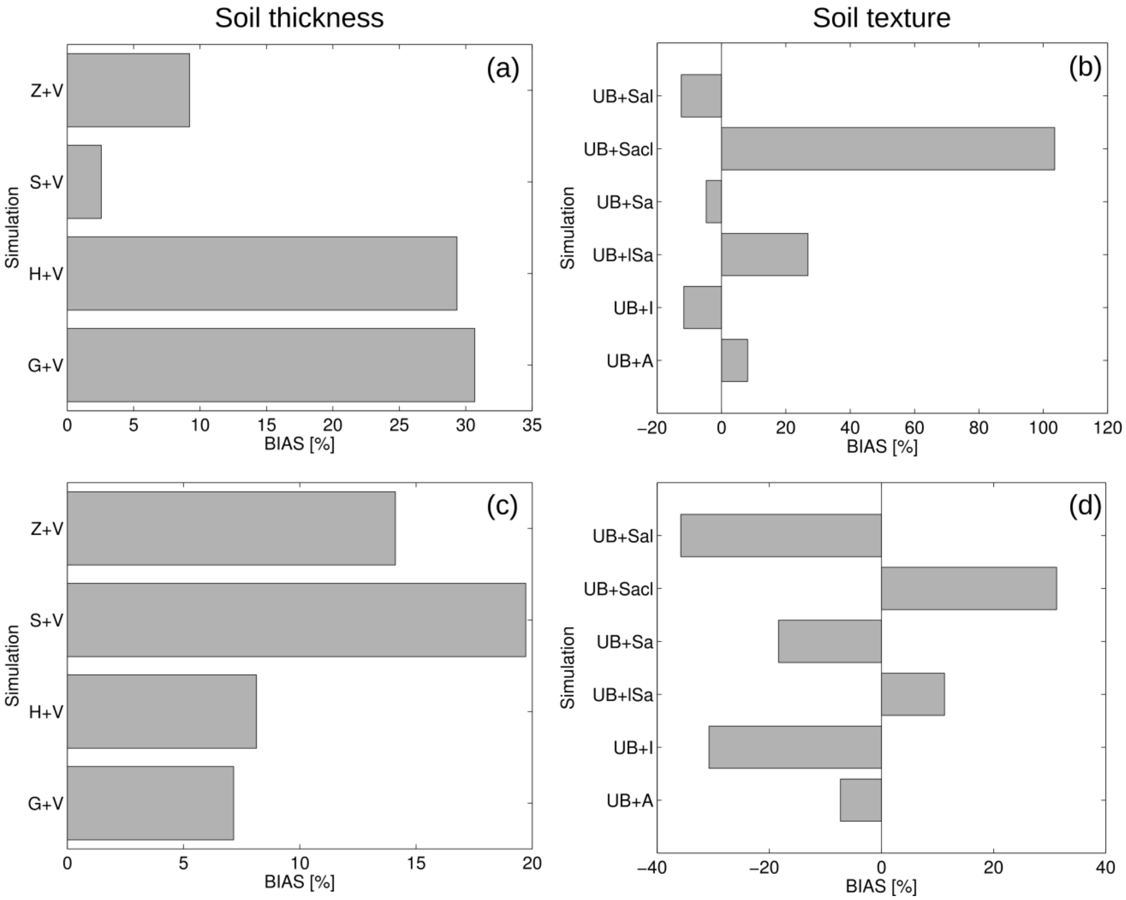

Figure 3.6. Effect of Soil Texture and Soil Thickness in Basin-Averaged Hydrological Variables. The Metric Used to Evaluate Model Performance Was Bias Expressed as Percentage of Under/Over Estimation to the Model Benchmark. (a) And (c) Show the Impact of Four Different Soil Thickness Distributions on Basin-Averaged Evapotranspiration (ET) and Surface Soil Moisture (SM) Respectively. (b) And (d) Illustrate the Effect of Six Different Soil Texture Depictions on Basin-Averaged ET and SM.

In one subset, soil thickness (Heimsath, Gessler, Saulnier-z and Saulnier-slp) was changed while in the other one soil texture was changed (ASTER, INEGI and four uniform soil texture cases). The results were compared to the benchmark simulation and the statistical metric used to evaluate simulation performance was bias (expressed as percentage of difference with benchmark). Figure 3.6 shows the rate of change in basin-averaged ET and soil moisture by running the benchmark simulation with different soil thickness data or soil texture. As observed, both soil moisture and ET were consistently overestimated regardless of the soil thickness data. Evapotranspiration was greatly affected by the Heimsath (H+V) and Gessler (G+V) methods. Both approaches overestimated seasonal cumulative evapotranspiration close to 30%.

Conversely, Saulnier-elevation (Z+V) overestimated seasonal ET in about 10% while Saulnier-slope (S+V) increased ET in about 3%. Unlike evapotranspiration, soil moisture did not follow the same magnitude of overestimation by soil thickness method, for example; the Saulnier-slope (S+V) method overestimated up to 20 % the seasonal soil moisture followed by Saulnier-elevation (Z+V) with in an overestimation of 14 % and both Heimsath and Gessler overestimated soil moisture close to 7%. It is clear that changing soil thickness produce wetter basins in comparison with benchmark simulation. However, there were one case (S+V) where ET was very close to model benchmark (~3% difference) but soil moisture was largely overestimated (20%). We can infer that although soil moisture is higher that model benchmark, this soil moisture is not accessible either to plants that can enhance evapotranspiration or low vegetation cover is present. In section 3.5 there will be a detailed description of how soil moisture is distributed in the Sierra Los Locos Basin

In contrast to soil thickness, soil texture showed larger differences in basin-averaged evapotranspiration and soil moisture in comparison with model benchmark. Figure 3.6b shows the effect of the spatial distribution of soil texture on basin evapotranspiration. As previously mentioned, there was a larger range of values in flux bias. For example uniform Sandy-loam, uniform sand and the INEGI soil texture map tended to underestimate ET in comparison with model benchmark. INEGI soil texture and uniform sandy loam underestimated ET in 10 %, while uniform sand overestimated only 5%. Conversely, seasonal ET was overestimated 10% when using ASTER-soil texture (UB+A); whereas uniform loamy sand over Sierra Los Locos Basin overestimated basin ET around 30% higher than benchmark simulation. Not surprisingly, uniform sandy-clay-loam overestimated the basin ET for more than 100%; and also, soil moisture in more than 35%. This latter soil texture showed the largest differences in basin averaged ET. One may infer that clay-rich soils have lower water infiltration than sandy-rich soils after rainfall pulses, allowing water to be available at the surface for plant transpiration or soil evaporation.

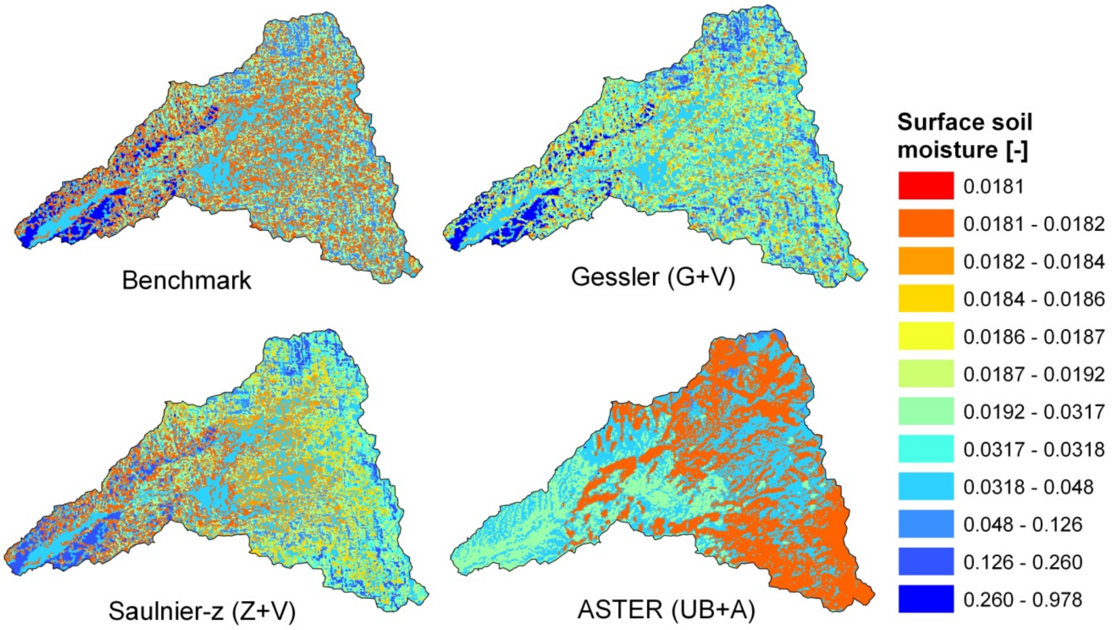
Benchmark

Gessler (G+V)

Saulnier-z (Z+V)

ASTER (UB+A)

Figure 3.7. Comparison of Four Different Spatial Representations of Time Integrated Surface Soil Moisture During the Monsoon Season 2004 (June Through September). The Model Scenarios Used for Comparison Were: Model Benchmark, Gessler Soil Thickness + Vivoni Soil Texture (G+V), Saulnier-Z Soil Thickness + Vivoni Soil Texture (Z+V), and Model Benchmark + ASTER Soil Texture (UB+A).

However, when vegetation is present, the surface loses water more quickly than bare soil because transpiration of plants (Huxman et al., 2004). Our results express the capacity of water retention related with soil texture and other studies have found similar patterns in soil moisture and vegetation with fine and coarse texture soils (Sala et al., 1988; Huxman et al., 2004). Finally, In the case of basin averaged soil moisture, uniform sandy loam, uniform sand, INEGI soil data and ASTER-based soil map showed an underestimation of 35, 20, 30 and 7 % with respect to the model benchmark respectively.

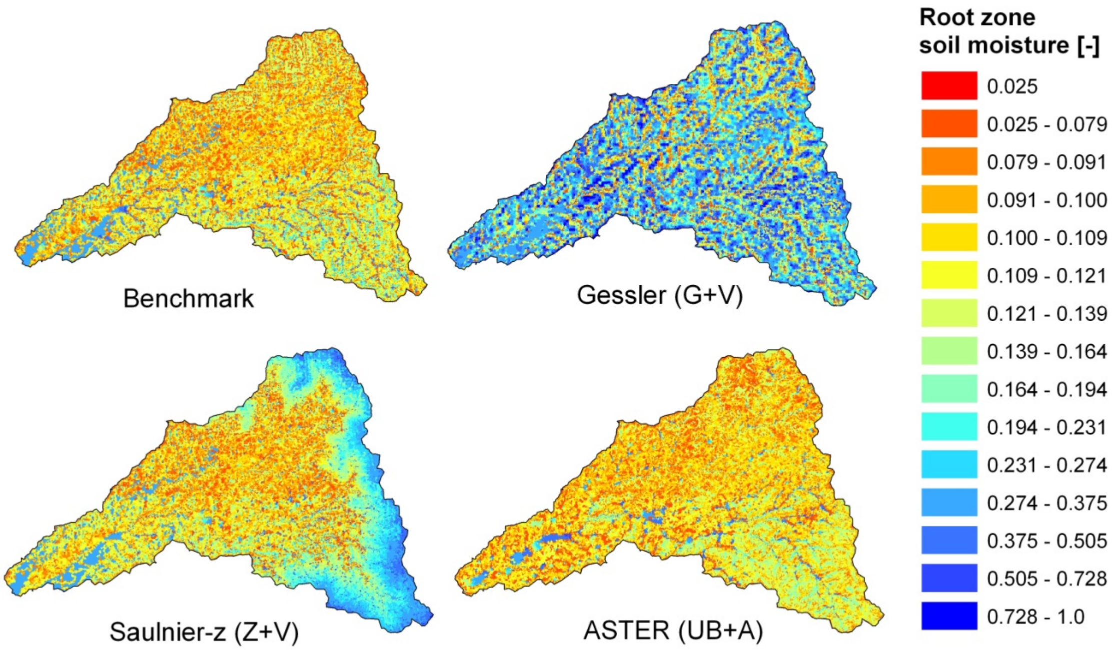

Figure 3.8. Comparison of Four Different Spatial Representations of Time Integrated Root Zone Soil Moisture During the Monsoon Season 2004 (June Through September). The Model Scenarios Used for Comparison Were: Model Benchmark, Gessler Soil Thickness + Vivoni Soil Texture (G+V), Saulnier-Z Soil Thickness + Vivoni Soil Texture (Z+V), and Model Benchmark + ASTER Soil Texture (UB+A).

3.3.6. Spatial Patterns of Surface Soil moisture, Root Zone Soil Moisture and Evapotranspiration in Sierra Los Locos Basin

In this section we have evaluated the role of soil thickness and texture on spatial patterns of soil moisture and ET at basin scale. Three different soil thickness distributions and two soil texture maps have been compared with model benchmark to evaluate changes in hydrological patterns at basin scale. The three maps of soil thickness evaluated in this section are characterized by contrasting distribution in soil thickness, for example; Gessler map is a shallow basin with a mean soil thickness of 80 cm with very complex subsurface topography. Secondly, Saulnier-z map has a deeper soil thickness with a smooth gradient in change of soil thickness that goes from shallower soil thickness in higher elevations and deeper soil thickness at lower elevation. Finally, Benchmark map has a uniform soil thickness of 1.5 meters. The two maps of soil texture (ASTER and slope-based) have contrasting soil texture distributions, therefore, selected to evaluate their role in the spatial distribution of water fluxes.

As observed in figure 3.7, model benchmark, Gessler and Saulnier-z cases showed similar spatial patterns in surface soil moisture. In fact, these model scenarios had a high spatial correlation coefficient with model Benchmark ($R^2 = 0.88$). Wetter soils were found in the main floodplain located in the western portion of the basin as well as some clusters in the gentle slopes located in the northern and eastern zones of the basin. The highest values in soil moisture (ranging from 0.260 to 0.90) found in model benchmark, Gessler and Saulnier matched with the spatial distribution of sandy clay loam (see figure 3.3b). This information suggested that the high capacity of water retention by clay-rich soils exerted a high control in wetness persistence. Furthermore, moderate soil moisture values (ranging from 0.0318 to 0.126) matches the spatial distribution of sandy loam textural soil type that suggest a moderate water retention capacity that affects the distribution of soil moisture. Finally, these three cases showed the lowest soil moisture values in loamy sand soils. Albeit the spatial patterns in soil moisture were similar in model benchmark, Gessler and Saulnier-z, the range in soil moisture values differs greatly among simulations. For example, Gessler simulation obtained the highest surface soil moisture values with those close to saturation soil moisture. Again this simulation reflects the role of sinks in subsurface topography in enhancing soil moisture values.

Conversely, the ASTER-soil texture map highly affected the spatial distribution of soil moisture and differs from the patterns observed in Vivoni et al. (2010) soil texture map. The almost non-existent clay rich-soils on this map reflected the lack of large spatial coverage of extreme high values in soil moisture. However, there was a clear gradient in soil moisture values that matches with the spatial distribution of soil type; for example, the lowest soil moisture values (ranging from 0.0181 to 0.0184) coincided with the distribution of loamy sand soils (figure 3.3c). Similarly, moderate soil moisture values (ranging from 0.0192 to 0.0318) matched with the spatial distribution of sandy soils; whereas the highest values (0.0318 to 0.126) were located on sandy loam soils.

In contrast, root zone soil moisture was affected in lesser degree by spatial distribution of soil texture but in certain cases was largely affected by soil thickness distribution. For instance, model benchmark showed slight differences in root zone soil moisture. There was a clear gradient in root zone soil moisture values with drier soil moisture values in the northern part of Sierra Los Locos basin while the south part is moderately wetter. In the same way that surface soil moisture, the west part of the basin observed the highest values of soil moisture. Likewise, floodplains and the spatial distribution of clay-rich soils (sandy clay loam) exerted a strong control on the spatial distribution of root zone soil moisture. The moderately increase in root zone soil moisture in the southern part of the basin could have been attributed to topographic controls such orographic effect on the distribution of rainfall. The southern region of Sierra Los Locos basin had the highest elevation with a pronounced relief. It is well known that precipitation-vegetation in the region was closely linked to the elevation distribution (Méndez-Barroso et al., 2009; Forzieri, et al., 2011).

Conversely, Sierra Los Locos basin showed wetter conditions when spatially variable soil thickness was used. For instance, there were extreme values of soil moisture (ranging from 0.505 to 0,728) when the Gessler soil thickness was used during hydrological simulations. These high values zones are represented as localized clusters (sinks) of high soil moisture values and are found in regions of high gradient in soil depth (soil pits upstream followed by shallow soil depth downstream). The dominant mechanism that increased the root zone soil depth was the filling and spilling of such subsurface bedrock pits that produced perched groundwater flux and increased soil moisture values when such soil pits were followed by shallow soil thickness. In fact, this phenomenon is widely accepted as the main mechanism of moisture dynamics in hillslope Hydrology. More authors found similar results when spatially variable soil depth was used to estimate hydrologic responses in virtual experiments (Weiler et al., 2004; Spence, 2010; Lanni et al., 2013).

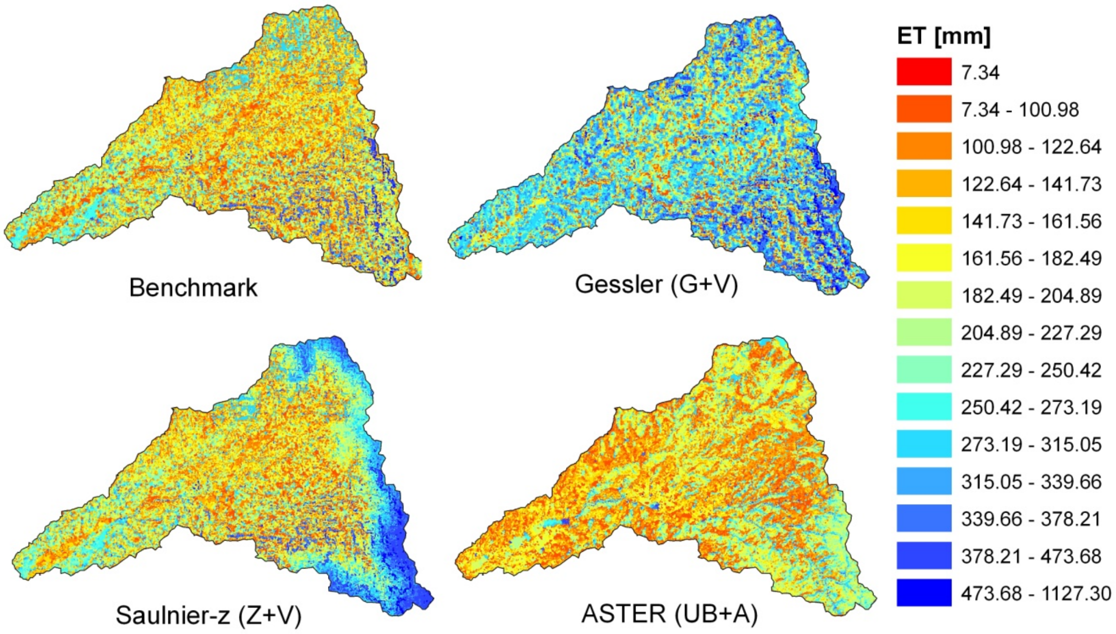

Figure 3.9. Comparison of Four Different Spatial Representations of Time Integrated Evapotranspiration During The Monsoon Season 2004 (June Through September). The Model Scenarios Used for Comparison Were: Model Benchmark, Gessler Soil Thickness + Vivoni Soil Texture (G+V), Saulnier-Z Soil Thickness + Vivoni Soil Texture (Z+V), And Model Benchmark + ASTER Soil Texture (UB+A).

When the Saulnier-z approach was used in hydrological modeling, a less complex and smoothly distribution was observed in simulated root zone soil moisture. High root zone soil moisture matched the distribution of shallow soil thickness while the rest of the basin showed a similar distribution to the model benchmark. Finally, estimates in distribution of root zone soil moisture with ASTER-soil texture map did not show large differences in spatial distribution of soil moisture compared to model benchmark. However, main discrepancies between ASTER-soil texture and model benchmark were found in the floodplain (west region of the basin). The high soil moisture values did not extend as wide as model benchmark. Unlike the model benchmark, the ASTER-soil texture map did not illustrate a large spatial extension of clay-rich soils in the flood plain that led to a low water retention capacity.

Unlike soil moisture, evapotranspiration highly depends on the spatial distribution of vegetation cover and the root zone soil moisture, as well as, but in a lesser degree; to the spatial distribution of soil texture. Although the magnitude of evapotranspiration varies among model scenarios, their highest seasonal integrated evapotranspiration values were found in mountain forests (for spatial distribution of ecosystems reader should reference Xiang et al., 2014). Model benchmark and Saulnier-z soil thickness experienced similar spatial distribution of seasonal ET with a great exception of the mountains regions. Saulnier-z showed high values in ET ranging from 378 to 473 mm with clusters reaching up to more than 600 mm. Such high values in ET could be attributed to the high availability of root zone soil moisture to the vegetation found at high elevations. Estimated ET with Gessler soil thickness was closely related to the spatial distribution of the root zone soil moisture. In general, ET was uniformly high in Sierra Los Locos using Gessler's soil thickness with lower values found in sandy soils. Sand-rich soils facilitated water infiltration leading water to deeper soil layers, which are not easily accessible to surface rooted plants, hence decreasing ET rates.

3.3.7 Impact of Vegetation Greening in the Spatial Variability of Basin ET and Soil Moisture

This section explores how the spatial variability of evapotranspiration and soil moisture behaved within the Sierra Los Locos during the evolution of the monsoon season 2004 (June to September). To evaluate this, the mean and standard deviation within the Sierra Los Locos basin was estimated each week in order to find out the evolution of the variability during the monsoon season. Figure 3.9 shows the evolution in the spatial variability of estimated soil moisture within Sierra Los Locos basin by applying five representative model simulations. The time series of basin-averaged Normalized Difference Vegetation Index (NDVI) was included in the figure to illustrate the conditions of vegetation growth in the basin. As observed, basin variability in soil moisture was in phase with the curve of vegetation growth. During dry conditions at the end of June through early July variability was low. Nevertheless, the largest variability consistently reached during the transition from dry to wet conditions, before vegetation achieved its maximum activity.

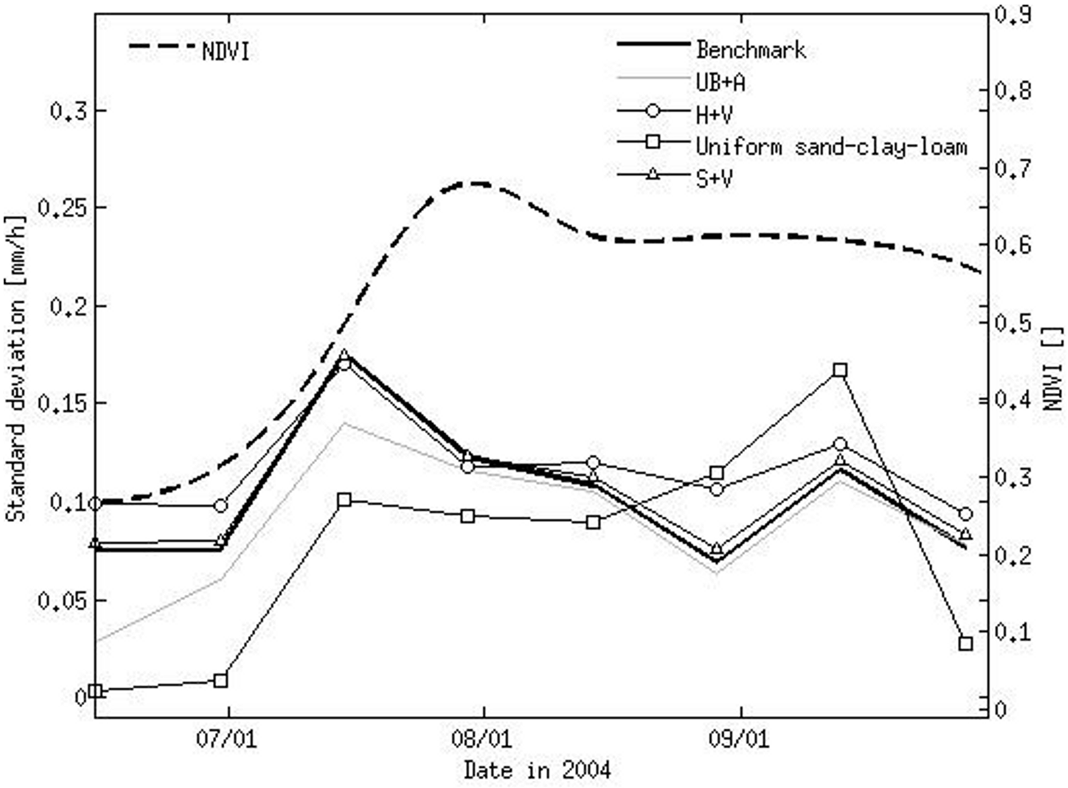

Figure 3.10 Comparison of Four Different Spatial Representations of Time Integrated Evapotranspiration During The Monsoon Season 2004 (June Through September). The Model Scenarios Used For Comparison Were: Model Benchmark, Gessler Soil Thickness + Vivoni Soil Texture (G+V), Saulnier-Z Soil Thickness + Vivoni Soil Texture (Z+V), and Model Benchmark + ASTER Soil Texture (UB+A).

Once basin vegetation was at its maximum point of seasonal greenness, soil moisture variability began to decrease or remained stable until the end of the monsoon season (late September). However, there were differences in the magnitude and rate of change in the spatial variability of soil moisture. For instance, model benchmark, Saulnier-slope and Heimsath soil thickness (using Vivoni soil texture) showed similar and stable spatial variability within the Sierra Los Locos Basin during dry conditions as well as the transition period (σ = 0.05 and 0.13 respectively).

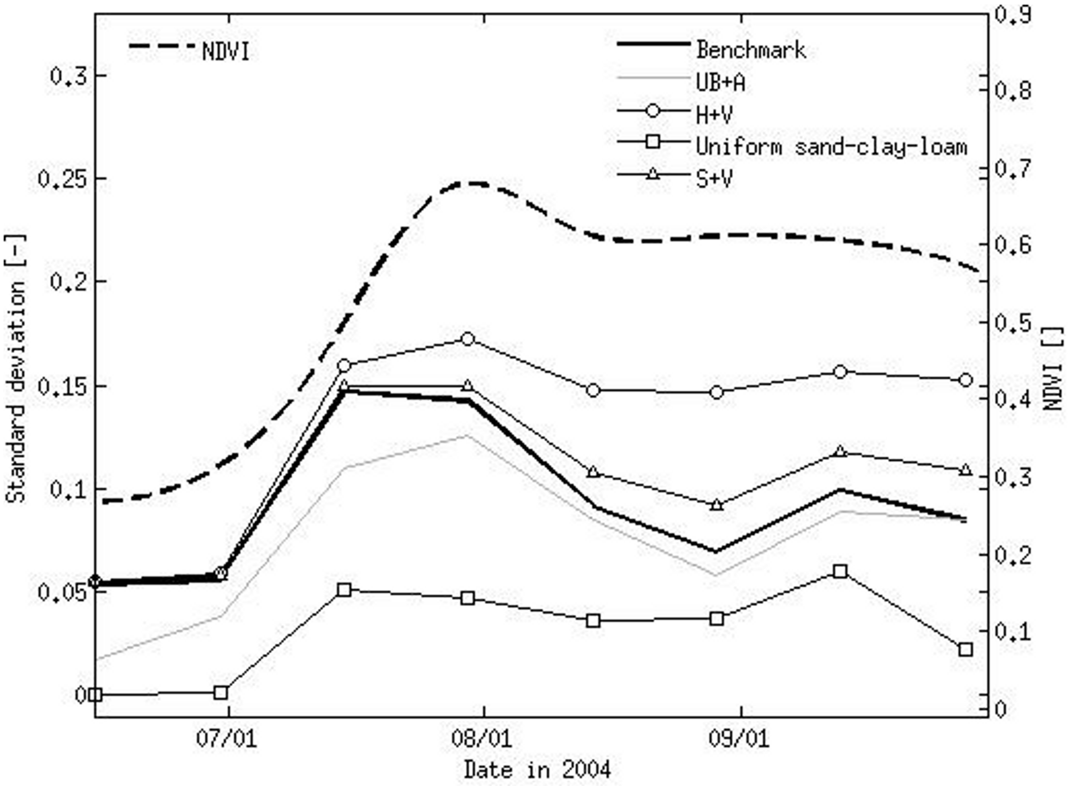

Figure 3.11. Temporal Evolution of Standard Deviation of Soil Moisture Under Five Model Scenarios. Dashed Black Line Shows the Time Series of Vegetation Greenness (NDVI) During the Monsoon Season 2004. The Model Scenarios Evaluated Were: Benchmark (Black Solid Line), Model Benchmark + ASTER Soil Texture (Grey Line), Heimsath Soil Thickness + Vivoni Soil Texture (Open Dots), Uniform Sandy Clay Loam (Squares) and Saulnier-Slope Soil Thickness + Vivoni Soil Texture (Triangles).

When vegetation is well established, the spatial variability of estimates soil moisture among these later simulations started to deviate in different ways. Heimsath hydrological simulations continued to be stable after reaching the maximum point of variability in late July with a slight decrease in mid-August. Conversely, spatial variability of Saulnier –slope and model benchmark decreased with larger discrepancies between these two model simulations starting in late August to the end of the monsoon season. In the case of the ASTER-soil texture simulation, the spatial variability of soil moisture was lower than the model benchmark along with the Heimsath and Saulnier- slope simulations (σ = 0.012 at the beginning of the monsoon season and maximum of 0.12 in early August). Uniform sandy clay-loam showed the lowest values of standard deviation and smallest temporal variability. Due to the fact that soil type did not vary in the basin, spatial variation was small. These minimal changes could be attributed to basin topography or patterns in vegetation. Similarly to the other cases, variability increases during the shift from dry to wet conditions or during the vegetation green up. Once vegetation vigor (high NDVI starting at mid-July) is high, variability stabilized, suggesting small spatial variability within the basin.

Evapotranspiration showed a similar temporal behavior in spatial variability within the Sierra Los Locos Basin. In general, all simulation cases showed the highest spatial variability during vegetation green up. Spatial variability remained stable during the dry period (June to early July). During vegetation green up, there was significant spatial variability inside the basin and it was expressed as high values of standard deviation. Model benchmark, Heimsath and Saulnier-slope had a similar temporal evolution since the beginning of monsoon season until early August. In mid-August, Heimsath deviated from model benchmark and Saulnier-slope. These two latter cases continued with similar temporal evolution in basin variability through the end of the season. The model simulation with ASTER-soil texture started with small basin spatial variability at the beginning of the monsoon season but when vegetation greenness reached its maximum point behaved similar to model benchmark, Heimsath and Saulnier-slope simulations. Finally, the uniform sand-clay loam simulation had a different evolution in spatial variability in comparison with the rest of the cases. This latter case started with stable spatial conditions at the beginning of the monsoon season. When growing season progressed the spatial variability increased steadily until mid-September, when a sudden decrease of the spatial variability occurred leading to stable conditions.

3.4 Summary and Conclusions

This research ran a set of hydrological simulations in a semiarid basin within the North American Monsoon region. Some of these simulations accounted for the spatial distribution of soil depth and soil texture with the goal to evaluate their effect on energy and water fluxes. The results of these simulations were compared to a previous calibrated hydrological simulation, which was described in this research as model benchmark and is described in Xiang et al., (2014). After performing a series of analyses the research concluded:

Surface soil texture exerted a strong control in surface soil moisture (5 cm depth). Wetter regions within Sierra Los Locos basin were closely linked to textural classes with large water retention capacities such as clay-rich or sandy-loamy soils. Drier soils are closely linked to high infiltration capacities soils, similar to sandy soils with scarce vegetation.

Root zone soil moisture was strongly controlled by spatial variability of soil thickness by creating soil depressions that retained subsurface water. The filling and spilling of these soil depressions greatly affected groundwater exfiltration, especially; when soil depressions were followed by shallow soil thickness. Semiarid basin groundwater table was usually disconnected from the river network and the main mechanism of run off generation was infiltration excess (Hughes, 1995; Pilgrim et al., 1988). In this case, it is essential to establish a fixed groundwater table or the Saulnier-z or Saulnier-slope when is necessary to account for spatial variation in soil thickness. However, there could be regions or events during the monsoon season when the water table could be connected to the river network. In this case, an alternative is to use a more realistic and accurate spatial distributed soil thickness similar to Heimsath or Gessler.

Heimsath and Gessler are reliable alternatives to estimate distributed soil thickness particularly in basins with limited information and surveying may be labor intensive and expensive. Soil texture surveying using remotely sensed data was also another reliable alternative for remote basin with lack of soil information.

The visible and thermal bands of the Advance Spaceborne Thermal Emission and Reflection Radiometer (ASTER) have demonstrated to be a reliable option for soil texture surveying.

Soil texture exerted a strong control in spatial patterns of soil moisture and evapotranspiration during the transition from dry to wet conditions. Once vegetation vigor and cover fraction are dominating the basin, the influence of soil texture in controlling spatial patterns decreased and vegetation tended to smooth this spatial variability within the basin.

Finally, this work displayed a significant improvement in the representation of basin characteristics. This can help future research to understand and improve water balance forecasting and spatial patterns of hydrological variables.

CHAPTER 4

INTER-ANNUAL VARIABILITY OF VEGETATION COVER AND ITS EFFECT ON THE SPATIAL AND TEMPORAL DISTRIBUTION OF EVAPOTRANSPIRATION AND RUN OFF IN A SEMIARID BASIN

4.1 Introduction

It is well known that water controls vegetation growth in arid and semiarid areas in the world. Furthermore, vegetation exerts a feedback mechanism by returning water to the atmosphere and controlling surface processes such as run off generation, albedo and land surface temperature (Eltahir, 1998; Dominguez et al., 2008). One of the regions that experience large shift in vegetation greening is the west slopes of the Sierra Madre due to the onset of the North American Monsoon (NAM) region (Forzieri, et al., 2011; Watts et al., 2006). Recently, the amount of run off and ET studies in the NAM have been increasing despite the lack of hydrological observations. For example, previous studies have shown the regional variation in the relation between rainfall-runoff and its dependence with monsoon rains (Brito-Castillo et al., 2003; Gochis et al., 2006;). Other studies have evaluated the impact of land use or land cover change on surface run off and soil removal (Navar and Synnott, 2000; Viramontes and Descroix, 2003) in field plots. Moreover, the use of hydrological models has been recently increasing to understand hydrological processes and water balance in ungauged basins in the NAM region (Vivoni et al 2010; Gochis et al., 2010; Vivoni, 2012, Robles-Morúa et al., 2012; Mendez-Barroso et al., 2014; Robles-Morúa et al., 2014). Main contribution in this area comprises the impact of the surface and subsurface features on water and energy fluxes, e.g.; surface water states such as antecedent soil moisture and water content decay parameter play an important role in the generation of run-off and catchment hydrological behavior in subtropical ecosystems of Northern Mexico (Descroix et al., 2002).

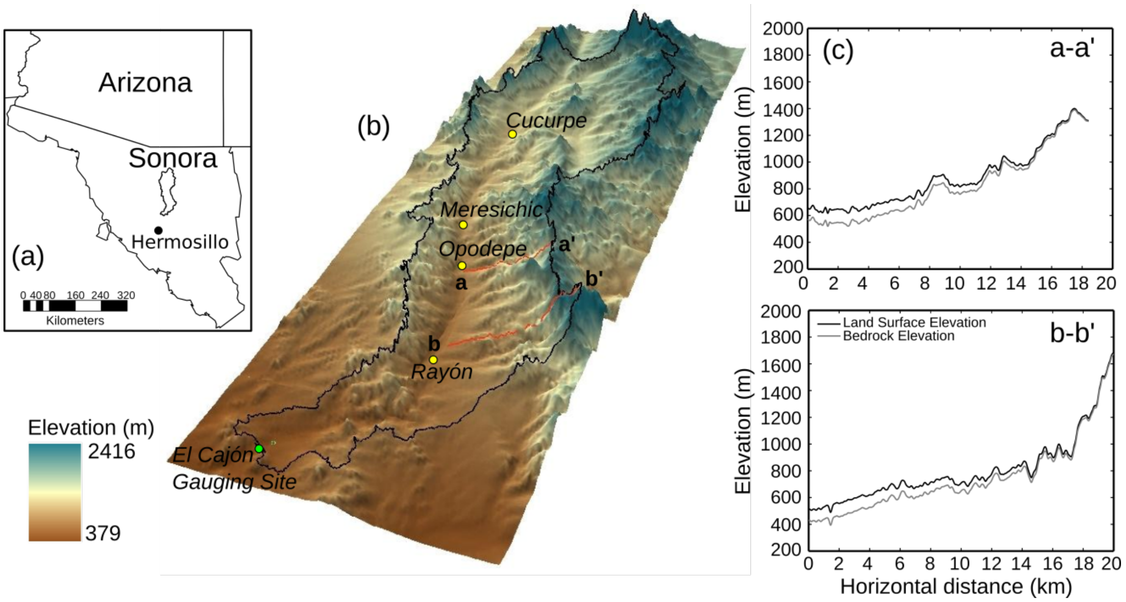

Figure 4.1. Land Morphology and Basin Location. (a) Location of the San Miguel River Basin in a Regional Domain. (b) Topographic Characteristics of the San Miguel Basin With the Location of El Cajón Gauging Site and Some Important Towns. (c) Land Surface and Bedrock Elevation Profiles on Transects A-A' And B-B'. Basin Relief is About 2000 Meters.

4.2. Methods

4.2.1 Study Region

The San Miguel river basin (SMRB) is located in the Northwestern Mexican state of Sonora. This basin has an area of 3796 km^2 (figure 4.1) and it is the second largest within the Sonora River System. The topography is quite complex with an elevation relief close to 2000 meters and slopes ranging from 0 to 65 degrees. The central part of the state belongs to the southern extreme of the Basin and range, a physiographic region characterized of valleys bounded by one or more normal faults that runs parallel to range front (Dickinson, 2002). Normal faults usually trend North-South in the same direction of the mountain range. Basin headwaters are located in the Sierra Azul mountain range with river tributaries flowing along the east-west and west-east directions into the main river. The main river flows from north to south until it reaches the only stream gauge that monitors and records basin discharge at El Cajon gauge station, near San Miguel de Horcasitas, Sonora, Mexico.

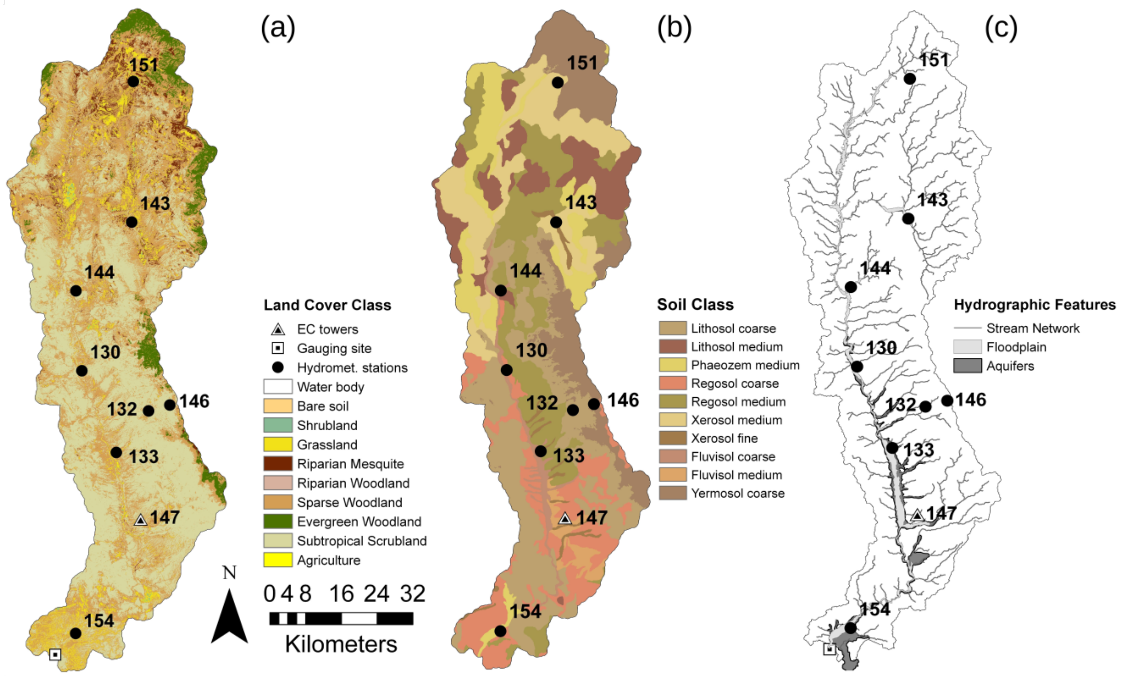

Figure 4.2. San Miguel River Basin Characteristics. (a) Land Cover Estimated From Landsat 5 Using A Decision Tree Method (Yilmaz et al., 2008). (b) Soil Classes Obtained from INEGI (National Institute of Geography And Statistics) Following the FAO Soil Classification System. (c) Stream Network Derived from ASTER Digital Elevation Model Using the Terrain Analysis Model Taudem (Terrain Analysis Using Digital Elevation Model).

Ecosystems in the San Miguel River Basin follow a very well defined rainfall (in this region rainfall is closely related to elevation) pattern that identifies vegetation characteristics (Figure 4.1b). This pattern ranges from desert scrubs (at lowest elevation ~ 300 to 400 m) to evergreen communities (mixed forest) in higher elevations (beyond 1300 m). The dominant ecosystem in the basin is subtropical scrublands, which encompass 44% of the total area, followed by sparse woodlands (sparse woodland with 37%) and grasslands (8%). Different soil types exist in the basin where the most common are Lithosol, Regosol and Xerosol that respectively include 43%, 28% and 15% (total of 84%) of the basin area (Table 4.1). Lithosols are soils with shallow thickness with lack of horizons development and are found in mountains regions with high steepness.

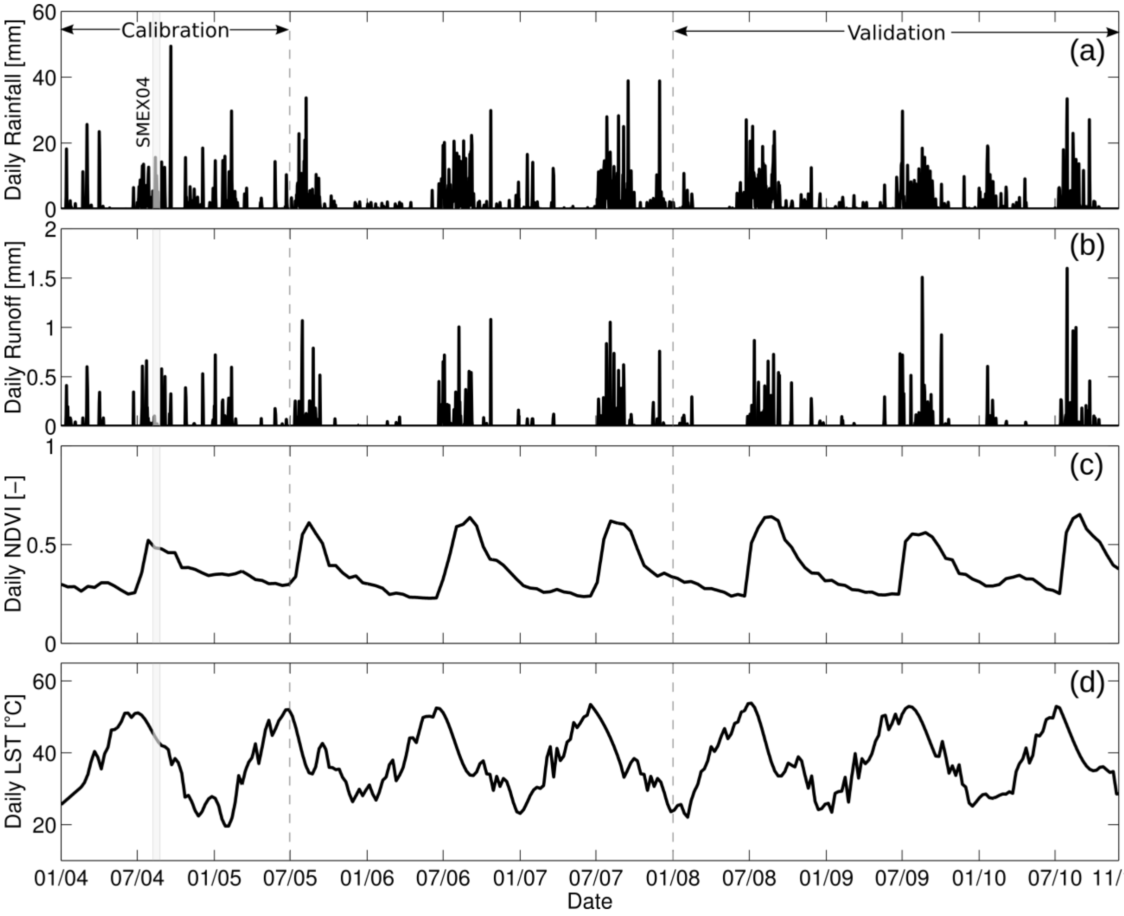

Figure 4.3. Seasonal Variability of Rainfall, Runoff and Normalized Difference Vegetation Index (NDVI) on the San Miguel River Basin Encompassing the Period 2004-2010. (a) Daily Rainfall Aggregated from a Network of Meteorological Stations Managed by The Mexican National Water Commission (CONAGUA). (b) Daily Runoff Measured at the CONAGUA Gauging Site El Cajon. (c) Daily Interpolated Land Surface Temperature (LST) from the Moderated Resolution Imaging Spectroradiometer (MODIS). Gray Vertical Bars in August 2004 indicate the Days of Acquisition of Soil Moisture Maps by the 2DSTAR Aircraft-Based Sensor.

Secondly, Regosols are very weakly developed mineral soil in unconsolidated material and are very common in arid or semiarid areas and mountain regions of the world. Finally, Xerosols appear in arid areas and can contain organic matter and deeper layers with accumulation of clays, carbonates and sulfates. Other minor soil types in the region are Phaeozem, Yermosol and Fluvisol.

Land cover type	% Area
Water body	0.001
Bare soil	0.03
Shrubland	0.22
Grassland	8.03
Riparian Mesquite	4.44
Riparian Woodland	0.09
Sparse woodland	37.80
Evergreen	4.56
Subtropical scrub	44.78
Agriculture	0.05
Soil Type	**% Area**
Phaeozem	9.09
Fluvisol	3.46
LIthosol	43.01
Regosol	27.54
Xerosol	14.94
Yermosol	1.96

Table 4.1. Percentage of Area Covered by Different Land Cover and Soil Types Within the San Miguel River Basin (SMRB).

The precipitation regime in this region is characterized by a marked seasonality, with most of the annual precipitation (60-70% of the total) falling during summer months (June, July and August) during the onset of the North American Monsoon (NAM) (Douglas et al., 1993; Adams and Comrie; 1997). Figure 4.3a shows the time series of the mean areal precipitation during the study period from January 2004 to November 2010. As observed, most of the rainfall events occurred during the monsoon season mainly in the form of convective storms localized in space and time, while some sporadic rainfall events occurred in winter in the form of stratiform systems with larger spatial coverage (Mascaro et al., 2014). A notable exception occurred in the winter of 2004 when intense storms, caused by El Niño (Brito-Castillo, 2003), produced abnormal discharge in the basin (Figure 4.3b). Vegetation seasonality in the San Miguel River Basin is highly coupled to inter-annual variability in seasonal precipitation. For example, Figure 4.3c shows contrasting years in seasonal precipitation where the summer season in 2004 was a dry monsoon season while the summer 2008 was a wet year. These contrasting conditions in seasonal precipitation led to similar contrasting conditions in vegetation greening in the region.

4.2.2 Field and Remote Sensing Observations

For this study we used rainfall and soil moisture observations at different locations within the San Miguel River Basin domain . Every station consists of a tipping bucket gauge (Texas electronics, TR525W) and two soil moisture probes (Stevens Water Monitor Systems, Hydra Probes) deployed at 5 and 10 centimeters depth. Soil moisture and rainfall data were stored every 30 minutes in a Campbell data logger model CR1000. We used 9 hydro-meteorological stations distributed along the San Miguel River Basin, which some have been operating since July 2004 and were installed as part of the Soil Moisture Experiment in 2004 (SMEX04). Table 4.2 shows the locations of 9 hydro-meteorological stations in the Rio River Basin, as well as some site characteristics such as soil type, elevation land cover and the purpose of the station data set (either calibration or validation).

In addition to ground observations, we utilized remote sensing imagery of the land surface to monitor vegetation development, surface energy states and surface topography. Normalized Difference Vegetation Index (NDVI), Leaf Area Index (LAI), short wave white-sky albedo and Land Surface Temperature (LST) from The MODerate resolution Imaging Spectroradiometer (MODIS) were used to characterize the spatial variability of the land surface conditions, and generate dynamic vegetation fields required to parameterize plant phenology in the hydrological model as described in Méndez-Barroso (2014). We utilized 16-day composites of NDVI (MOD13Q1, with spatial resolution of 250 meters) along with 8-day composite of white sky-albedo (MOD43B, spatial resolution 1000 meters), LAI (MOD15A2, spatial resolution 1000 meters) and LST (MOD11A2, spatial resolution 1000 meters) comprising an image catalog of 7 years (2004 through 2010). Our MODIS dataset was projected, transformed and clipped using the HDF-EOS to GeoTIFF conversion tool (HEGtool). This tool allows converting the MODIS native hierarchical data format (hdf) to the widely used GIS-format GeoTIFF. Furthermore, HEGtool allows clipping MODIS imagery to a smaller region of interest in batch form. MODIS 16 and 8-day composites of LST, NDVI and LAI were interpolated to daily images to capture the progression of land surface changes. For evaluation of model performance, we used MODIS LST as well as soil moisture observations at 800-m resolution from the Two-Dimensional Synthetic Aperture Radiometer (2DSTAR) aircraft-based sensor, which collected measurements on August 7-8 and 24-26, 2004 as part of SMEX04 (Ryu et al., 2010).

4.2.3 Basin, Floodplain and River Network Delineation

A realistic representation of basin characteristics is critical in order to have an accurate temporal and spatial distribution of water and energy fluxes. Basin topography is represented in the tRIBS hydrological model through a Triangular Irregular Network (TIN) (Ivanov et al., 2004a,b). The TIN for the RSMB was created from the 30-m resolution Digital Elevation Model (DEM) derived from ASTER (Advance Space-borne Thermal and Reflection Radiometer), according to the procedure described in Vivoni et al. (2005) and aimed at capturing the hydro-physiographic features of the basin by sampling the DEM with varying resolution. Specifically, given the importance of the processes occurring in the riparian area, a higher detail was adopted to represent the floodplain. Floodplain delineation was conducted by using thermal infrared spectral indices from ASTER that allowed us to separate different materials based on their spectral absorption. The indices used were carbonate Index (band13/band14), quartz Index ($band11^2$/band10*band12) and the mafic index (band12*$band14^3$/$band13^4$). These ASTER-based geological maps helped us to identify the extension of the current flood plain and later corroborate it with existing geological maps and aerial orthophotos in order to have a more accurate delineation of the river floodplain.

River network was delineated using the Terrain Analysis Using Digital Elevation Models (TauDEM version 5.0) adopting the slope-area relation method that allow to have a better representation of the stream network in wide and meandering floodplains (Tarboton, 2003).

Station	Lat. [°]	Long. [°]	Easting [m]	Northing [m]	Elevation [m]	Soil Type	Land cover	Cal. year	Val. year
130	30.0	-110.6	531465	3323298	708	R	Sps	2004	2007
132	29.9	-110.5	546347	3314298	878	L	Ss	2004	2007
133	29.8	-110.5	539130	3305014	624	F	Sps	2005	2007
143	30.3	-110.5	542590	3356533	947	F	Ss	2004	2007
144	30.2	-110.6	530134	3341169	778	F	Ss	2007	2007
146	29.9	-110.4	551091	3315638	1377	L	Ws	2004	2007
151	30.6	-110.5	542954	3387967	1419	X	Rm	2007	2007
154	29.5	-110.6	530064	3264545	419	P	Sw	2007	2007
ST-EC	29.7	-110.5	544811	3290182	632	Y	Ss	2004	2007

Table 4.2. Characteristics and Location of Hydro-Meteorological Stations Used for Model Calibration and Validation. Soil Types are: Regosols (R), Lithosols (L), Fluvisols (F), Xerosols (X), Yermosol (Y) and Phaeozem (P). Land Cover Types are: Sparse Woodland (Sps), Subtropical Scrubland (Ss), Woodland Savanna (Ws), Riparian Mesquite (Rm) and Sparse Woodland (Sw).

Both the river flood plain and river network was later incorporated in the creation of triangulated irregular network. The final representation of topography by triangulated irregular network was generated using the TINindex Analysis Package (TIAP, version 1.2). The total number of Voronoi polygons (unit for fluxes computations) for the San Miguel River Basin TIN was 618,745 resulting in a horizontal point density (the ratio of DEM cells to TIN nodes) was d = 0.147 with an equivalent cell size of r_e = 78.21 meters.

Spatially variable depth to bedrock was estimated according to the method proposed by Saulnier et al., (1997). This method correlates soil depth (*h*) as a linear function of local elevation (*z*):

$$h = h_{max} - \frac{z_i - z_{min}}{z_{max} - z_{min}} (h_{max} - h_{min}) \tag{4.1}$$

Where h_{max} is the maximum bedrock depth observed in the basin, h_{min} is the minimum bedrock depth observed, z_i is the current value of elevation whereas z_{max} and z_{min} are the maximum and minimum elevation values respectively.

4.2.4 Hydrological Forcing

We used ground-corrected meteorological grids form the North American Land Data Assimilation System, version 2 (NLDAS-2) to force our model simulations (Cosgrove, 2003). NLDAS hourly data was obtained from the NASA-GES Hydrology Data Holdings web site (http://disc.sci.gsfc.nasa.gov/hydrology/data-holdings). The native GRIdded Binary format (grib) was converted to ESRI ascii format, which is the format, required as an input for the hydrological model. The meteorological variables used to force the model consisted in grids with a spatial resolution of 12 km (0.125°) of atmospheric pressure (PA), relative humidity (RH), incoming short wave radiation (IS), air temperature (TA), wind speed (US) and precipitation (RA).

The NLDAS datasets were corrected with ground observation using the approach of Robles-Morúa et al. (2012) based on the application of an averaged ratio of means multiplicative factor of Steiner et al. (1999). We relied on a network of meteorological station managed by the Sonora State Water Commission (CEA for the acronym in Spanish) to adjust model meteorological forcing and rainfall. Due to the lack of ground observations during the year 2006 and part of 2007, we decided to use NLDAS-adjusted data for the year 2004 and 2005 for model calibration and year 2008 through 2010 for model validation.

4.2.5 Description of the Distributed Hydrological Model

Numerical hydrological simulations were carried out using the TIN-based (Triangular irregular network) Real-time Integrated Basin Simulator (tRIBS), a fully distributed model of hydrological fluxes (Ivanov et al., 2004, Vivoni, 2007). This model works in a framework represented by a network of TIN with embedded elevation, channel and boundary nodes that mimic the basin topographic features. TINs are linked to a series of Voronoi polygons that allow flux and mass calculations under the finite difference approach. Hydrological domain (San Miguel

River Basin) was delineated using a digital elevation model from ASTER with a spatial resolution of 30 meter draining to the only stream gauge located in the basin. The National Water Commission (CONAGUA for the acronym in Spanish) operates this stream gauge (known as “El Cajon”) and it is located near the town of San Miguel de Horcasitas.

Because the large amount of Voronoi polygons, The Saguaro supercomputer performed the hydrological simulations in parallel mode (distribution of tasks over multiple processors at once) at ASU-Advance Computer Center. Saguaro is a massively parallel cluster or a collection of many small computer nodes that are interconnected with high speed, low-latency network fabric. The reach-based partitioning method divided the domain of the San Miguel River Basin in 256 processors. A set of empirical equations described in Méndez-Barroso et al. (2014) calculated dynamic vegetation parameters that accounts for rainfall interception and plant transpiration. Such equations relate remotely sensed vegetation indices such as MODIS-Leaf Area Index (LAI) and Normalized Vegetation Index (NDVI) with vegetation variables such as Optical transmission (OT), canopy capacity (CC), stomatal resistance (SR), through-fall coefficient (TF) and vegetation fraction (VF). Furthermore, MODIS-short wave albedo (AL) was incorporated to account for the partition of energy balance in the surface.

Spatial distribution of soil types in grid format was acquired from the National Institute of Statistics and Geography (INEGI for its the acronym in Spanish) based on the soil classification system of the Food and Agriculture Organization (FAO). Soil hydraulic parameters were estimated from particle size distribution applying the pedotransfer functions described in Saxton et al., 2006. Soil texture was estimated by analysis of soil samples collected nearby the station sites. However, when soil samples were not available for analysis, we relied in soil texture fractions obtained from the Global Soil Profile Dataset (ISRIC-WISE, version 3.1) developed and updated by the International Soil Reference and Information Centre. The ISRIC-WISE database contains soil horizon information for about 149 countries using the FAO-UNESCO soil classification (Batjes, 2009). Furthermore, we utilized the land cover-land use classification developed by Yilmaz et al., 2008 using a decision tree parameterization over Landsat 5 TM imagery over the region.

Parameter	*Variable [unit]*	*Lithosol coarse*	*Lithosol medium*	*Phaeozem medium*	*Regosol coarse*	*Yermosol coarse*
Saturated hydraulic conductivity[1]	K_s [mm/h]	32.4	6	15	49.1	32.4
Saturated soil moisture content[1]	θ_s [-]	0.4	0.47	0.49	0.38	0.4
Residual soil moisture content[2]	θ_r[-]	0.01	0.01	0.01	0.002	0.01
Pore size distribution index[3]	m [-]	2	2	2	0.8	1.6
Air entry bubbling pressure[3]	ψ_b [mm]	0	0	0	0	0
Conductivity decay parameter[4]	f [mm^{-1}]	8x10^{-4}	8x10^{-4}	8x10^{-4}	3x10^{-4}	8x10^{-3}
Conductivity anisotropy ratio[4]	A_s [-]	1	1	1	1	1
Soil porosity[1]	n [-]	0.42	0.49	0.51	0.40	0.42

Parameter	*Variable [unit]*	*Regosol medium*	*Xerosol medium*	*Xerosol fine*	*Fluvisol coarse*	*Fluvisol medium*
Saturated hydraulic conductivity[1]	K_s [mm/h]	8.3	3.9	33.6	5	49.1
Saturated soil moisture content[1]	θ_s [-]	0.47	0.47	0.4	0.51	0.38
Residual soil moisture content[2]	θ_r[-]	0.002	0.01	0.03	0.05	0.002
Pore size distribution index[3]	m [-]	2	2	0.06	2	1.5
Air entry bubbling pressure[3]	ψ_b [mm]	0	0	0	0	0
Conductivity decay parameter[4]	f [mm^{-1}]	3x10^{-4}	3x10^{-4}	0.05	0.0009	0.0009
Conductivity anisotropy ratio[4]	A_s [-]	1	1	1	1	1
Soil porosity[1]	n [-]	0.49	0.49	0.42	0.53	0.40

Table 4.3. Model Parameters for Different Soil Types in Rio San Miguel River Basin. Source of Model Parameters are as Follows: (1) Based on ISRIC-WISE World Soils Database With Modifications During Calibration. (2) Minimum Observed Soil Moisture. (3) Méndez-Barroso et al., 2014 and Xian et al., 2014 (4 and 5) Model Calibration.

However; this land cover map did not cover the southern part of the basin. For this reason, we performed a non-supervised classification (Maximum Likelihood Classification) using all the bands of a previous Landsat image over the region and complement the land cover of Yilmaz et al., 2008.

Dynamic groundwater equilibrium was reached by performing a spin-up process to our hydrological simulation. We did not find inter-annual statistically significant differences in discharge and soil moisture during the three years of spin-up. Consequently, the spin up process lasted only 1 year.

4.2.6 Model Initialization, Calibration and Validation

Because the limitation of continuous soil moisture and temperature observations in the hydro-meteorological network, we restricted the model calibration to the monsoon seasons (June 1 through September 30) 2004, 2005 and 2007. We selected not only those stations that kept the longest continuous datasets but also the ones that cover the most representative soil and vegetation types. In total, we used 9 hydro-meteorological to compare with model outputs. Table 4.2 summarizes the characteristics of the stations used for model calibration and validation. We performed a manual calibration approach by modifying the value of some hydrological soil properties within a reasonable range of variable values and evaluated the difference with observed soil moisture and soil temperature. The soil parameters evaluated were pore distribution index (m), air entry bubbling pressure (ψ_b) and conductivity decay parameter (f) and the optimum value was selected when minimum value of root mean squared error was achieved. Conversely, saturated hydraulic conductivity (K_s), soil moisture at saturation (θ_s), residual soil moisture (θ_r) and porosity (n) were estimated from pedotransfer functions (Saxton et al., 2006) based on FAO or field textural data and were not modified during the calibration process. Model performance during the calibration/validation process was evaluated using the following statistical metrics: Mean absolute error (MAE), root mean squared error (RMSE), correlation coefficient (CC) and bias. For a description of the statistical metrics, the reader can reference Méndez-Barroso et al., 2014.

4.3. Results and Discussion

4.3.1 Evaluation of Model Performance: Model Calibration

The performance of the hydrological simulations was evaluated through one summer monsoon season (June 1st to September 30) with a time resolution of one hour. We selected a set of stations that represented the most representative soil types and land cover of the San Miguel River Basin. Different monsoon years were utilized for model runs due to the lack of continuous hydrological observations on the selected subset of hydrological stations (see Table 4.2 for monsoon season used in model calibration). Model parameterization includes the manual tuning of six soil variables described in section 4.2.6. The optimal soil parameters were selected when the minimum root mean squared error between simulated and observed soil moisture and soil temperature was achieved.

Table 4.3 shows the soil parameters after the calibration process. The values of saturated hydraulic conductivity (K_s) range from 5 to 49.1 mm/h. The lowest values of hydraulic conductivity were found in Xerosols and Phaeozem with medium texture. Conversely, the highest K_s values were found in Regosols and Yermosols with coarse texture. These later soils are characterized by a high fraction of coarse unconsolidated material and very common in arid and semiarid areas. The high fraction of sand allows water to infiltrate rapidly (Brady & Weil, 1996). Xerosols are soils that are poor inorganic matter but can have layer rich in clays or caliche that do not allow water infiltration and prevent soil erosion while Phaeozem are found in flat areas with considerable organic matter in the upper layers that helps to retain soil moisture, therefore in both cases decreasing hydraulic conductivity. The values of hydraulic conductivity, saturated soil moisture and porosity found in San Miguel River Basin agreed with those found by other authors on similar soil textural types and classification (Clapp & Hornenberg, 1978; Freeze and Cherry, 1979; Batjes, 2009). Regosols showed low soil porosity and saturated soil moisture (0.38 and 0.40 respectively) whereas Fluvisols and Phaeozem obtained the highest values of these hydraulic soil properties (0.50 and 0.51 respectively).

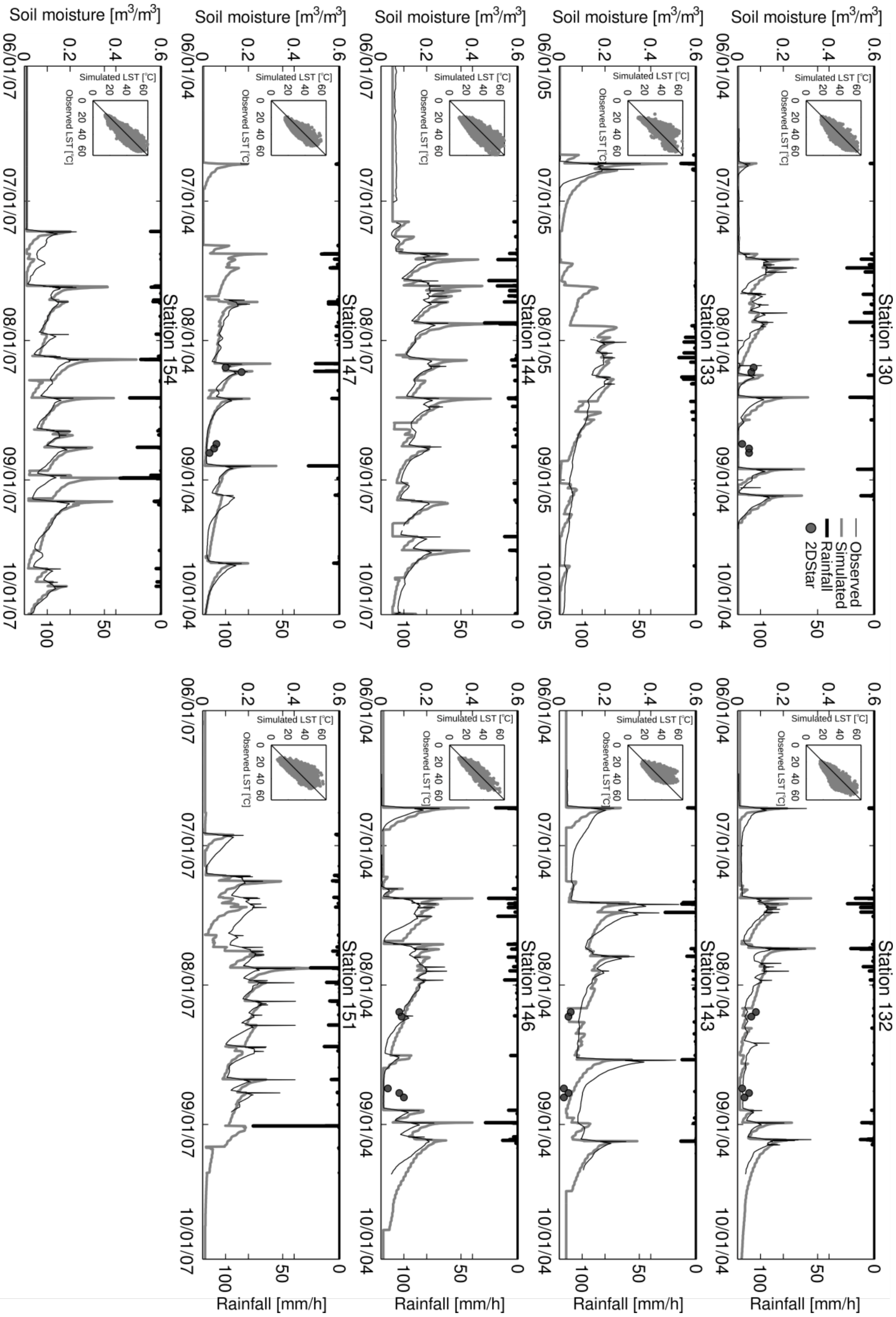

Figure 4.4. Model Calibration at Different Hydro-Meteorological Stations Using Surface Soil Moisture at 5 Centimeters Depth. Stations Represents Different Soil Types as Well as Land Cover. Solid Triangles Show the Values of 2Dstar Soil Moisture Whereas Gray and Black Lines are Simulated and Observed Soil Moisture. Inner Plots Show the Comparison Between Observed and Simulated Land Surface Temperature (LST).

Root mean squared error (RMSE), correlation coefficient (CC) and mean absolute error (MAE) between observed and estimated soil moisture were the statistics metrics used to evaluate model performance (table 10). RMSE values on calibration process ranged from 0.015 to 0.044 m^3/m^3 with a mean of 0.027 (±0.009 m^3/m^3). The best model performance occurred on the EC tower (ST-147) followed by the hydro-meteorological stations 130 and 132 with RMSE values of 0.015, 0.018 and 0.02 respectively. Moreover, these stations also obtained very low mean absolute errors (0.012, 0.013 and 0.016), high correlation coefficients (0.91, 0.94 and 0.90) and relatively good accuracy (-2.6, 17.8 and 5.1 % bias). Figure 4.4 shows the temporal evolution of observed and simulated soil moisture as well as the comparison with land surface temperature. As observed, stations 130,132 and 147 capture very well the temporal evolution of soil moisture and surface temperature during the monsoon season 2004. The hydrological model tRIBS was able to capture and simulate the response to rainfall pulses, recession time and the dry out period accurately in these stations. To add more confidence to our model calibration, these stations are located in three different soil types (ST147 = Yermosol, ST130 = Regosol and ST132 = Lithosol).

These soil types represent representing nearly 74 % of the total area of the basin. In addition, stations 132 and 147 agreed well with measurements of remotely sensed soil moisture from the Two-dimensional Synthetic Aperture Radiometer (2D-STAR), especially on wet days in station 147 and dry days in station 132. Other stations that obtained a very good calibration performance were stations 133 and 144 with relative low root mean squared error (0.021 and 0.028 respectively), very high correlation coefficients (0.947 and 0.948) and excellent degree of accuracy (-1.2 % and 5.8 % difference with observations). Stations 133 and 144 were found in Fluvisols that increase the represented area of the San Miguel River Basin in 77 %. These stations tracked very well the temporal evolution of surface soil moisture and the values were quite closed to observation. However, there were some problems in reproducing peak values after rainfall events.

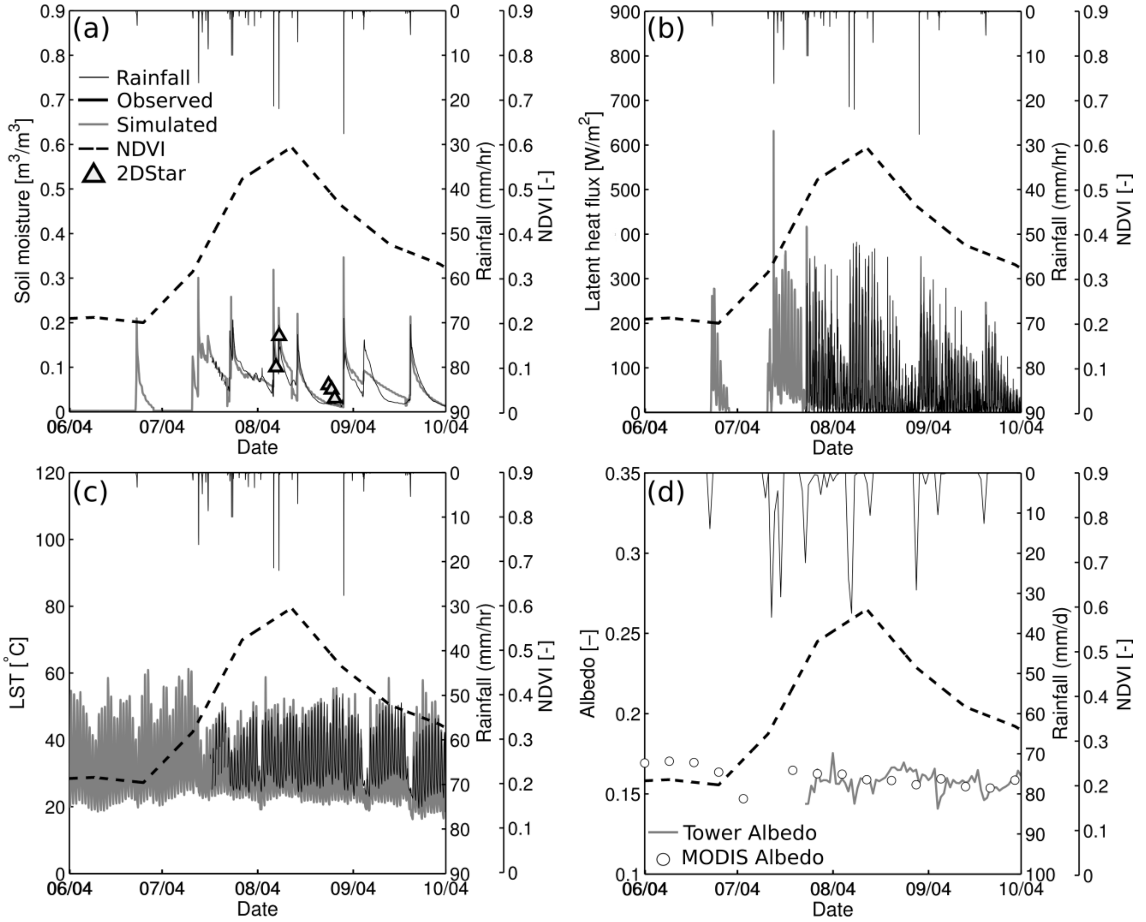

Figure 4.5. Model Calibration at the Subtropical Scrubland EC Site Using: (a) Soil Moisture, (b) Latent Heat and (c) Soil Surface Temperature. Dashed Black Lines Represent Vegetation Development at the Site Using Normalized Difference Vegetation Index (NDVI). Solid Triangles in (A) Show The Values of 2Dstar Soil Moisture Whereas Gray And Black Lines in (a) and (b) are the Simulated and Observed Soil Moisture and Latent Heat Respectively. Finally, (d) Shows The Comparison Between Daily Maximum Albedo Measured at the Tower Location (Gray Lines) With MODIS Albedo Product (Open Dots).

Usually these stations greatly underestimated the peak values but represents very well values during dry up periods specially station 144 which capture the recession times in later period of the monsoon. Station 133 was not as good as station 144 in capturing the dry up period and large differences was found in this period between observations and simulated surface soil moisture. The rest of the stations had a moderately good performance with RMSE values ranging from 0.030 to 0.044, correlation coefficients ranging from 0.89 to 0.91 and bias values in the range of -10.7 % up to 27.6 %.

Station ID	*Soil type*	*Soil texture*	*BIAS (%)*	*MAE*	*RMSE*	*CC*
130	Lithosol	Coarse	17.88	0.013	0.018	0.937
132	Phaeozem	Medium	5.14	0.016	0.02	0.907
133	Regosol	Coarse	5.82	0.015	0.021	0.947
143	Regosol	Medium	-21.70	0.033	0.044	0.852
144	Xerosol	Medium	-1.26	0.021	0.028	0.948
146	Xerosol	Fine	27.68	0.024	0.032	0.944
147	Fluvisol	Coarse	-2.61	0.012	0.015	0.912
151	Fluvisol	Medium	-10.79	0.026	0.038	0.91
154	Yermosol	Coarse	4.49	0.015	0.029	0.899

Table 4.4. Statistical Metrics for Model Calibration Using a Set of Hydro-Meteorological Stations at San Miguel River Basin.

Station 143 showed the poorest performance among stations with a RMSE value of 0.044 a MAE of 0.033 and a correlation coefficient of 0.85 and an underestimation of shallow soil moisture of -21% in comparison with station measurements. As observed in figure 4.4, this station underestimated peak values and also could not capture well the dry up periods. Estimated soil moisture rapidly decreases in dry periods while observations decayed in a steady manner with prolonged dry up periods. However, this station got a good match between estimated surface soil moisture (gray solid line) and remotely sensed soil moisture measured with two-dimensional synthetic Aperture radiometer (Jackson et al., 2009). Without doubt, station 147 (EC tower) obtained one of the best performances in model calibration. Due to the capability of reproduction of soil moisture and temperature and the existence other surface observations, we will focus on the temporal evolution of surface energy fluxes such as latent heat and terrain albedo. For example; figure 4.5 shows the comparison between observed and simulated soil moisture (Figure 4.5a), latent heat flux (Figure 4.5b), land surface temperature (Figure 4.5c) and short wave albedo (Figure 4.5d) at the Eddy covariance tower site.

Station ID	Soil Type	Soil texture	BIAS (%)	MAE	RMSE	CC
130	Lithosol	Coarse	-17.37	0.017	0.025	0.882
132	Phaeozem	Medium	-12.39	0.016	0.02	0.921
133	Regosol	Coarse	-2.72	0.016	0.029	0.928
143	Regosol	Medium	-40.41	0.062	0.068	0.94
144	Xerosol	Medium	-18.21	0.038	0.048	0.839
146	Xerosol	Fine	-4.99	0.019	0.027	0.942
147	Fluvisol	Coarse	12.14	0.012	0.017	0.953
151	Fluvisol	Medium	-23.78	0.026	0.039	0.887
154	Yermosol	Coarse	17.67	0.029	0.039	0.835

Table 4.5. Statistical Metrics for Model Validation Using a Set of Hydro-Meteorological Stations at San Miguel River Basin.

For reference, this figure includes the evolution of vegetation growth expressed as Normalized Vegetation Index (NDVI) and represented with a dashed line. The NDVI time series shown in figure 4.5 represents very well the seasonal phenology of subtropical scrubs characterized by a sudden increase in vegetation greening with the arrival of summer precipitation and a fast decay to dormant conditions at the end of the monsoon period. In particular, the monsoon season 2004 showed a very pronounced intra-seasonal drought in mid-August to early-September that led to fast decay in vegetation greening. For this reason, there is a considerable impact in energy fluxes and surface temperature at the end of the monsoon season.

Despite these intra-seasonal changes in surface conditions, the hydrological model was able to reproduce this variability in simulated hydrological variables. For instance, there was a considerable reduction in the latent heat flux at the end of the monsoon season (September) notably influenced by the rapid decrease in vegetation vigor (figure 4.5b). Similarly, there was also an increase in land surface temperature (figure 4.5c) due to the decrease in vegetation activity. In both cases, the model was able to track the changes in magnitude and timing of latent heat and land surface temperature. However, there was a clear overestimation in minimum land surface temperature during diurnal cycles.

These results emphasize the importance of incorporating the temporal evolution of vegetation vigor, fraction of soil covered by vegetation and albedo in hydrological modeling. Because the importance of albedo in the partition of surface energy fluxes, we have included a comparison between 8-days composites of MODIS short-wave albedo with daily time series of surface albedo measured at the tower location (figure 4.5d). The goal of this figure is to demonstrate that MODIS albedo is capturing the temporal variability of the site and it is representing well the surface conditions during the shift in vegetation greening. It is clear that MODIS-albedo is capturing well the transition from dry to wet conditions. Albeit the limitation in continuous observations, MODIS was able to track the seasonal decrease in surface albedo. Therefore, MODIS albedo is a reliable indicator of diffuse reflectivity of incoming solar radiation in semiarid areas and could be used to represent the partition of energy fluxes at the surface.

4.3.2 Model Validation at Point Scale

Statistical metrics showed very similar results to model calibration (Table 4.5). However, there is general increase in over/underestimation of simulated soil moisture (increase/decrease in bias). In similar fashion to model calibration, best model performance occurred on the EC tower (ST-147) followed by the hydro-meteorological stations 130 and 132 with RMSE values of 0.017, 0.02 and 0.025 respectively. Moreover, these stations obtained very low mean absolute errors (0.012, 0.016 and 0.017) and high correlation coefficients (0.95, 0.92 and 0.88). Conversely, model accuracy in soil moisture estimation decreases in comparison with calibration. Station 147 overestimates soil moisture in 12.1 % while stations 130 and 132 underestimated in 12.3 and 17.3 % respectively. Notwithstanding, there was a big improvement in model performance at station 146 in comparison to model calibration. For example, RMSE decreased from 0.032 to 0.027 and MAE from 0.024 to 0.019 whereas correlation coefficient practically did not change (0.94). There was a huge improvement in the accuracy of estimated soil moisture in this station by going from an overestimation of 27.6 % to an underestimation of only 4.9 %. Station 133 is still a very reliable location with good statistical metrics during model validation. This station obtained a moderately low RMSE (0.029), high correlation coefficient (0.93) and very low MAE (0.013). Even more important, this station improved its accuracy in estimating surface soil moisture by decreasing percentage of bias from an overestimation of 5.8% to an underestimation of 2.2%. The rest of the stations had similar statistical metrics in comparison to those obtained in model calibration. One great exception is station 144 which performance in the validation got worse by increasing its RMSE from 0.028 to 0.048, increasing the MAE from 0.021 to 0.038, decreasing the correlation coefficient from 0.95 to 0.83 and increasing the underestimation of soil moisture from 1.2% (the best obtained in model calibration) to 18 %. Finally, station 143 remained as the station with the poorest performance with the highest RMSE (0.068), the highest MAE (0.062) and the highest discrepancy with observed soil moisture due to an underestimation of 40.4%. At the same time, station 144 obtained a very high correlation coefficient of 0.94 (second highest in the validation process) which suggest that estimated soil moisture is capturing the variability of soil moisture but systematic errors in measuring observed soil moisture could lead to mismatch of simulated soil moisture.

In summary, there were mixed results after the validation process. One station (146) improved their performance on the validation process while station 144 worsened the estimation of soil moisture during the validation. Most of the stations remained with the same performance during both the calibration and validation process. Remarkably, stations 147, 130, 132 and 133 obtained the best performances during calibration and validation that aggregated confidence to model set up because these stations represent close to 77% of the soil types and nearly 50% of the lands cover types in the San Miguel Valley.

4.3.3 Spatial Validation of Soil Moisture and Land Surface Temperature

Figure 4.6 shows the comparison between the spatial distribution of estimated soil moisture and land surface temperature with two remote sensing products.

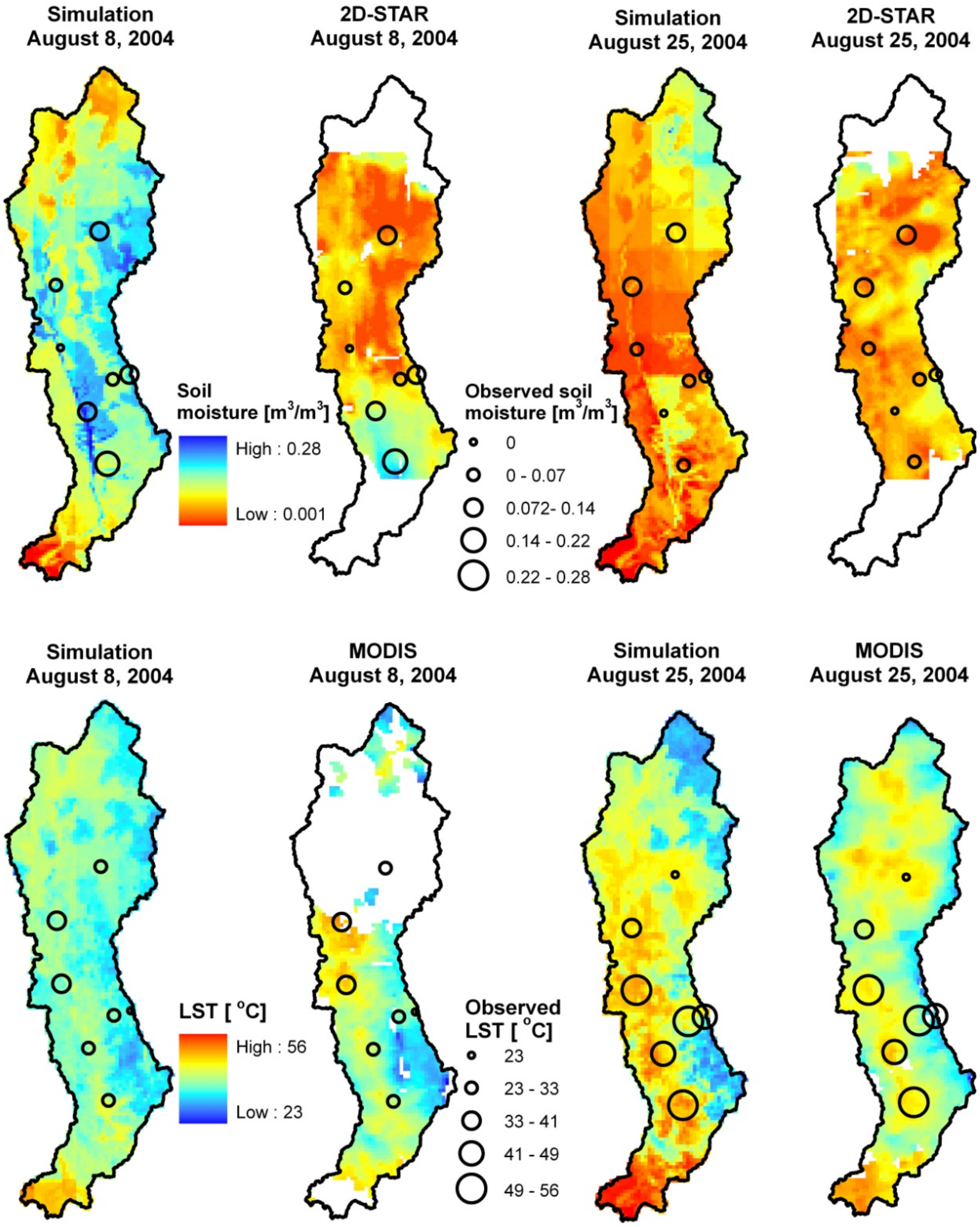

Figure 4.6. Model Calibration Using Different Distributed Products. Upper Set of Images Shows the Comparison Between Simulated Soil Moisture With the One Estimated from the Radar-Based 2D-STAR (2 Dimension Synthetic Aperture Radar). Bottom Set of Figures Show the Comparison Between Simulated and MODIS Land Surface Temperature. Comparison Between Simulated and 2D-STAR Soil Moisture as Well Simulated and MODIS Land Surface Temperature Were Carried Out on August 8 (Wet) and August 24 (Dry), 2004 as Part of the SMEX-04. Hollow Circles Represent Magnitude in Soil Moisture or Surface Temperature Measured in the Network of Hydro-Meteorological Stations.

Upper part of figure 4.6 shows the comparison between model-estimated soil moisture and soil moisture estimated from Two-dimensional Synthetic Aperture Radiometer (2D-STAR) in two contrasting precipitation conditions. The first comparison was made on August 8, 2004; a reasonable wet day followed by a mean basin precipitation of 10.5-mm. The second comparison was made on August 25, 2004; a very dry day followed by a mean basin precipitation of 0.03 mm. The 2D-STAR sensor flew over Rio San Miguel River Basin on August 8 at 10:00 AM local time and again at 14:00 PM on August 25. Conversely, the bottom part of figure 4.6 shows the comparison between model-estimated land surface temperature and the one estimated from Moderate Resolution Imaging Spectroradiometer (MODIS) on the same days that 2D-STAR overflew the region.

Two different MODIS platforms were used due to image quality (% of cloud cover). MODIS-Terra was used on August 8 and overpassed the region at 11:00 AM local time while MODIS-AQUA was used on August 25 and overpassed the region at 13:00 PM. Large spatial discrepancies were found between modeled and measured soil moisture on August 8 (wet day). The hydrological model forecasted an almost entirely wet basin with the exception of the extreme southern and northern regions that remained with very low soil moisture values (close to 0 m^3/m^3). The model estimated saturated conditions along the floodplains, the river network and high elevations of the San Miguel River Basin with soil moisture values close to 0.28 $m^3/m^{3.}$. In contrast, 2D-STAR only measured high surface soil moisture on the southern part while most the basin was dry. Lack of spatial correlation can be demonstrated by statistical metrics shown in table 11. The very high value of bias (2.13) indicates that the hydrological model is clearly overestimating soil moisture in comparison with 2D-STAR observations. The extreme low correlation coefficient (CC<0.05) suggests lack of spatial correspondence in spatial patterns. A slightly improvement in the range of values but not in the representation of spatial patterns occurred in August 25. Model estimated wet floodplains and a moderately wetter northern region while 2D-STAR did not show a clear pattern of wetter floodplains or river network but measured scattered clusters of high soil moisture. As shown in Table 4.6, the range of values of estimated soil moisture was closed to those measured by 2D-STAR. Calculated bias between simulated and observed soil moisture was 0.90 (with 1 as a perfect match) with a slightly increase in spatial correlation (R^2=0.08) but still showing lack of correlation in spatial patterns. There is also a moderately improvement in model accuracy by the decrease in MAE (0.02). Lack of spatial correlation between modeled soil moisture and measured by 2D-STAR could be attributed to the source of meteorological forcing used for the hydrological simulations. NLDAS (North American Land Data Assimilation System hourly meteorological forcing data was used as input for the hydrological simulations in Rio San Miguel River Basin. NLDAS precipitation dataset is constructed from gauge-based observed precipitation data and is temporally disaggregated using stage II radar data (involving statistical methods). Furthermore, bias-corrected shortwave radiation and surface meteorology is calculated from previous model-based reanalysis (Mitchell et al., 2004). Undoubtedly, not only the statistical temporal disaggregation of NLDAS precipitation is inducing a degree of uncertainty in precipitation values but also the spatial aggregation (12 km) of NLDAS pixel is inducing bias in spatial variability of rainfall. It is well known that rainfall in the North American Monsoon region is characterized by concentrated storms in a short period of time and highly variable in space usually with isolated storms occurring in relative short distances (Liebmann et al., 2008; Gebremichael et al., 2007). Therefore, the high spatial variability of NAM rainfall events is not intrinsic in a12-km pixel of NLDAS. This uncertainty raised the question whether a 12-km pixel represents the rainfall characteristics of the NMA region. Despite the advances in rainfall data availability, the problem of highly temporal and spatial variability in the semiarid areas still persist and still remain as a common problem in hydrological modeling in semiarid areas (Pilgrim et al., 2009).

On the contrary to soil moisture, land surface temperature had a much better match between model-estimated and measured land surface temperature. Both products showed common spatial patterns on both days, for instance; on August 8, both products were able to represent warm regions around the flood plain of the San Miguel River and the southern region close to the basin outlet. Furthermore, both products agreed in the location of the cool zones allocated mainly on high elevations of San Miguel River Basin (figure 4.6). Table 4.6 shows the statistics metrics used to evaluate the performance of the spatial validation of land surface temperature in San Miguel River Basin. As observed, there is a good agreement between modeled and measured land surface temperature on August 8 with a slightly underestimation in temperature values (bias=0.95, where 1 is a perfect match) and a very low error of just 1 degree Celsius. Spatial patterns were very well correlated (0.52) with the exception of the central region of the San Miguel River Basin, for instance; 2D-STAR measured high temperatures on the central region of the basin while the hydrological model forecasted low temperatures. As explained before, forcing data is causing the bias between model-estimated and measured land surface temperatures due to possible overestimation in some regions of precipitation. It is clear that NLDAS rainfall is adding more precipitation in some places that disagreed with observations; one clear example is the north-central region of San Miguel River Basin (August 8), Although is a wet day, the spatial representation of rainfall differs in both sensors. NLDAS assumed an even distribution of rainfall in the basin while 2D-star inferred wetter southern region and a drier north region. This latter statement is confirmed by drier north-central region leading to higher temperatures. However, there was a big improvement in correlation of spatial patterns on August 25 (dry day). The spatial correlation of land surface temperature increased from 0.52 to 0.64 with a good agreement in the range of values (bias =1.03) albeit MAE slightly increased (2.2 degree Celsius). There is a clear mismatch between observed variables at the stations with those from model-estimated or 2D-STAR. Such discrepancies are attributed to differences in scale between remote sensing products and point observations. However, the agreement between point observations and remote sending products improved on August 25 (dry conditions) in both soil moisture and land surface temperature but remarkably soil moisture obtained a high correlation coefficient (0.55) and a relative low MAE (0.02).

4.3.4 Time Series of Basin-Averaged Hydrological Variables from 2004 through 2010

Figure 4.7 shows the basin-averaged time series of vegetation fraction, soil moisture, land surface temperature and evapotranspiration in the San Miguel River Basin during the simulation period June 2004 through September 2010.

	Surface Temperature			
Date	Comparison	Bias [-]	CC [-]	MAE[°C]
Aug 8, 2014	Simulated vs MODIS	0.95	0.52	1.01
Aug 25, 2014	Simulated vs MODIS	1.03	0.64	2.22
Aug 8, 2014	Simulated vs Observed	1.25	0.01	7.83
Aug 25, 2014	Simulated vs Observed	0.99	0.14	7.21
	Surface Soil Moisture			
Date	Comparison	Bias [-]	CC [-]	MAE[-]
Aug 8, 2014	Simulated vs 2DSTAR	2.13	0.02	0.06
Aug 25, 2014	Simulated vs 2DSTAR	0.90	0.08	0.02
Aug 8, 2014	Simulated vs Observed	2.30	0.18	0.09
Aug 25, 2014	Simulated vs Observed	1.6	0.55	0.02

Table 4.6. Statistical Metrics of the Comparison Between Observed Soil Temperature and Moisture With Those Measured With Two Remote Sensing Sensors (MODIS and 2D-STAR).

The hydrological model captured very well the inter-annual variability and helps us to identify wet and dry years by the magnitude and temporal persistence of soil moisture, evapotranspiration and vegetation fraction. For example; it is clear that year 2005 is the driest year during the simulation period with low ET and soil moisture values and highly concentrated only during the summer season. Conversely, year 2008 showed slightly higher vegetation fraction and considerable higher evapotranspiration fluxes and soil moisture during the summer. Furthermore, this figure can also show some abnormal winter precipitation leading to high water fluxes in the San Miguel River Basin. The region is characterized by showing winter precipitation as results of frontal systems with low frequency events unlike local convection systems common in summer precipitation. However, there some year of unusual winter precipitation that can lead to high ET and soil moisture values. These unusual wet winters are enhanced by meteorological phenomena such as El Nino (ENSO), la Nina or Inter-decadal Oscillation.

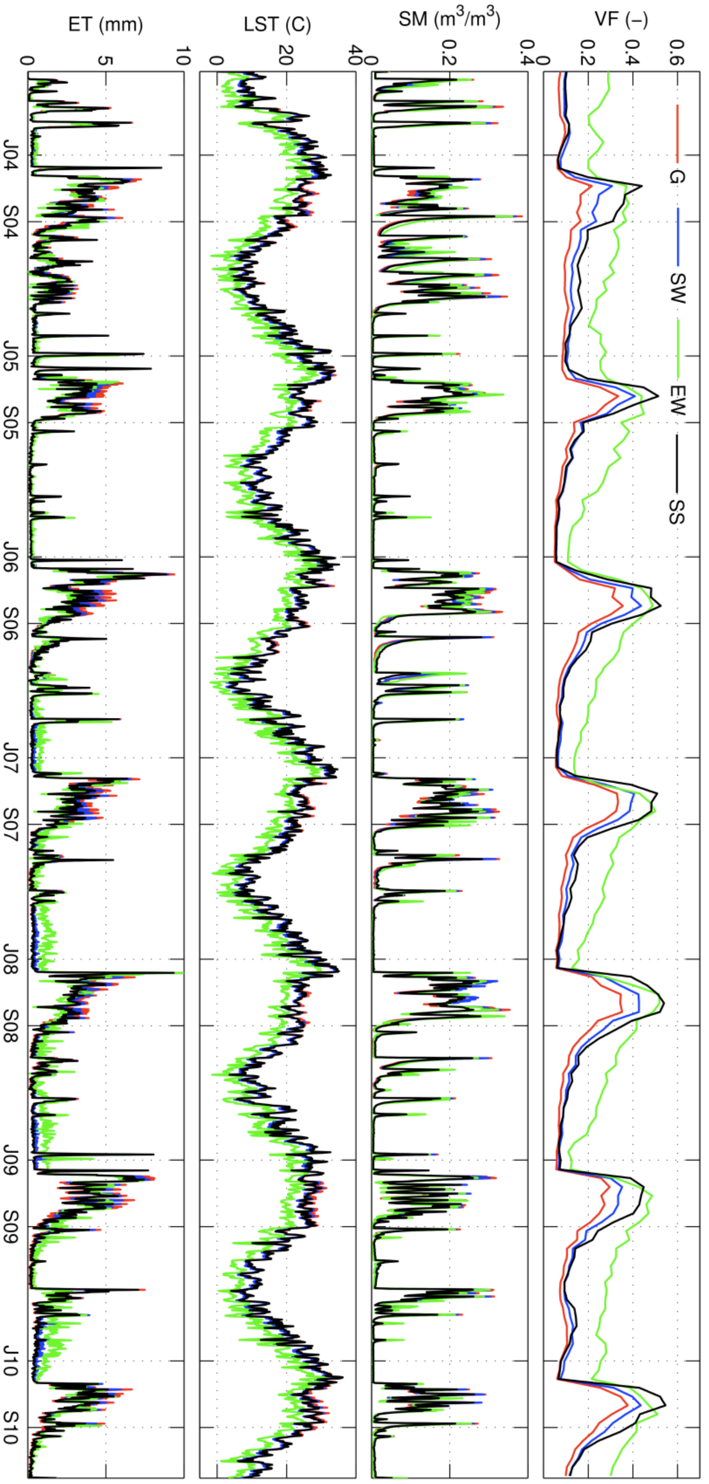

Figure 4.7. Time Series of Hydrological Variables and Vegetation Fraction Among Ecosystems in the San Miguel River Basin. The Ecosystems Shown in this Figure are: Grassland (G), Sparse Woodland (SW), Evergreen Woodland (EW) and Subtropical Scrubland (SS). The Time Series Encompasses the Period from June 2004 Through September 2010.

It is well know that El Nino increases winter precipitation in the NAM while La Nina tends to increase summer precipitation (Brito Castillo et al., 2003). As shown in figure 29, winter season of years 2004 and 2010 were wetter than other winter seasons whereas year 2008 was the wettest during the period 2004-2010. In fact, years 2004-2005 and 2009 coincide with reports of weak and moderate El Niño years that led to increase in winter precipitation. In the other hand 2008 coincided with reports of La Nina events that produced a wetter summer (CPC, 2014). Therefore, this time series in water fluxes could be a useful tool to see the impacts of global meteorological systems in regional water fluxes. In addition, figure 29 can give us an insight of the differences in hydrological variables among ecosystems within the San Miguel River Basin. For example; Notice that most of the ecosystems in the San Miguel River Basin have a strong response to the rainfall pulses of the North American Monsoon.

Subtropical scrubland (SS), sparse woodland (SW) and grassland (G) have high intensity (high slope to peak), quasi-symmetrical peaks (fast time to peak and fast recession curve) which is the main feature of subtropical ecosystems with high response to NAM rainfall (Méndez-Barroso et al., 2009; Forzieri et al., 2011). Nevertheless, subtropical scrublands can develop vegetation fraction as high as evergreen but with very different recession curves during the year. Evergreen vegetation showed steady annual decline in vegetation fraction while the rest of the ecosystems showed shorter productivity with fast decline in vegetation fraction. Forzieri et al., (2011) found similar results by analyzing time series of MODIS-NDVI in the North American Monsoon region (NAM). There are clear differences in water use by vegetation type. For example, despite the lowest soil moisture on subtropical scrublands, they tend to produced higher vegetation cover and high ET during the summer growing season while grasslands showed eve higher soil moisture and evapotranspiration than subtropical vegetation but lower vegetation fraction.

Sparse woodland showed intermediate soil moisture, vegetation fraction and ET values between subtropical scrublands and grassland. Evergreen vegetation experienced vegetation cover values as high as subtropical vegetation with a steady decrease during the rest of the year. Soil moisture was slightly lower than grasslands but higher than subtropical vegetation and ET was as high as grasslands in summer but definitively this evergreen forest had the highest ET and soil moisture values during the winter period. These differences in water fluxes and vegetation fraction suggest that some ecosystems are more efficient to uptake soil moisture and produce aboveground biomass (directly related to vegetation fraction). Without doubt, subtropical scrublands were the most efficient ecosystems in water use because of the very high vegetation cover with less surface soil moisture values among all the analyzed ecosystems followed only by evergreen woodlands. Grasslands were the most inefficient water-use ecosystems because of low vegetation fraction with high soil moisture. Méndez-Barroso et al., (2009) found that Sinaloan thornscrub (subtropical scrub in this work) was the most efficient ecosystem in water use in the NAM region based on time series analysis of rainfall data and time integrated-NDVI followed by Madrean Woodland (evergreen woodland). Finally, there is a clear distinction between land surface temperatures among the ecosystems found in the San Miguel River Basin. To illustrate this, evergreen woodland is significantly lower than the rest of the ecosystems during the simulation period. The high vegetation cover and soil moisture decreases surface albedo, hence; the amount of radiation scattered back to the atmosphere resulting in a decrease in surface temperature. Furthermore, the combination of high fraction of vegetation to bare soil, high soil moisture and creates a cooling effect related to release of latent heat.

4.3.5 Spatial Distribution of Seasonal-Averaged Evapotranspiration and Soil Moisture

Figure 4.8 shows the comparison between the basin-distribution of seasonal evapotranspiration and soil moisture. Upper part of the figure shows the comparison between summer (July, August and September) and winter (December, January and February) soil moisture. Both summer and winter seasons have in common a wetter north region with a drier south interconnected by a very humid floodplain. Soil moisture values in the summer ranges from 0.056 located mainly in the south up to 0.51 in the floodplains. Undoubtedly, soil type is exerting a very strong control in the spatial distribution of soil moisture specially those soils with high porosity and low hydraulic conductivities such as lithosol with medium texture, xerosol with medium texture, regosol with medium texture and fluvisol with coarse texture. These soil types are characterized by a high capacity of water storage per volume of bulk material but they cannot release the water rapidly, therefore; they act as clay-rich soil with strong water retention properties. Main floodplain is composed of fluvisol and holds the highest values of soil moisture in the basin. Regosols and lithosol with medium texture can also act as a great reservoir of water in soil that is quite observable in the spatial distribution of soil moisture. In winter soil moisture values drastically drops to values ranging from 0.0094 to no more than 0.1074. Conversely, basin evapotranspiration is not entirely controlled by soil type but also vegetation fraction is having a strong control on its distribution. Similarly to soil moisture, evapotranspiration values are much higher during the monsoon season than in winter time. However, the basin is not as clearly divided in two humid regimes (wet north and dry south) as in the case of soil moisture. Summer values ranges between 217 to 600 mm with larger ET values found in sparse woodland and agricultural areas. Low ET values are associated to high infiltration and soils like fluvisol with medium texture. This type of soil rapidly infiltrates water to deeper soil horizons where could not be up taken by plants roots and released back to the atmosphere. This is clearly observable by identification of very los values in ET in the southern region of the basin. ET during the winter showed a similar spatial distribution to the summer one. ET values ranged from 0 to 74 mm with high values distributed mainly in the riparian corridor and high elevation woodlands.

4.3.6 Temporal and Spatial Evolution of the Ratio ET/P and Q/P

Figure 4.9 shows the temporal and spatial evolution of the ratio evapotranspiration to precipitation (ET/P) during the summer season. The figure shows exclusively the average of the months July, August and September within the simulation period 2004 through 2010. In general, an increasing gradient from low to high values of the ratio ET/P is observed as the monsoon season progresses from July to August.

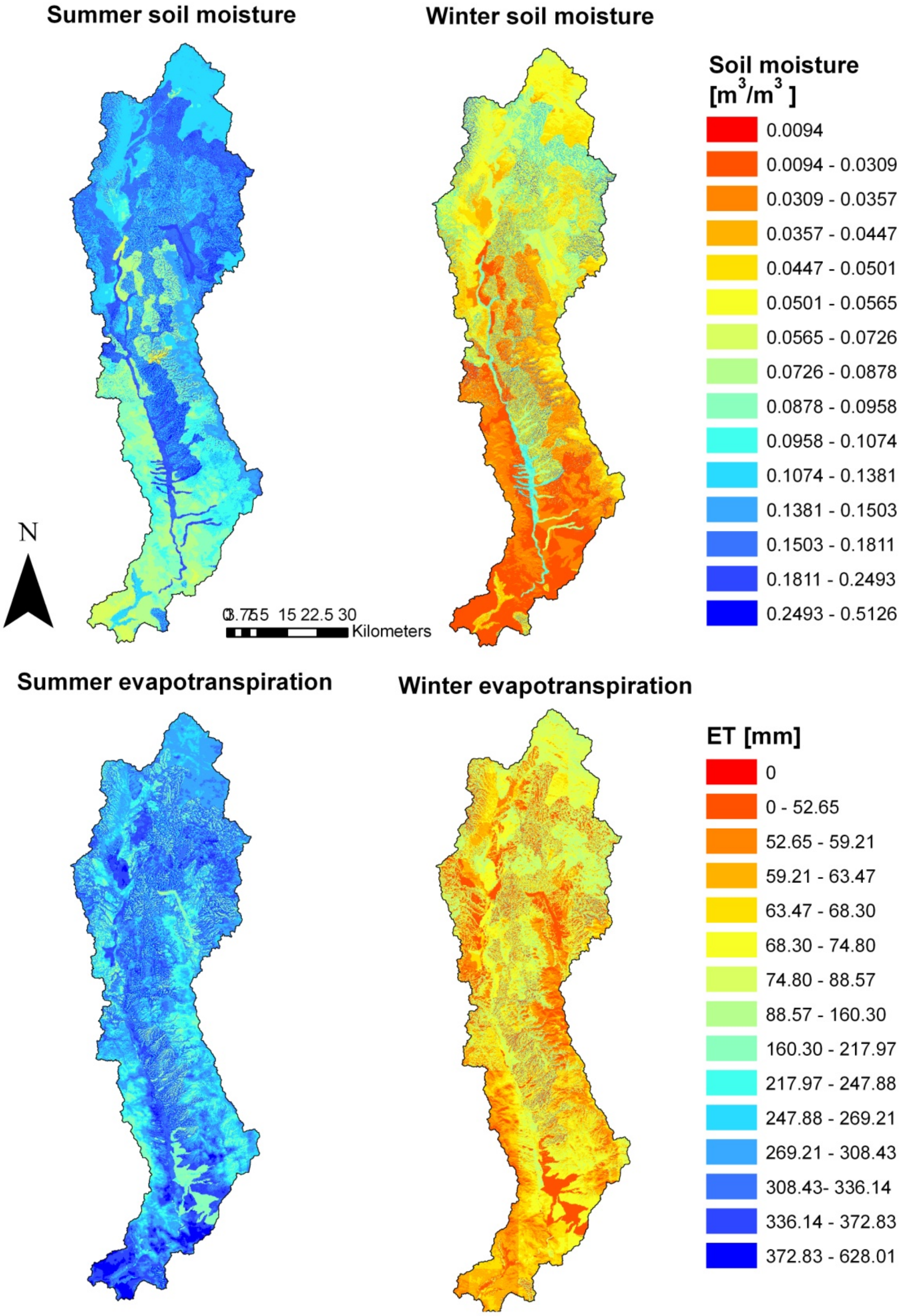

Figure 4.8. Spatial Distribution of Seasonal Evapotranspiration and Soil Moisture Averaged During the Simulation Period 2004-2010. Summer Season Encompasses the Months of July, August and September Whereas the Winter Season includes the Months of December, January and February.

In July, the beginning of the monsoon season, high ET/P are observed only in the riparian corridor and some agricultural regions in the north and south with most of the native vegetation is found with low values of ET/P because of whether precipitation is present is not overpassed by ET fluxes. Nevertheless, August start to increases the ratio ET/P extending from the subtropical vegetation in the south to the grasslands in the north. High elevations ecosystems (evergreen woodland) and soil dominated by medium textured fluvisols remained with very low values of the ratio ET/P.

Figure 4.10 shows the temporal evolution of the ratio ET/P among different ecosystems found in the San Miguel River Basin. The plot shows monthly values of ET/P and standard deviation estimated during the simulation period 2004 through 2010. As observed, Grassland and sparse woodlands were consistently the ecosystems that showed larger values of ET/P, suggesting that these ecosystems are the main sources of basin moisture to the atmosphere. In other words, these two ecosystems can help to sustain the flux or feedback of moisture that can strength the monsoon. Some authors consider the ratio ET/P or Q/P as a proxy for precipitation recycling ratio (Savenije, 1996). Conversely, subtropical scrublands and evergreen woodland showed very similar trending in the temporal evolution of the ratio ET/P during the monsoon. However, the evergreen woodlands showed the highest variability among ecosystems.

Figure 4.11 shows the spatial an temporal evolution of the runoff coefficient (Q/P) during the monsoon season. The progression in the runoff ratio is expressed as monthly values averaged during the simulation period (2004-2010). It is clear that a there is a increase in the runoff ratio as the monsoon season progresses. In July, the entire San Miguel River Basin showed very low values of Q/P ranging from 0 through 0.05. However, as the monsoon progresses the run off ranges from 0.002 up to 0.35 in August and September. As observed in figure 4.11, there is a clear North-South trending in the run off ratio along the Basin where the highest ratios are located in the northern part and decreasing along the San Miguel River to the South. In General, The highest values were located a long the floodplain of the San Miguel River and in the Northern plains where grasslands and shrublands dominate.

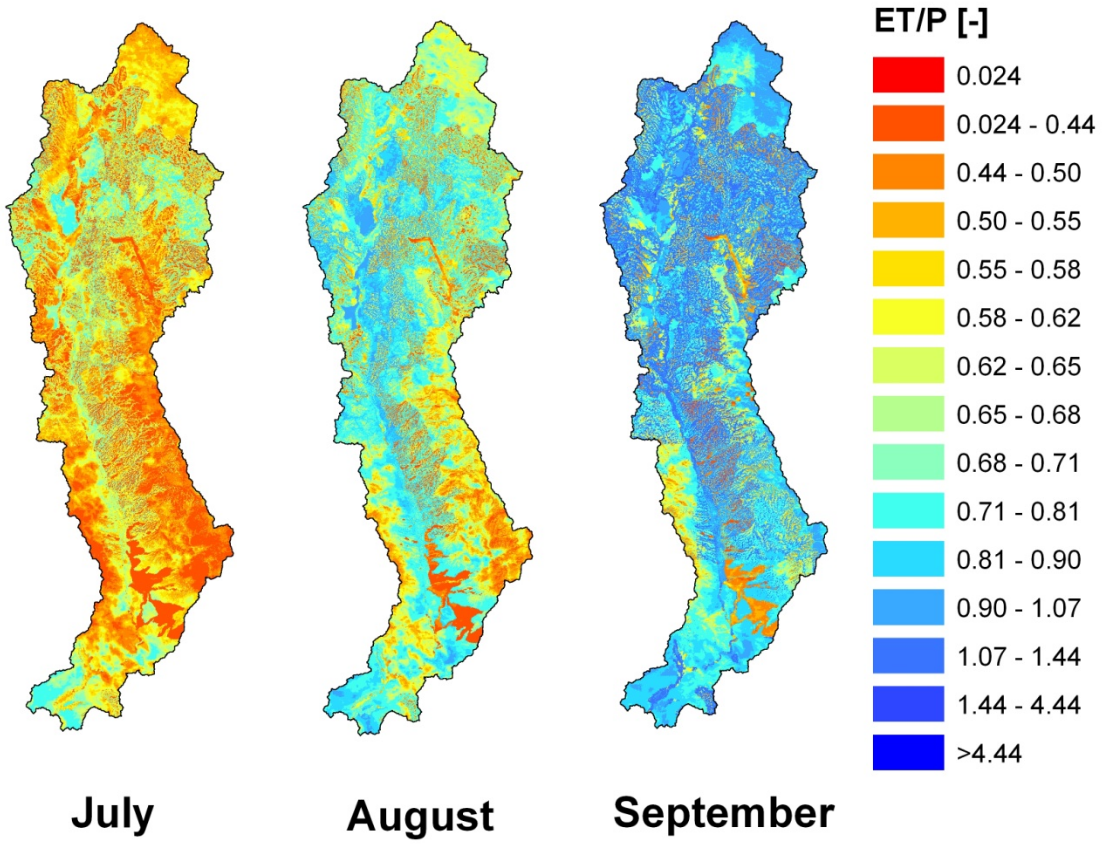

Figure 4.9. Spatial and Temporal Evolution of the Ratio ET/P Averaged During the Simulation Period 2004-2010 in the San Miguel River Basin.

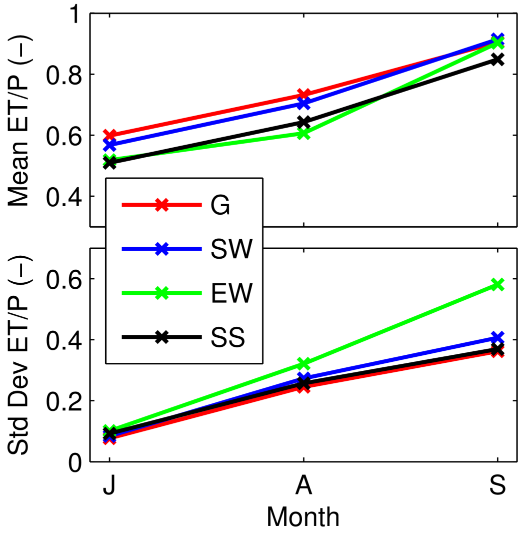

Figure 4.10. Temporal Evolution and Variability of the Estimated Ratio ET/P in Different Ecosystems During The Monsoon Season. The Plot Shows the Monthly Average During the Period 2004-2010 Within The San Miguel River Basin.

Furthermore, There is a strong link between soil texture and values of run off ratio. This statement is evident in the floodplains where fluvisols and regosols are found and phaeozems in the north. These soil types are characterized by fine or medium texture with low to moderate values of hydraulic conductivity. Runoff ratio ranges from 0.26 to 0.35 in the floodplains during September (peak in run off production) while in the northern region runoff ratio ranges from 0.09 to 0.26.

Figure 4.12 help us to understand the temporal progression of the runoff ratio among different ecosystems in the San Miguel River Basin. Furthermore, standard deviation accounts for monthly variability in the period 2004-2010. Overall, sparse woodlands (SS) and grasslands (G) showed higher runoff ratios among the dominant ecosystems in the San Miguel River Basin. Low vegetation fraction and soil characteristics could be reason for high runoff coefficient. In one hand, vegetation helps to attenuate rainfall intensity by intercepting rainfall in leaves and stems, hence, helps to retain water in the surface. If soil is exposed directly to rainfall and this latter overpasses the capacity of water infiltration, then runoff is produced. In addition, Grasslands and sparse woodlands are commonly found in regosol, fluvisols and phaoezems, characterized by slow hydraulic conductivities at the surface, then; delaying the rapid infiltration of water. Conversely, Evergreen woodlands, showed the lowest runoff ratios, except in September with values very similar to grasslands and sparse woodlands. Evergreen woodlands also were very variable in time, however; again in September showed values similar to grasslands.

4.4. Summary and Conclusions

We performed a multiyear hydrologic simulation (2004-2010) by incorporating vegetation seasonality at basin scale to evaluate the inter-annual variability in ecohydrological dynamics on the entire San Miguel River Basin.

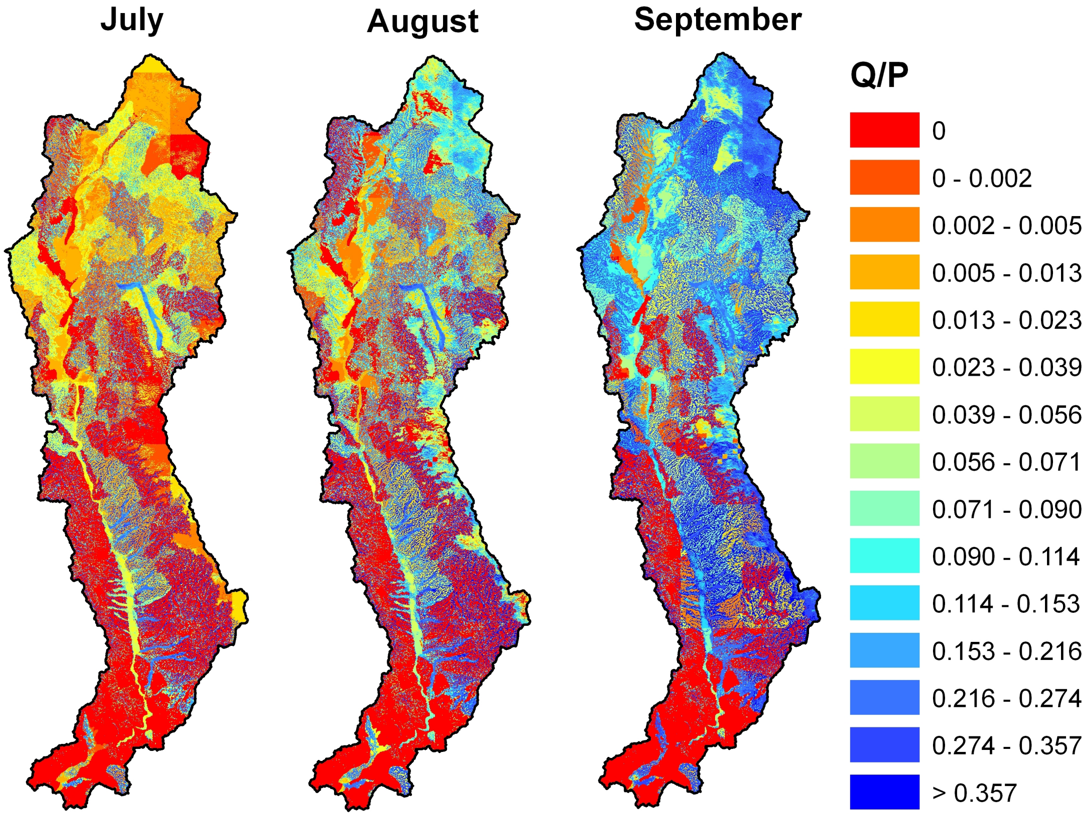

Figure 4.11. Spatial and Temporal Evolution of the Ratio Q/P Averaged During the Simulation Period 2004-2010 in the San Miguel River Basin.

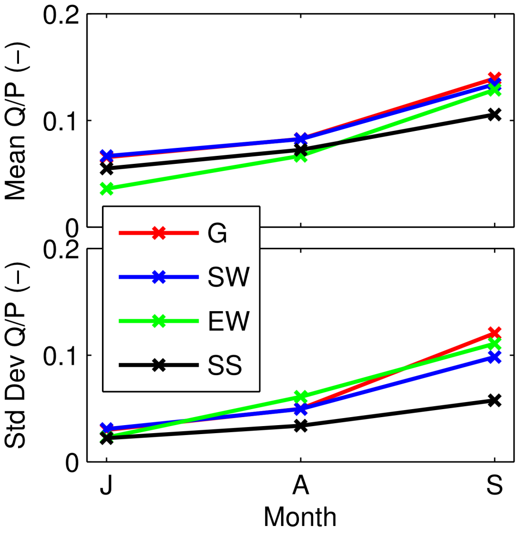

Figure 4.12. Temporal Evolution and Variability of the Estimated Ratio Q/P in Different Ecosystems During the Monsoon Season. The Plot Shows the Monthly Average During the Period 2004-2010 Within the San Miguel River Basin.

The calibration and validation of the model tRIBS relied in observations from 9 hydro meteorological stations deployed in different ecosystems and soil types. Two set of remote sensing observations of soil moisture (2DSTAR) and land surface temperature were used to evaluate the spatial correlation with distributed model outputs. This work is one of the few that showed the evolution temporal and spatial evolution of the ratios ET/P (used as a proxy for precipitation recycling) and runoff ratio in semiarid areas. Furthermore, this work explores the role of the ecosystems found in San Miguel River Basin in sustaining moisture to the atmosphere (high ET/P) and producing runoff. Our most important findings in this work include:

Incorporation of seasonal vegetation greening allows to see clear differences among ecosystems in water fluxes, for example; grasslands and sparse woodlands to return water to the atmosphere that suggest that these two ecosystems are important to sustain rainfall within the basin.

There is an increasing capacity of the basin to return water to the atmosphere as ET/P increases with the progression of the monsoon season. Highest ET/P values were found in September with values ranging from 0.5 to 1. According to our results, Grasslands and Sparse woodlands are the ecosystems that potentially can contribute to sustain precipitation feedback due to high ET/P coefficients.

There is an increasing capacity of the basin to increase the production of runoff (Q/P) as the monsoon season progresses. Similarly to ratio ET/P, the highest runoff ratios values were found in September with values ranging from 0.05 to 0.32.

The hydrological model tRIBS can be used as a tool to identify with high rates of conversion of precipitation to evapotranspiration while others supported the production of runoff. These later statement is very important for the design of water resources management as well as decisions for stakeholders in water use planning.

CHAPTER 5

GENERAL CONCLUSIONS AND FUTURE WORK

This research work represents a step forward in hydrological model in the semiarid basins of the North American Monsoon (NAM) region. As previously mentioned, the basins located in the Northwestern part of Mexico, within the central portion of the NAM domain, experience dramatic changes in vegetation greening leading to sudden changes in surface conditions. Therefore, incorporating the temporal evolution of vegetation and transform it in model parameters represents a big challenge in hydrology. We have utilized a research model, the TIN-based Real-Time Integrated Basin Simulator (tRIBS), to explore the impact of incorporation of vegetation greening at three different temporal and spatial scales on water fluxes. Furthermore, in our efforts to improve basin representation in the semiarid basins, we have tested model sensitivity to the different representations of the spatial distribution of soil textual properties and soil thickness. In the following we describe the main findings of this research work.

Seasonal vegetation greening affects the partitioning of water and energy fluxes in arid and semiarid ecosystems under the influence of the North American monsoon. As a result, modeling applications that assume constant parameters or represent each summer with a fixed seasonal cycle can miss important vegetation impacts. We found good agreement between field observations of evapotranspiration and soil moisture and simulations from Dynamic scenarios, indicating that the hydrologic model can represent interannual differences in the water and energy fluxes in the two ecosystems. Furthermore, the model was able to estimate the temporal evolution of ET partition in the region by incorporating vegetation dynamics. Previous research works in the region only estimate partition of ET in very specific days during the onset of the monsoon season by isotopic composition (Tarin, 2014). However, we have used this limited dataset to corroborated our findings. Our ecohydrological modeling simulations found that subtropical scrublands, with rapid vegetation greening, had a ratio T/ET (fraction of evapotranspiration from plant transpiration) of 56 ± 9% over the five summer periods while oak-savanna stands showed a T/ET ratio of only 18 ± 8%. Results described in this study identify the implications of the two ecosystem types on the water and energy fluxes, specifically on evapotranspiration and its partitioning, which have not been previously known. Intermediate-elevation subtropical scrublands have a high sensitivity to precipitation, primarily during the early development of the NAM, which allow them to quickly transition from soil- to vegetation-mediated losses to the atmosphere. In contrast, high-elevation oak savannas, with a lower sensitivity of canopy development to precipitation, have a slower transition from evaporation- to transpiration-dominated periods. As a result, these extensive water users slowly deplete soil moisture during the NAM, preserving it for subsequent use to maintain greenness and transpiration during the fall.

Surface soil texture exerted a strong control in surface soil moisture (5 cm depth). Wetter regions within SMRB were closely linked to textural classes with large water retention capacities such as clay-rich or sandy-loamy soils. Drier soils are closely linked to high infiltration capacities soils, similar to sandy soils with scarce vegetation. Root zone soil moisture was strongly controlled by spatial variability of soil thickness by creating soil depressions that retained subsurface water. The filling and spilling of these soil depressions greatly affected groundwater exfiltration, especially; when soil depressions were followed by shallow soil thickness. This problem arises in the approaches with complex subsurface topography such as Heimsath and Gessler, however; these two approaches are reliable alternatives to estimate distributed soil thickness particularly in basins with limited information and surveying may be labor intensive and expensive. Soil texture surveying using remotely sensed data was also another reliable alternative for remote basin with lack of soil information. The visible and thermal bands of the Advance Spaceborne Thermal Emission and Reflection Radiometer (ASTER) have demonstrated to be a reliable option for soil texture surveying.

Soil texture exerted a strong control in spatial patterns of soil moisture and evapotranspiration during the transition from dry to wet conditions. Once vegetation vigor and cover fraction are dominating the basin, the influence of soil texture in controlling spatial patterns decreased and vegetation tended to smooth this spatial variability within the basin.

The hydrological model tRIBS was also used as an important tool that allows us to understand the complexity of hydrological processes in semiarid areas. One important contribution of the current research is the understanding of the temporal evolution of the ratios ET/P and Q/P. This work is one of the few that showed the temporal and spatial evolution of the ratios ET/P (used as a proxy for precipitation recycling) and runoff ratio in semiarid areas. Furthermore, this work explores the role of the ecosystems found in San Miguel River Basin in sustaining moisture to the atmosphere (high ET/P) and producing runoff. The incorporation of vegetation dynamics definitively plays a role in the organization of patterns closely related with ecosystems leading to variations in water fluxes. This research recognizes the importance of grasslands and sparse woodlands as important components in basin water balance. These two ecosystems obtained the highest averaged ET/P fractions during the monsoon season (June to September). In general, there is an increasing capacity of the basin to return water to the atmosphere as ET/P increases with the progression of the monsoon season. Highest ET/P values were found in September with values ranging from 0.5 to 1.

Similarly, we found that the capacity of the basin to produce of runoff (Q/P) increases as the monsoon season progresses. Similarly to ratio ET/P, the highest runoff ratios values were found in September with values ranging from 0.05 to 0.32. The hydrological model tRIBS can be used as a tool to identify with high rates of conversion of precipitation to evapotranspiration while others supported the production of runoff. Such differences in these ratios suggested that the ecosystems of the San Miguel River Basin could have different contributions to recycling of precipitation and runoff production. This finding expands our knowledge about the complex interactions between vegetation and water fluxes, which are very important in the development of sustainable management of water and ecosystem resources.

In summary, this research work represents an important contribution in the study of the hydrology in semiarid areas. One big step forward in hydrological modeling is the incorporation of vegetation dynamics in the form of variables that affect the water balance. In this case remote sensing observations were transformed to model parameters to account for seasonal evolution of the vegetation. Secondly, we developed the parameterization of an ecohydrological model for very complex and dynamic ecosystems within the North American Monsoon Region. Furthermore, this research is an example that it is possible to overcome the problem of lack of data by integrating different data sources. The integration of remote sensing, ground observations and ecohydrological models is crucial to understand the complex interactions in semiarid basins. For this reason the current work represents a milestone in understanding the semiarid basins in the NAM region.

We recognize the limitations of the current research work and future work should be done in order to have a better understanding of the ecohydrological processes that can lead to better predictions. The transpiration fractions estimated in this work must be corroborated with other methodologies or approaches to estimate ET partition such as isotopic signal, sap flow or soil chambers. In addition, more ground observations are required to improve model calibration. These observation include close monitoring of vegetation phenology and a more accurate measurement of the fate of rainfall such as rainfall infiltration, interception by canopy, stem flow, channel losses and surface runoff.

The results of this research can help to aware water agencies and academic institution the important to expand networks of hydrological and ecological observations in order to understand the complexity of semiarid basins. Better observations lead to better calibration and better predictions. In addition, we need to upgrade our soil sampling and topographic survey in the area. We recognize the power of developing models for the estimation of subsurface topography. However, the results of soil thickness in this work could be robust and more sampling is required, especially in the approaches that relay on the relation between curvature and soil thickness.

REFERENCES

Adams, D., Comrie, A. (1997). The North American Monsoon. *Bulletin of the American Meteorological Society*, 78: 2197-2213.

Andersen,J., Dybkjaer, G., Jensen, K.H. , Refsgaard, J.C., Rasmussen, K. (2002). Use of remotely sensed precipitation and leaf area index in a distributed hydrological model, Journal of Hydrology, 264(1–4): 34-50

Andre, F., Jonard, M., Ponette, Q. (2008). Precipitation water storage capacity in temperate mixed Oak-Beech canopy. *Hydrological Processes,* 22: 4130-4141.

Apan, A., Kelly, R., Jensen, T., Butler, D., Strong, W., Basnet, B. (2002). Spectral discrimination of agricultural crops and soil moisture attributes using ASTER imagery. 11th ARSPC. Brisbane, Australia.

Arora, V. (2002). Modeling vegetation as a dynamic component in soil-vegetation-atmosphere transfer schemes and hydrological models. *Reviews of Geophysics*, 40(2): 1-26.

Baldocchi, D.D., Law, B.E., Anthoni, P.M. (2000). On measuring and modeling energy fluxes above the floor of a homogeneous and heterogeneous conifer forest. *Agricultural and Forest Meteorology*, 102: 187-206.

Baldocchi, D.D., Xu, L. (2007). What limits evaporation from Mediterranean oak woodlands: The supply of moisture in the soil, physiological control by plants or the demand by the atmosphere? *Advances in Water Resources*, 30: 2113-2122.

Batjes, N.H. (2009). Harmonized soil profile data for applications at global and continental scales: Updates to the WISE database. *Soil Use and Management,* 25: 124-127.

Bertoldi, G., R. Rigon, and T. M. Over, (2006). Impact of watershed geomorphic characteristics on the energy and water budgets. *Journal of Hydrometeorology*, 7**,** 389–403.

Beven K. J., Kirby, M.J. (1979). A physically based variable contributing area model of basin hydrology , *Hydrological Sciences. Bulletin*, 24:43-69.

Bindlish, R., Jackson, T.J., Gasiewski, A.J., Stankov, B., Cosh, M.H., Mladenova, I., Vivoni, E.R., Lakshmi, V., Watts, C.J., Keefer, T. (2008). Aircraft-based soil moisture retrievals in mixed vegetation and topographic conditions. *Remote Sensing of Environment*, 112: 375-390.

Boegh, R.N. Poulsen, M. Butts, P. Abrahamsen, E. Dellwik, S. Hansen, C.B. Hasager, A. Ibrom, J.-K. Loerup, K. Pilegaard, H. Soegaard, (2009). Remote sensing based evapotranspiration and runoff modeling of agricultural, forest and urban flux sites in Denmark: From field to macro-scale, Journal of Hydrology, 377(3–4): 300-316.

Blake, G.R. (1965). Bulk density, Methods of Soil Analysis, part 1, American Society of Agronomy.

Brito-Castillo, L., Douglas, A. V., Leyva-Contreras, A. and Lluch-Belda, D. (2003), The effect of large-scale circulation on precipitation and streamflow in the Gulf of California continental watershed. *International Journal of Climatology*, 23: 751–768. doi: 10.1002/joc.913.

Brown, D. (1994). *Biotic Communities: Southwestern United States and Northwestern Mexico.* University of Utah Press. 315 pages.

Brunsell, N.A. (2006). Characterization of land surface precipitation feedback regimes with remote sensing. *Remote sensing of Environment*, 100, 200-211.

Campbell Scientific, Inc. (2012). *Soil heat flux plate model HFP01. Instruction manual.* 18 pp.

Carleton, A.M. (1986). Sypoptic-dynamic character of bursts and break in the southwest U.S. summer precipitation singularity. Journal of Climatology, 6, 605-623.

Carlson, T.N., Ripley, D.A. (1997). On the relation between NDVI, fractional vegetation cover, and leaf area index. *Remote Sensing of Environment*, 62: 241-252.

Carlyle-Moses, D.E., Price, A.G. (2007). Modeling canopy interception loss from a Madrean pine-oak stand, Northeastern Mexico. *Hydrological Processes*, 21: 2572-2580.

Catani, F., Segoni, S., Falorni, G. (2010). An empirical geomorphology-based approach to the spatial prediction of soil thickness at catchment scale, *Water Resources Research*, 46:W05508.

Cavanaugh, M., Kurc, S., Scott, R.L. (2011). Evapotranspiration partitioning in semiarid shrubland ecosystems: a two-site evaluation of soil moisture control on transpiration. *Ecohydrology*, 4: 671-681.

Clapp, R., Hornberger, M.G. (1978). Empirical equations for some hydraulic properties. Water Resources Research, 14:4, 601-604.

Cleugh, H.A., Leuning, R., Mu, Q., Running, S.W. (2007). Regional evaporation estimates from flux tower and MODIS satellite data. *Remote Sensing of Environment*, 106: 285-304.

Cosgrove, B., Lohmann, D., Mitchell, K.E., Houser, P.R., Wood, E., Schaake, J.C., Robock, A., Marshall, C., Sheffield, J., Duan, Q., Luo, L., Higgins, R.W., Pinker, R., Tarpley, J.D., Meng, J. (2003). Real-time and retrospective forcing in the North American Land Data Assimilation System (NLDAS) project. Journal of Geophysical Research, 108:D22, 8842.

Deardorff, J.W. (1978). Efficient prediction of ground surface temperature and moisture with inclusion of a layer of vegetation. *Journal of Geophysical Research*, 82: 1889-1903.

Descroix, L., Nouvelot, J.F., Vauclin, M. (2002). Evaluation of an antecedent precipitation index to model runoff yield in the western Sierra Madre (North-west Mexico). Journal of Hydrology, 263: 114-130.

Dickinson, W. (2002). The Basin and range province as a composite extensional domain. International Geology Review, 44: 1-38.

Dietrich, W., D. Bellugi, L. Sklar, J. Stock, A. Heimsath, and J. Roering (2003), Geomorphic transport laws for predicting landscape forms and dynamics, in *Prediction in Geomorphology,* Geophysical. Monograph Series, vol. 135, pp. 103–132, doi:10.1029/135GM09.

Dirmeyer, Paul A., Randal D. Koster, Zhichang Guo, (2006). Do Global Models Properly Represent the Feedback between Land and Atmosphere?. Journal of Hydrometeorology, 7, 1177–1198.

Dominguez, F., Kumar, P., Vivoni, E.R. (2008). Precipitation recycling and ecoclimatological stability. A study using NARR data. Part II: North American monsoon region. Journal of Climate. 21: 5187-5203.

Douglas, W.M., Maddox, A.R., Howard, K., Reyes, S. (1993). The Mexican monsoon. *Journal of Climate,* 6: 1665-1677.

Dorman, J.L., Sellers, P.J. (1989). A global climatology of albedo, roughness length and stomatal resistance for atmospheric general circulation models as represented by Simple Biosphere Model (SiB). *Journal of Applied Meteorology*, 28: 833-855.

Douglas, W.M., Maddox, A.R., Howard, K., Reyes, S. (1993). The Mexican monsoon. Journal of Climate, 6: 1665-1677.

Droogers, P. and Kite, G. (2002), Remotely sensed data used for modelling at different hydrological scales. Hydrological Processes, 16: 1543–1556. doi: 10.1002/hyp.1019.

Dunne, T. and Black, R. D. (1970). An experimental investigation of runoff production in permeable soils, Water Resources Research, 6(2), 478– 490.

English, N.B., Weltzin, J.F., Fravolini, A., Thomas, L., Williams, D.G. (2005). The influence of soil texture and vegetation on soil moisture under rainout shelters in a semidesert grassland. *Journal of Arid Environments*, 63:324-343.

Eltahir, E.A.B., Bras, R.L. (1993). A description of rainfall interception over large areas. *Journal of Climate*, 6: 1002-1008.

Eltahir, E.A.B. (1998). A soil moisture-rainfall feedback mechanism: 1. Theory and observations. Water Resources Research, 34(4): 765-776.

Feddes, R.A., Kowalik, P.J., Zaradny, H. (1978). *Simulation of Field Water Use and Crop Yield*. John Wiley, New York, NY, 188 pp.

Fensholt, R., Sanholt, I., Schultz, M. (2004). Evaluation of MODIS LAI, fAPAR and the relation between fAPAR and NDVI in a semiarid environment using in situ measurements. *Remote Sensing of Environment*, 91: 490-507.

Frank, J., Massman, W., Ewers, B. (2013). Underestimates of sensible heat flux due to vertical velocity measurement errors in non-orthogonal sonic anemometers. *Agricultural and Forest Meteorology*, 171-172: 72-81.

Forzieri, G., Castelli, F., Vivoni, E.R. (2011). Vegetation dynamics within the North American Monsoon Region. Journal of Climate. 24(6): 1763-1783.

Freeze, R.A., Cherry, J.A. (1979), Groundwater, Prentice Hall. Pp: 35-52.

Gebremichael, M., Vivoni, E.R., Watts, C.J. and Rodríguez, J.C. (2007). Sub-mesoscale spatiotemporal variability of North American monsoon rainfall over complex terrain. *Journal of Climate*, 20(9): 1751-1773.

Gee, G. W., Bauder, J. W. (1986). Particle-size Analysis, in: Methods of Soil Analysis, Part 1. Soil Science Society of America. Book Series 5, 2nd edition., Madison, pp. 383–411.

Gessler P.E., Moore, I.D., McKenzie, N.J., Ryan, P. 1995. Soil-landscape modeling and spatial prediction of soil attributes, *International Journal of Geographical Information Systems*, 9(4): 421-432.

Gochis, D.J., Brito-Castillo, L., Shuttleworth, W.J. (2006). Hydroclimatology of the North American Monsoon region in northwest Mexico. Journal of Hydrology, 316: 53-70.

Gochis, D.J., Vivoni, E.R., Watts, C. (2010). The impact of soil depth on land surface energy and water fluxes in the North American Monsoon region, *Journal of Arid Environments*, 74: 564-571.

Gutzler, D.S. (2004). An index of interannual precipitation variability in the core of the North American monsoon region. *Journal of Climate*, 17: 4473-4480.

Heimsath, A.M., Dietrich, W.E., Nishiizumi, K., Finkel, R.C. (1999). Cosmogenic nuclides, topography, and the spatial variation of soil depth: *Geomorphology*, 27: 151-172.

Higgins, R.W., Shi, W. (2001). Intercomparison of the principal modes of interanual and intraseasonal variability of the North American monsoon system. *Journal of Climate*, 14: 403-417.

Horton, R. E. (1933). The role of infiltration in the hydrological cycle, Trans. AGU, 14, 446–460.

Hursh, C. R. and Brater, E. F. (1941). Separating storm-hydrographs form small drainage-areas into surface and subsurface flow, Trans. AGU, 22, 863–870.

Huxman, T.E., Cable, J.M., Ignace, D.D., Eilts, A.J., English, N.B., Weltzin, J., Williams, D.G., (2004). Response of net ecosystem gas exchange to a simulated precipitation pulse in a semi-arid grassland: the role of native and non-native grasses and soil texture. *Oecologia* 141, 295–305.

Irmak, S., Mutiibwa, D., Irmak, A., Arkebauer, T.J., Weiss, A., Martin, D.L., Eisenhauer, D.E. (2008). On the scaling up leaf stomatal resistance to canopy resistance using photosynthetic photon flux density. *Agricultural and Forest Meteorology*, 148: 1034-1044.

Ivanov, V.Y., Vivoni, E.R., Bras, R.L., Entekhabi, D. (2004). Catchment hydrologic response with a fully distributed triangulated irregular network model. *Water Resources Research*, 40: W11102, doi: 10.1029/2004WR003218.

Ivanov, V.Y., Bras, R.L., Vivoni, E.R. (2008). Vegetation-hydrology dynamics in complex terrain of semiarid areas. I. A mechanistic approach to modeling dynamic feedbacks. *Water Resources Research*, 44: W03429, doi:10.1029/2006WR005588.

Jasechko, S., Sharp, Z., Gibson, J., Birks, S.J., Fawcett, P. (2013). Terrestrial water fluxes dominated by transpiration**,** Nature, 496: 347–350. doi:10.1038/nature11983.

Jenson, K.S., Domingue,J.O.(1988). Extracting topographic structure from digital elevation data for geographic information system analysis. photogrammetric engineering and remote sensing, 54(11):1593-1600.

Kochendorfer, J., Meyers, T.P., Frank, J., Massman, W.J., Heuer, M.W. (2012). How well can we measure the vertical wind speed? Implications for fluxes of energy and mass. *Boundary Layer Meteorology,* 145(2): 383-398.

Kustas, W.P., Prueger, J.H., Hatfield, J.L., Ramalingam, K., Hipps, L.E. (2000). Variability in soil heat flux from a mesquite dune site. *Agricultural and Forest Meteorology*, 103: 249-264.

Lanni, C., McDonnell, J., Hopp, L. and Rigon, R. (2013), Simulated effect of soil depth and bedrock topography on near-surface hydrologic response and slope stability. Earth Surf. Process. Landforms, 38: 146–159. doi: 10.1002/esp.3267.

Lapham, W.W. (1989). Use of temperature profiles beneath streams to determine rates of vertical groundwater flow and vertical hydraulic conductivity. *USGS Water Supply Paper 2337*, 1-35.

Lawrence, D., Thornton, P., Oleson, K., Bonan, G. (2007). The partition of evapotranspiration into transpiration, soil evaporation, and canopy evaporation in GCM: Impacts on land-atmosphere interactions. *Journal of Hydrometeorology*, 8: 862-880.

Lee, X., Finnigan, J., Paw U, K.T. (2004). Coordinate systems and flux bias error. In: *Handbook of Micrometeorology: A Guide for Surface Flux Measurements*, eds. Lee, X., Massman, W.J., Law, B.E. Dordrecht, The Netherlands: Kluwer Academic, pp. 33-66.

Liao, K., Xu, S., Wu, J., Zhu, Q. (2014). Spatial estimation of surface soil texture using remote sensing data. Soil Science and Plant Nutrition. 59:4, 488-500.

Liebmann, B., Blade, I., Bond, N., Gochis, D., Allured, D., Bates, G.T. (2008). Characteristics of North American summertime rainfall with emphasis on the monsoon. Journal of Climate. 21: 1277-1294.

Lizárraga-Celaya, C., Watts, C.J., Rodríguez, J.C., Garatuza- Payán, J., Scott, R.L., Sáiz-Hernández, J.A. (2010). Spatio-temporal variations in surface characteristics over the North American monsoon region. *Journal of Arid Environments*, 74: 540-548.

Maass, J.M., Vose, J.M., Swankb, W., Martinez-Yrizar, A. (1995). Seasonal changes of leaf area index (LAI) in a tropical deciduous forest in west Mexico. *Forest Ecology and Management*, 74: 171-180.

Mahfouf, J.-F., Ciret, C., Ducharne, A., Irannejad, P., Noilhan, J., Shao, Y., Thorton, P., Xue, Y., Yang, Z.-L. (1996). Analysis of transpiration results from the RICE and PILPS Workshop. *Global and Planetary Change*, 13: 73-88.

Mascaro, G., Vivoni, E.R., Gochis, D.J., Watts, C.J. and Rodriguez, J.C. (2014). Temporal Downscaling and Statistical Analysis of Rainfall across a Topographic Transect in Northwest Mexico. Journal of Applied Meteorology and Climatology. 53(4): 910-927.

Massman, W.J., Lee, X. (2002). Eddy covariance flux corrections and uncertainties in long-term studies of carbon and energy exchanges. *Agricultural and Forest Meteorology*, 113: 121-144.

Matsui, T., Lakshmi, V., Small, E.E. (2005). The effects of satellite derived vegetation cover variability on simulated land-atmosphere interactions in the NAMS. *Journal of Climate*, 18: 21-40.

Mauder, M., Foken, T. (2004). *Documentation and instruction manual of the eddy covariance software package TK2*. Universität Bayreuth, Abt. Mikrometeorologie, 26, 44 pp.

Meek, D.W., Hatfield., J.L., Howell, T.A., Idso, S.B., Reginato, R.J. (1984). A generalized relationship between photosynthetically active radiation and solar radiation, *Agronomy Journal*, 76: 939-945.

Méndez-Barroso, L.A., Vivoni, E.R., Watts, C.J., Rodríguez, J.C. (2009). Seasonal and interannual relations between precipitation, soil moisture and vegetation dynamics in the North American monsoon region. *Journal of Hydrology*, 377: 59-70.

Méndez-Barroso, L.A., Vivoni, E.R. (2010). Observed shift in land surface conditions during the North American monsoon: Implications for a vegetation-rainfall feedback mechanism. *Journal of Arid Environments*, 74: 549-555.

Méndez-Barroso, L.A., Vivoni, E.R., Robles-Morúa, A., Mascaro, G., Yépez, E.A., Rodriguez, J.C., Watts, C.J., Garatuza-Payan, J., Saiz-Hernandez, J.A. (2014). A modeling approach reveals differences in evapotranspiration and its partitioning in two semiarid ecosystems in Northwest Mexico. Water Resources Research, 50, doi:10.1002/2013WR014838.

Mielnick, P., Dugas, D.A., Mitchell, K., Havstad, K. (2005). Long-term measurements of CO_2 flux and evapotranspiration in a Chihuahuan desert grassland. *Journal of Arid Environments*, 60: 423-436.

Mitchell, K.E., and coauthors. (2004). The multi-institution North American Land Data Assimilation System (NLDAS): Utilizing multiple GCIP products and partners in a continental distributed hydrological modeling system. *Journal of Geophysical Research*, 109: D07S90, doi:10.1029/2003JD003823.

Moncrieff, J.B., Jarvis, P.G., Valentini, R. (2000). Canopy fluxes. In: *Methods in Ecosystem Science* (Sala, O.E., Jackson, R.B., Mooney, H.A., Howarth, R.W. eds. Springer-Verlag, New York, NY, pp. 161-181.

Moore, I.D., Gessler, P.E., Nielsen, G.A. Petersen, G.A. (1993). Soil attribute prediction using terrain analysis, *Soil Science Society of America Journal*, 57: 443-452.

Moran, M.S., Scott, R.L., Keefer, T.O., Emmerich, W.E., Hernandez, M., Nearing, G.S., Paige, G.B., Cosh., M.H., O'Neill, P.E. (2009). Partitioning evapotranspiration in semiarid grassland and shrubland ecosystems using time series of soil surface temperature. *Agricultural and Forest Meteorology*, 149: 59-72.

Návar, J., Synnott, T. (2000). Surface runoff, soil erosion and land use in northeastern Mexico. TERRA Latinoamericana. 18:3, 247-253.

Newman, B.D., Wilcox, B.P., Archer, S., Breshears, D.D., Dahm, C.N., Duffy, C.J., McDowell, N.G., Phillips, F.M., Scanlon, B.R., Vivoni, E.R. (2006). The ecohydrology of arid and semiarid environments: A scientific vision. *Water Resources Research*, 42: W06302, doi:10.1029/2005WR004141.

Nicótina, L., D. G. Tarboton, T. K. Tesfa, and A. Rinaldo (2011), Hydrologic controls on equilibrium soil depths, Water Resources Research, 47, W04517, doi:10.1029/2010WR009538.

Noy-Meir, I. (1973). Desert Ecosystems: Environment and Producers. Annual Review of Ecology and Systematics, 4: 25-51.

Notaro, M., Gutzler, D. (2012). Simulated impact of vegetation on climate across the North American Monsoon region in CCSM3.5. Climate Dynamics, 38: 795-814.

Oleson, K. W., and Coauthors, (2004). Technical description of the community land model (CLM). NCAR Tech. Note NCAR/TN-461+STR, 186 pp.

Peel, M.C., Finlayson, B.L, McMahon, T.A. (2007). Updated world map of the Köppen-Geiger climate classification. *Hydrology and Earth System Science,* 11: 1633-1644.

Pelletier, J. D., and C. Rasmussen (2009), Geomorphically based predictive mapping of soil thickness in upland watersheds, Water Resources Research, 45, W09417, doi:10.1029/2008WR007319.

Pereira, F.L., Gash, J.H.C., David, J.S., David, T.S., Monteiro, P.R., Valente, F. (2009). Modelling interception loss from evergreen oak Mediterranean savannas: Application of a tree-based modelling approach. *Agricultural and Forest Meteorology*, 149(3-4): 680-688.

Perevochtchikova M. (2009). Retos de la información del agua en Mexico para una mejor gestión. Realidad, datos y espacio: Revista internacional de estadística y geografía. 4(1): 42-57.

Perevochtchikova M. (2011). El Uso del dato obtenido del monitoreo hidroclimatologico: el caso de la cuenca del valle de Mexico en: Oswald,U. Retos de la Investigacion del agua en Mexico, Mexico, CRIM-UNAM: 77-87.

Pitman, J.I. (1989). Rainfall interception by bracken in open habitats relations between leaf area, canopy storage and drainage rate. *Journal of Hydrology*, 105: 317-334.

Privette, J.L., Myneni, R.B., Knyazikhin, Y., Mukelabai, M., Roberts, G. (2002). Early spatial and temporal validation of MODIS LAI product in the Southern Africa Kalahari. *Remote Sensing of Environment*, 83: 232-243.

Rawls, W.J, Brakensiek, D.L. (1989) Estimation of soil water retention and hydraulic properties In: *Unsaturated Flow in Hydrologic Modeling: Theory and Practice*, Kluwer Academic Publishing, Dordrecht, pp. 275-300.

Rawls, W.J., Brakensiek, D.L., Miller, N. (1983). Green-Ampt infiltration parameters from soils data. *Journal of Hydraulic Engineering*, 109(1): 62-70.

Raz-Yaseef, N., Yakir, D., Schiller, G., Cohen, S. (2012). Dynamics of evapotranspiration partitioning in a semi-arid forest as affected by temporal rainfall patterns. *Agricultural and Forest Meteorology*, 157: 77-85.

Reynolds, J.F., Kemp, P.R., Tenhunen, J.D. (2000) Effects of long-term rainfall variability on evapotranspiration and soil water distribution in the Chihuahuan Desert: A modeling analysis. *Plant Ecology*, 150: 145-159.

Richardson A.D., Keenan, T., Migliavacca, M., Ryu, Y., Sonnentag, O., Toomey, M. (2013). Climate change, Phenology and phenological control of vegetation feedbacks to the climate system. Agricultural and Forest Meteorology 169: 156-173.

Robles-Morúa, A., Vivoni, E.R., Mayer, A. (2012). Distributed hydrologic modeling in Northwest Mexico reveals the links between runoff mechanisms and evapotranspiration. Journal of Hydrometeorology, 13: 785-807.

Robles-Morúa, A., Che, D., Mayer, A.S., and Vivoni, E.R. (2014). Hydrologic Assessment of Proposed Reservoirs in the Sonora River Basin, Mexico, under Historical and Future Climate Scenarios*Hydrological Sciences Journal*. (In Press). DOI:10.1080/02626667.2013.878462.

Rodriguez-Iturbe, I., A. Porporato, L. Ridolfi, V. Isham, and D. Cox (1999), Probabilistic modelling of water balance at a point: The role of climate soil and vegetation, *Proc. R. Soc. London, Ser. A, 455,* 3789 – 3805.

Rodríguez-Iturbe, I., Porporato, A., Laio, F., Ridolfi, L. (2001). Intensive versus extensive use of soil moisture: plant strategies to cope with stochastic water availability. *Geophysical Research Letters*, 28: 4495-4497.

Rutter, A.J., Kershaw, K.A., Robins, P.C., Morton, A.J. (1971). A predictive model of rainfall interception in forests: 1. Derivation of the model from observation in a plantation of Corsican pine. *Agricultural Meteorology*, 9: 367-384.

Ryu D., Jackson, T.J., Bindlish, R., Le Vine D.M., Hacken, M. (2010). Soil moisture retrieval using a two-dimensional L-band synthetic aperture radiometer in a semiarid environment. IEEE Transactions on Geoscience and Remote Sensing, 48(12): 4273-4283.

Ryu, Y., Verfaille, J., Macfarlane, C., Kobayashi, H., Sonnentag, O., Vargas, R., Ma, S., Baldocchi, D. (2012). Continuous observations of tree leaf area index at ecosystem scale using upward-pointing digital cameras. *Remote Sensing of Environment*, 126: 115-125.

Saulnier, G.M., Beven, K., Obled, C. (1997). Including spatially variable effective soil depths in TOPMODEL. *Journal of Hydrology,* 202: 158-172.

Sala, O.E., Parton, W.J. Lauenroth, W.K. Joyce, L.A. (1988). Primary production of the central grasslands region of the United States. *Ecology*, 69: 40-45.

Savenije, H.H.G. (1996).The runoff coefficient as the key to moisture recycling. Journal of Hydrology, 176: 219-225. doi:10.1016/0022-1694(95)02776-9.

Saxton, K.E., Rawls, W.J. (2006). Soil water characteristics estimates by texture and organic matter for hydrologic solutions. Soil Science Society of America Journal, 70: 1569-1578.

Sellers, P.J., Randall, D.A., Collatz, G.J., Berry, J.A., Field, C.B., Dazlich, D.A., Zhang, C., Collelo, G.D., Bounoua, L. (1996) A revised land surface parameterization (SiB2) for atmospheric GCMs. Part 1: Model formulation, Journal of Climate, 9: 676-705.

Schaap, M.G., Shouse, P.J., Meyer, P.D. (2003). Laboratory measurements of the unsaturated hydraulic properties at the vadose zone transport field study. Pacific Northwest National Laboratory. Report #PNNL-14284, Richland, WA, 73 pp.

Schulze, E.D., Leuning, R., Kelliher, F.M. (1995). Environmental regulation of surface conductance for evaporation from vegetation, *Vegetatio*, 121: 79-87.

Scott, R.L., Edwards, E.A., Shuttleworth, W.J., Huxman, T.E., Watts, C.J., Goodrich, D.C. (2004). Interannual and seasonal variations in fluxes of water and carbon dioxide from a riparian woodland ecosystem. *Agricultural and Forest Meteorology,* 122: 64-84.

Scott, R.L., Huxman, T.E., Cable, W.L., Emmerich, W.E. (2006). Partitioning of evapotranspiration and its relation to carbon dioxide exchange in a Chihuahuan desert shrubland. *Hydrological Processes*, 20: 3227-3243.

Seyfried, M.S., Murdock, M.D. (2004). Measurement of soil water content with a 50-MHz soil dielectric sensor. *Soil Science Society of America Journal*, 68: 394-403.

Shuttleworth, W.J. (1992). Evaporation. In *Handbook of Hydrology*, edited by D. R. Maidment, pp. 4.11 – 4.18, McGraw-Hill, New York, NY.

Stannard, D.I., Weltz, M.A. (2006). Partitioning evapotranspiration in sparsely vegetated rangeland using a portable chamber. *Water Resources Research*, 42: W02413, doi:10.1029/2005WR004251.

Sugiyama, S., Yoneyama, M., Takahashi, N., Gotoh, K. (1985). Canopy structure and productivity of Festuca arundinacea Schreb. during vegetative and reproductive growth. *Grass Forage Science*, 40: 49-55.

Sullivan, D.G., Shaw, N.J., Rickman, D. (2005). IKONOS imagery to estimate surface soil property variability in two Alabama Physiographies, *Soil Science Society of America Journal*, 69: 1789-1798.

Sutanto, S. J., Wenninger, J., Coenders-Gerrits, A. M. J., and Uhlenbrook, S. (2012). Partitioning of evaporation into transpiration, soil evaporation and interception: a comparison between isotope measurements and a HYDRUS-1D model, Hydrology and Earth System Science, 16, 2605-2616, doi:10.5194/hess-16-2605-2012.

Tang, Q., Vivoni, E.R., Munoz-Arriola, F. and Lettenmaier, D.P. (2012). Predictability of evapotranspiration patterns using remotely-sensed vegetation dynamics during the North American monsoon. *Journal of Hydrometeorology*, 13: 103-121.

Tarboton, D. G., (2003), Terrain Analysis Using Digital Elevation Models in Hydrology, 23rd ESRI International Users Conference, San Diego, California, July 7-11.

Tarín, T.T., Yépez, E.A., Garatuza-Payán, J., Watts, C.J., Rodríguez, J.C., Vivoni, E.R., Méndez-Barroso, L.A. (2014). Evapotranspiration partitioning with stable isotopes in ecohydrological studies. *Water Technology and Sciences*, 5(3): (In Press).

Tromp-van Meerveld, H.J., McDonnell, J.J. (2006). On the interrelations between topography, soil depth, soil moisture, transpiration rates and species distribution at the hillslope scale, Advances in Water Resources, 29(2): 293-310.

Unland, H., Houser, P.R., Shuttleworth, J.W/, Yang, Z.L. (1996). Surface flux measurement and modeling at a semi-arid Sonoran Desert site, Agricultural and Forest Meteorology, 82(1-4):119-153.

Van den Hurk, B.J.J.M., Viterbo, P., Los, S.O. (2003). Impact of leaf area index seasonality on the annual land surface evaporation in a global circulation model. *Journal of Geophysical Research*, 108(D6): 4191.

Van Genuchten, M.T. (1980). Predicting the hydraulic conductivity of unsaturated soil. *Soil Science Society of America Journal*, 44: 892-898.

Vargas, R., Yépez, E.A., Andrade, J.L., Angeles, G., Arredondo, T., Castellanos, A.E., Delgado, J., Garatuza-Payán, J., Gonzalez del Castillo, E., Oechel, W., Sanchez-Azofeifa, A., Velasco, E., Vivoni, E.R., Watts, C.J. (2013). Progress and opportunities for monitoring greenhouse gases fluxes in Mexican ecosystems: The MexFlux Network. *Atmósfera*, 26(3): 325-336.

Viramontes, D. and Descroix, L. (2003), Changes in the surface water hydrologic characteristics of an endoreic basin of northern Mexico from 1970 to 1998. Hydrological Processes, 17: 1291–1306. doi: 10.1002/hyp.1285.

Vivoni, E.R., Entekhabi, D., Bras, R.L., Ivanov, V.Y. (2007a). Controls on runoff generation and scale-dependence in a distributed hydrologic model. *Hydrology and Earth System Sciences*, 11(5): 1683-1701.

Vivoni, E.R., Gutiérrez-Jurado, H.A., Aragón, C.A., Méndez-Barroso, L.A., Rinehart, A.J., Wyckoff, R.L., Rodríguez, J.C., Watts, C.J., Bolten, J.D., Lakshmi, V., Jackson, T.J. (2007b). Variation of hydrometeorological conditions along a topographic transect in northwestern Mexico during the North American monsoon. *Journal of Climate*, 20(9): 1792-1809.

Vivoni, E.R., Entekhabi, D., Bras, R.L., Ivanov, V.Y. (2007c). Controls on runoff generation and scale-dependence in a distributed hydrologic model, Hydrology and Earth System Sciences, 11: 1683-1701.

Vivoni, E.R., Moreno, H.A., Mascaro, G., Rodríguez, J.C., Watts, C.J., Garatuza-Payán, J., Scott, R.L. (2008). Observed relation between evapotranspiration and soil moisture in the North American monsoon region. *Geophysical Research Letters*, 35: L22403, doi: 10.1029/2008GL036001.

Vivoni, E.R., Rodríguez, J.C., Watts, C.J. (2010). On the spatiotemporal variability of soil moisture and evapotranspiration in a mountainous basin within the North American monsoon region. *Water Resources Research*, 46: W02509, doi:10.1029/2009WR008240.

Vivoni, E.R., Mascaro, G., Mniszewski, S., Fasel, P., Springer, E.P., Ivanov, V.Y., Bras, R.L. (2011). Real-world hydrologic assessment of a fully-distributed hydrological model in a parallel computing environment. Journal of Hydrology, 409: 483-496.

Vivoni, E.R. (2012). Diagnosing seasonal vegetation impacts on evapotranspiration and its partitioning at the catchment scale during SMEX04-NAME. *Journal of Hydrometeorology*, 13: 1631-1638.

Wagener T, Sivapalan M, Troch PA, McGlynn BL, Harman CJ, Gupta HV, Kumar P, Rao SC, Basu NB, Wilson JS. (2010). The future of hydrology: an evolving science for a changing world. Water Resources Research 46: 1–10.

Watts, C.J., Scott, R.L., Garatuza-Payán, J., Rodríguez, J.C., Prueger, J.H., Kustas, W.P., Douglas, M. (2007). Changes in vegetation condition and surface fluxes during NAME 2004. *Journal of Climate*, 20: 1810-1820.

Webb, E.K., Pearman, G.I., Leuning, R. (1980). Correction of flux measurements for density effects due to heat and water vapour transfer. *Quarterly Journal of Royal Meteorology Society*, 106: 85-100.

Weiler, M., McDonnell, J.J. (2006). Testing nutrient flushing hypotheses at the hillslope scale: A virtual experiment approach, Journal of Hydrology, 319(1–4): 339-356.

Weyman, D. R. (1970). Throughflow on hillslopes and its relation to the stream hydrograph, Hydrological Science Bulletin, 15, 25–33.

Wigmosta, M.S., Vail, L., Lettenmaier, D.P. (1994). A distributed hydrology-vegetation model for complex terrain. *Water Resources Research*, 30: 1665-1679.

Wilcox, B. P., and Y. Huang (2010), Woody plant encroachment paradox: Rivers rebound as degraded grasslands convert to woodlands, Geophys. Res. Lett., 37, L07402, doi:10.1029/2009/GL041929.

Wilczak, J.M., Oncley, S.P., Stage, S.A. (2001). Sonic anemometer tilt correction algorithms. *Boundary-Layer Meteorology*, 99: 127-150.

Wilson, K., Goldstein, A., Falge, E., Aubinet, M., Baldocchi, D. (2002). Energy balance closure at FLUXNET sites. *Agricultural and Forest Meteorology*, 113: 223-243.

Wilson, J.L., Guan. H. (2004). Mountain-block hydrology and mountain front recharge. In Groundwater recharge in a desert environment: The southwestern United States. Water Science and Applications 9. American Geophysical Union, Washington, DC, pp. 113-137.

Xiang, T., Vivoni, E.R., Gochis, D.J. (2014). Seasonal evolution of ecohydrological controls on land surface temperature over complex terrain. Water Resources Research, 50: 3852-3874.doi:/10.1002/2013WR014787.

Yan, H., Wang, S.Q., Billesbach, D., Oechel, W., Zhang, J.H., Meyers, T., Martin, T.A., Matamala, R., Baldocchi, D., Bohrer, G., Dragoni, D., Scott, R.L. (2012). Global estimation of evapotranspiration using a leaf area index-based surface energy and water balance model. *Remote Sensing of Environment*, 124: 581-595.

Yang, Y., Scott, R.L., Shang, S. (2013). Modeling evaporation and its partitioning over a semiarid shrub ecosystem from satellite imagery: A multiple validation. *Journal of Applied Remote Sensing*, 7: 073495, doi:10.1117/1.JRS.7.073495.

Yépez, E.A., Williams, D., Scott, R., Lin, G. (2003). Partitioning overstory and understory evapotranspiration in a semiarid savanna woodland from the isotopic composition of water vapor. *Agricultural and Forest Meteorology*, 119: 53-68.

Yépez, E., Scott, R., Cable, W., Williams, D. (2007). Intraseasonal variation in water and carbon dioxide flux components in a semiarid riparian woodland. *Ecosystems*, 10: 1100-1115.

Yilmaz, M.T., Hunt, E.R., Goins, D.L., Ustin, S.L., Vanderbilt, V.C., Jackson, T.J. (2008). Vegetation water content during SMEX04 form ground data and Landsat 5 Thematic Mapper imagery. *Remote Sensing of Environment,* 112:350-362.

Zalewski, M. (2000). Ecohydrology—the scientific background to use ecosystem properties as management tools toward sustainability of water resources. Ecological engineering 16(1): 1-8.

Zhang, R., Warrick A.W., Myers, D.E. (1992). Improvement of the prediction of soil particle size fractions using spectral properties, *Geoderma*, 52:223-234.

APPENDIX A

EVAPOTRANSPIRATION PARTITION

Three evaporation components are estimated in tRIBS: (1) bare soil evaporation (*E*), (2) evaporation of canopy interception (*I*) and (3) plant transpiration (*T*). Total evapotranspiration (*ET* = *E* + *I* +*T*) is estimated in a stepwise fashion using the Penman-Monteith approach:

$$\lambda ET = \frac{\frac{\Delta}{\gamma}(R_n - G) + \frac{\rho m \lambda}{r_a}\delta q_a}{1 + \frac{\Delta}{\gamma} + \frac{r_s}{r_a}} \quad , \tag{A1}$$

where Δ is the slope of the Clausius-Clayperon relation, γ is the psychometric constant, λ is the latent heat of vaporization, R_n is the net radiation, G is the ground heat flux, ρ_m is the moist air density, δq_a is the specific humidity deficit and r_a and r_s are the aerodynamic and canopy stomatal resistances. r_a is estimated using wind speed observations and vegetation height (*h*) estimates under the assumption of a logarithmic velocity profile (Shuttleworth, 1992). In this study, the time-varying r_s is obtained from remotely-sensed measurements of LAI and fPAR (see Appendix C). Net radiation is impacted by the albedo (*a*) and optical transmission coefficient (k_t) that characterize the plant canopy or soil surface (Table 3).

Interception occurs as a fraction of rainfall, $(1\text{-}p)R$, where *p* is the free throughfall coefficient and *R* is rainfall. Evaporation of intercepted water on the canopy is fulfilled first in the stepwise calculations as (Eltahir and Bras, 1993):

$$I = \begin{cases} v_f E_p \; for \; C > S \\ \frac{C}{S} v_f E_p \; for \; C \leq S \end{cases} \quad , \tag{A2}$$

where *C* is the canopy storage volume, *S* is the maximum canopy storage (Table 3) and E_p is the potential evaporation rate that excludes the effect of canopy stomatal resistance obtained as:

$$E_p = ET \left[\frac{\Delta + \gamma (1 + {}^{r_s}/_{r_a}}{\Delta + \gamma} \right] \quad , \tag{A3}$$

The Rutter et al. (1971) approach to tracking the canopy water storage is utilized in the model.

Bare soil evaporation is then obtained for the bare soil fraction, independently of the plant transpiration, from the potential evaporation rate as (Deardorff, 1978):

$$E = (1 - v_f)\beta_s E_p \quad , \tag{A4}$$

where v_f is the vegetation fraction of a model element occupied by a plant functional type (i.e., tree or shrub) and represents the green vegetation cover that can be linked to NDVI (Appendix C), while 1-v_f represents the bare soil area, and β_S is a function of soil moisture as:

$$\beta_s = min\left(1, \frac{\theta_{Sur} - \theta_r}{\beta_E \theta_s - \theta_r}\right) \quad , \tag{A5}$$

where θ_{sur} is the surface soil moisture (top 10 cm), θ_s is the soil moisture at saturation, θ_r is the residual soil moisture and β_E is the soil evaporation stress factor (Tables 2 and 3). The form of A5 is commonly used in hydrologic models (see Feddes et al., 1978; Mahfouf et al., 1996). Plant transpiration (T) is calculated after accounting for the consumption of intercepted water by evaporation as:

$$T = \beta_R v_f (E_p - I)\left[\frac{\Delta + \gamma}{\Delta + \gamma(1 + r_s/r_a}\right] \quad , \tag{A6}$$

where β_R accounts for soil moisture stress that limits the plant water uptake as:

$$\beta_R = min\left(1, \frac{\theta_{root} - \theta_r}{\beta_T \theta_s - \theta_r}\right) \quad , \tag{A7}$$

where θ_{root} is the root zone moisture (top 1 m) and β_T is the plant transpiration stress factor. Thus, ET is composed of three components ($ET = E + I + T$) that depend on vegetation (v_f, r_s, p, S, β_E and β_T) and soil (θ_s and θ_r) properties, including soil moisture, as well as meteorological forcing, through a weighting based on the areal proportions of bare soil and vegetation. For additional information, the reader is referred to Wigmosta et al. (1994) and Ivanov et al. (2004).

APPENDIX B

STATISTICAL METRICS

Model performance is assessed using three metrics to compare observations (*O*) and simulations (*S*) of latent heat flux and soil moisture over the number of time steps (*N*) with available data. The Mean Absolute Error (MAE) describes the absolute differences between observations and simulations without emphasizing the value of outliers as:

$$MAE = \frac{1}{N}\sum_{i=1}^{N}|O_i - S_i| \quad , \qquad \text{(B1)}$$

The correlation coefficient (CC), which measures the linear relation between *S* and *O*, is:

$$CC = \frac{\sum_{i=1}^{N}(O_i - \overline{O})(S_i - \overline{S})}{\left[\sum_{i=1}^{N}(O_i - \overline{O})^2\right]^{0.5}\left[\sum_{i=1}^{N}(S_i - \overline{S})^2\right]^{0.5}} \quad , \qquad \text{(B2)}$$

where the overbar denotes a temporal mean value. CC varies from -1 (negative correlation) to 1 (positive correlation), with CC = 0 indicating no correlation. The dimensionless bias (B) is obtained as the ratio of temporal mean of the simulated and observed variables, as:

$$B = \frac{\overline{S}}{\overline{O}} \quad . \qquad \text{(B3)}$$

APPENDIX C

EMPIRICAL EQUATIONS TO ESTIMATE VEGETATION PARAMETERS

A set of empirical equations are used to link remote sensing data to vegetation parameters in tRIBS (Table 3). In each case, coefficient values were locally-calibrated by comparing the retrieved parameters to the range of values from available literature in similar ecosystems. Maximum canopy storage (*S*) controls rainfall interception as a function of time-varying LAI from MODIS. For both sites, we used the relation, $S = 0.5\text{LAI}$, from Pitman (1989) and Carlyle-Moses and Price (2007), with the coefficient verified with the datasets of Pitman (1989) for shrubs and Andre et al. (2008) for oaks. The free through fall coefficient (*p*) accounts for the fraction of rainfall not captured by plants. We relate *p* to time-varying LAI, following Pitman (1989), as:

$$p = \exp(-1.5LAI) \quad , \tag{C1}$$

The optical transmission coefficient (k_t) is obtained from the Beer-Lambert law as:

$$k_t = \exp(-kLAI) \quad , \tag{C2}$$

where $k = 0.61$ for ST (Maass et al., 1995) and $k = 0.31$ for MW (Sugiyama et al., 1985), based on differences in leaf architecture at the two sites. The minimum canopy stomatal resistance (r_s) was obtained using an energy-limited relation developed by Schulze et al. (1995) and up-scaled from an individual leaf to the canopy following Irmak et al. (2008):

$$r_s = \frac{\left[\frac{Q_{50}+Q}{g_{max}Q}\right]}{LAI} \quad , \tag{C3}$$

where g_{max} is the maximum seasonal stomatal conductance specified as 0.03 m/s for drought deciduous trees (Schulze et al., 1995) and assumed here to be constant in time and for different vegetation types. A diurnal cycle is prescribed for stomatal resistance such that the minimum value (r_s) occurs at noon. This relation does not account for atmospheric conditions that are treated separately in the evapotranspiration estimate (A1). Q_{50} is the value of the absorbed photosynthetically active radiation (*Q*) obtained when g_{max} is half of its value. *Q* is obtained as:

$$Q = 0.45 I_s fPAR \quad , \tag{C4}$$

where I_s the incoming shortwave radiation, fPAR is the fraction of Photosynthetically Active Radiation from MODIS and the coefficient 0.45 represents the fraction of I_s that is used by plants directly for photosynthesis (Meek et al., 1984). Minimum stomatal resistance values (r_s) for both sites were calibrated using the global estimates of Dorman and Sellers (1989). Vegetation fraction (v_f) was estimated following Carlson and Ripley (1997) as:

$$v_f = \left[\frac{NDVI - NDVI_{min}}{NDVI_{max} - NDVI_{min}}\right]^2 , \tag{C5}$$

where $NDVI_{min}$ and $NDVI_{max}$ are the minimum and maximum values of the time-varying NDVI obtained over the MODIS record (2004-2009) at each site. $NDVI_{min}$ and $NDVI_{max}$ represent the background signal from the soil during the driest period of the record and peak greenness during the wettest period of the record (Méndez-Barroso et al., 2009). In the model, the vegetated fraction carries out transpiration, while the 1-v_f fraction is considered to be bare soil and is subject to soil evaporation (Appendix A). Time-varying albedo (a) was obtained directly from MODIS. Other vegetation parameters, such as vegetation height (h), were kept constant in the simulations

APPENDIX D

ASTER IMAGE PROCESSING AND ESTIMATION OF DISTRIBUTED OF SOIL TEXTURE

The estimation of the spatial distribution of soil texture involves certain preprocessing of ASTER image such conversion of ASTER raw data or digital numbers (DN) into surface radiance. The digital number value of the ASTER image is multiplied by a conversion factor specific for every band according to the following equation:

$$Radiance = (DN - 1) * conversion\ factor \ , \qquad \text{(D1)}$$

The following table shows the conversion factors specific for every ASTER band. This conversion factor are specified in the metadata file of ASTER:

Table D.1 Characteristics and Conversion Factors of ASTER Bands

ASTER Band	Wavelength [μm]	Description	Conversion factor [W/m^2/sr⋆μm]
1	0.520–0.600	Visible, green-yellow	1.688
2	0.630–0.690	Visible, red	1.415
3	0.760–0.860	Near infrared	0.862
4	1.600–1.700	Short-wave infrared	0.2164
5	2.145–2.185	Short-wave infrared	0.0696
6	2.185–2.225	Short-wave infrared	0.0625
7	2.235–2.285	Short-wave infrared	0.0597
8	2.295–2.365	Short-wave infrared	0.0417
9	2.360–2.430	Short-wave infrared	0.0318
10	8.125–8.475	Thermal infrared	0.00682
11	8.475–8.825	Thermal infrared	0.00678
12	8.925–9.275	Thermal infrared	0.00659
13	10.250–10.950	Thermal infrared	0.00569
14	10.950–11.650	Thermal infrared	0.00522

Once ASTER digital number is converted in surface radiance, then radiance value in all bands are extracted at the location of the sampling sites for surface soil. Figure 3.1a shows the location of the sampling sites for the determination of surface soil textural properties. After pixel extraction, radiance values are sorted according to soil textural type. The following table shows the values of radiance in all ASTER bands sorted by soil textural type determined by the method of the pipette. For clarification, the table has the following nomenclature: X an Y represents the location of the sampling sites in Universal Transverse Mercator (UTM) projected coordinate system, zone 12 North with datum World Geodetic System 1984 (WGS84). Sample ID corresponds to two type of samples: Surface sample (S) and soil pits (P) follow by a number that indicates the number of sample according to map 3.1b. Texture type describes the soil texture of the sample found in Sierra Los Locos basin: The soil textural types found in this basin were: Loamy sand (LS), sand (S), sandy clay loam (SCL) and loamy sand (LS). Finally, the column header indicates the number of the ASTER band and the range in the electromagnetic spectrum, for example; V refers to the visible portion of the electromagnetic radiation whereas S and T represents the shortwave and thermal infrared regions respectively. Bold numbers at the end of every soil textural class are the mean and standard deviation calculated for every ASTER band.

Table D.2 ASTER Radiance Values for the Soil Textural Classes Found in Sierra Los Locos, Sonora, Mexico. Radiance Values Were Extracted at Sampling Sites.

X	Y	**ID**	**Texture**	**V1**	**V2**	**V3N**	**V3B**	**S4**	**S5**	**S6**	**S7**
549622	3315727	S6	LS	92.8	89.1	76.7	75.9	19.6	5.4	5.1	4.4
546031	3314637	S13	LS	82.7	73.6	63.8	61.2	17.0	4.9	4.6	4.0
544266	3314158	S17	LS	67.5	58.0	50.0	50.9	15.2	4.6	4.3	3.6
548501	3312681	S33	LS	79.3	72.2	65.5	62.1	19.8	5.5	5.3	4.5
551302	3316141	S36	LS	99.6	97.6	87.9	90.5	21.3	5.8	5.6	4.7
552194	3314095	S38	LS	87.8	82.1	77.6	75.0	21.5	5.7	5.7	4.8
539955	3310984	S43	LS	79.3	72.2	60.3	69.0	16.1	4.8	4.4	4.1
546045	3313803	P5_1	LS	79.3	72.2	65.5	64.7	17.2	4.8	4.6	3.9
546082	3312189	P7_1	LS	79.3	72.2	68.1	70.7	19.8	5.4	5.2	4.4
549357	3313609	P8_1	LS	81.0	72.2	68.1	69.0	18.9	5.3	5.1	4.4
-	-	**Mean**	**LS**	**82.88**	**76.13**	**68.36**	**68.87**	**18.63**	**5.23**	**4.98**	**4.29**
-	-	**Stdev**	**LS**	**8.77**	**10.96**	**10.42**	**10.57**	**2.16**	**0.41**	**0.48**	**0.37**
545281	3314524	S14	S	69.2	58.0	56.0	59.5	15.7	4.7	4.3	3.7
543757	3314003	S18	S	77.6	67.9	67.2	64.7	17.0	4.9	4.6	3.9
-	-	**Mean**	**S**	**73.43**	**62.97**	**61.63**	**62.06**	**16.31**	**4.80**	**4.41**	**3.82**
-	-	**Stdev**	**S**	**5.97**	**7.00**	**7.92**	**3.66**	**0.92**	**0.20**	**0.22**	**0.17**
542254	3314534	S31	SCL	84.4	76.4	69.8	65.5	18.0	5.0	4.9	4.2
542809	3313456	P6_1	SCL	96.22	87.73	76.72	70.68	18.04	5.22	5.00	4.36
551215	3315613	P11_1	SCL	84.40	79.24	72.41	72.41	21.31	5.71	5.56	4.72
-	-	**Mean**	**SCL**	**88.34**	**81.13**	**72.98**	**69.53**	**19.13**	**5.31**	**5.15**	**4.44**
-	-	**Stdev**	**SCL**	**6.82**	**5.89**	**3.48**	**3.59**	**1.88**	**0.36**	**0.37**	**0.25**
550784	3315525	S4	SL	97.9	89.1	81.0	77.6	21.7	5.8	5.8	4.8

550463	3315804	S5	SL	89.5	76.4	68.1	56.0	17.8	5.2	4.8	4.2
549355	3315721	S7	SL	101.3	93.4	80.2	81.9	20.4	5.6	5.4	4.7
548673	3315046	S8	SL	94.5	92.0	81.9	75.9	21.7	5.9	5.7	4.9
547887	3315228	S9	SL	104.7	90.6	75.0	70.7	18.3	5.2	4.9	4.2
546684	3314894	S10	SL	86.1	83.5	75.9	72.4	17.4	5.1	4.8	4.1
546434	3314814	S11	SL	84.4	75.0	69.0	67.2	18.9	5.4	5.1	4.4
544510	3314228	S15	SL	89.5	83.5	71.5	71.5	16.3	4.9	4.6	4.1
542672	3313662	S19	SL	86.1	83.5	73.3	71.5	18.5	5.3	5.1	4.3
545534	3314627	S23	SL	79.3	69.3	62.1	63.8	16.7	4.8	4.4	3.9
545513	3313165	S24	SL	76.0	65.1	69.0	68.1	17.4	4.8	4.6	3.9
550165	3315856	S26	SL	86.1	76.4	68.1	62.1	18.5	5.2	4.9	4.3
538996	3310490	S28	SL	81.0	75.0	75.0	76.7	20.2	5.5	5.4	4.5
540128	3311237	S29	SL	86.1	76.4	68.1	66.4	19.3	5.6	5.3	4.5
542626	3313867	S30	SL	79.3	75.0	64.7	64.7	18.0	5.2	4.9	4.2
542802	3313657	S32	SL	79.3	70.8	64.7	61.2	17.0	5.0	4.8	4.0
546992	3311854	S34	SL	89.5	82.1	75.0	67.2	21.3	5.8	5.6	4.8
546964	3314849	S35	SL	84.4	77.8	69.8	66.4	19.6	5.4	5.1	4.5
551762	3316701	S37	SL	87.8	80.7	69.0	86.2	17.4	4.9	4.7	4.0
549086	3315695	S39	SL	84.4	73.6	66.4	64.7	19.6	5.4	5.3	4.4
546383	3314803	S41	SL	81.0	75.0	64.7	62.9	17.8	5.2	4.8	4.2
544658	3312619	S44	SL	104.7	92.0	82.8	79.3	21.1	5.8	5.6	4.7
548033	3312191	S45	SL	69.2	62.3	57.8	62.1	17.0	4.9	4.6	4.0
548990	3313016	S46	SL	96.2	92.0	79.3	75.0	21.5	5.7	5.6	4.8
551761	3315016	S47	SL	103.0	94.8	85.3	81.0	21.3	5.8	5.6	4.8
551970	3314445	S48	SL	87.8	82.1	76.7	77.6	21.1	5.6	5.6	4.5
552525	3313144	S49	SL	81.0	76.4	74.1	71.5	21.5	5.6	5.5	4.6
547116	3311812	S50	SL	79.3	76.4	68.1	68.1	19.6	5.4	5.4	4.5
538676	3310169	P1_1	SL	97.90	99.05	81.03	81.03	21.74	5.99	5.94	5.07
538427	3310294	P2_1	SL	97.90	96.22	86.20	83.61	22.39	6.47	6.19	5.43
545410	3312106	P3_1	SL	84.40	79.24	69.82	64.65	21.52	5.64	5.44	4.78
552045	3314362	P12_1	SL	96.22	93.39	81.89	81.89	23.04	6.12	5.88	5.07
-	-	**Mean**	**SL**	**88.30**	**81.50**	**72.97**	**71.28**	**19.55**	**5.44**	**5.22**	**4.48**
-	-	**Stdev**	**SL**	**8.87**	**9.42**	**7.20**	**7.75**	**1.94**	**0.41**	**0.46**	**0.38**

X	Y	**ID**	**Texture**	**S8**	**S9**	**T10**	**T11**	**T12**	**T13**	**T14**
549622	3315727	S6	LS	3.2	2.4	9.1	9.5	9.8	9.8	9.2
546031	3314637	S13	LS	2.8	2.2	9.6	10.1	10.4	10.4	9.9
544266	3314158	S17	LS	2.5	2.0	9.7	10.2	10.5	10.6	10.0
548501	3312681	S33	LS	3.2	2.4	9.6	10.2	10.5	10.4	9.9
551302	3316141	S36	LS	3.4	2.5	9.0	9.5	9.8	9.8	9.4
552194	3314095	S38	LS	3.4	2.7	9.4	9.9	10.3	10.1	9.6
539955	3310984	S43	LS	2.8	2.2	10.1	10.6	11.1	11.1	10.5
546045	3313803	P5_1	LS	2.8	2.1	9.4	9.9	10.2	10.2	9.7
546082	3312189	P7_1	LS	3.1	2.4	9.9	10.5	10.9	10.8	10.3
549357	3313609	P8_1	LS	3.1	2.3	9.4	9.9	10.2	10.2	9.7

-	-	**Mean**	**LS**	**3.02**	**2.31**	**9.52**	**10.02**	**10.37**	**10.33**	**9.82**
-	-	**Stdev**	**LS**	**0.29**	**0.21**	**0.34**	**0.38**	**0.41**	**0.43**	**0.39**
545281	3314524	S14	S	2.6	2.0	9.4	10.0	10.4	10.3	9.8
543757	3314003	S18	S	2.7	2.1	9.8	10.4	10.7	10.7	10.1
-	-	**Mean**	**S**	**2.65**	**2.07**	**9.61**	**10.18**	**10.52**	**10.51**	**9.97**
-	-	**Stdev**	**S**	**0.09**	**0.09**	**0.26**	**0.24**	**0.24**	**0.26**	**0.22**
542254	3314534	S31	SCL	3.0	2.2	10.0	10.6	11.0	10.9	10.3
542809	3313456	P6_1	SCL	3.04	2.26	9.68	10.12	10.59	10.53	10.04
551215	3315613	P11_1	SCL	3.29	2.54	8.99	9.48	9.78	9.63	9.06
-	-	**Mean**	**SCL**	**3.10**	**2.34**	**9.56**	**10.07**	**10.44**	**10.37**	**9.81**
-	-	**Stdev**	**SCL**	**0.17**	**0.18**	**0.52**	**0.56**	**0.60**	**0.67**	**0.66**
550784	3315525	S4	SL	3.4	2.6	8.3	8.8	9.2	8.9	8.2
550463	3315804	S5	SL	3.0	2.3	8.0	8.4	8.8	8.3	7.7
549355	3315721	S7	SL	3.3	2.5	9.1	9.7	10.0	9.9	9.3
548673	3315046	S8	SL	3.5	2.6	9.4	9.9	10.2	10.3	9.8
547887	3315228	S9	SL	3.0	2.3	8.9	9.5	9.8	9.8	9.4
546684	3314894	S10	SL	2.9	2.2	9.5	10.0	10.2	10.3	9.9
546434	3314814	S11	SL	3.1	2.4	9.4	9.8	10.3	10.2	9.7
544510	3314228	S15	SL	2.9	2.1	9.9	10.4	10.8	10.8	10.2
542672	3313662	S19	SL	3.1	2.3	10.2	10.7	11.1	11.1	10.6
545534	3314627	S23	SL	2.7	2.2	9.3	9.8	10.1	10.2	9.7
545513	3313165	S24	SL	2.8	2.1	9.8	10.3	10.6	10.6	10.1
550165	3315856	S26	SL	2.9	2.2	8.2	8.7	9.0	8.7	8.0
538996	3310490	S28	SL	3.3	2.4	11.2	11.8	12.0	11.9	11.3
540128	3311237	S29	SL	3.1	2.4	10.3	10.9	11.2	11.2	10.7
542626	3313867	S30	SL	3.0	2.2	10.1	10.7	11.0	11.0	10.5
542802	3313657	S32	SL	2.8	2.2	9.7	10.2	10.5	10.6	10.2
546992	3311854	S34	SL	3.5	2.5	10.1	10.6	11.0	10.9	10.4
546964	3314849	S35	SL	3.2	2.3	9.5	10.0	10.3	10.4	9.9
551762	3316701	S37	SL	2.8	2.2	9.4	9.8	10.2	10.2	9.7
549086	3315695	S39	SL	3.2	2.4	8.8	9.3	9.6	9.6	9.1
546383	3314803	S41	SL	2.9	2.2	9.3	9.9	10.3	10.2	9.7
544658	3312619	S44	SL	3.4	2.5	10.1	10.6	11.0	11.0	10.5
548033	3312191	S45	SL	2.8	2.2	9.2	9.7	10.1	10.1	9.7
548990	3313016	S46	SL	3.5	2.6	9.5	10.1	10.4	10.3	9.8
551761	3315016	S47	SL	3.4	2.6	8.7	9.2	9.6	9.4	8.8
551970	3314445	S48	SL	3.3	2.5	9.4	10.0	10.3	10.1	9.7
552525	3313144	S49	SL	3.3	2.5	9.4	10.0	10.4	10.2	9.7
547116	3311812	S50	SL	3.2	2.4	10.0	10.5	10.9	10.8	10.3
538676	3310169	P1_1	SL	3.63	2.70	10.50	11.05	11.39	11.41	10.85
538427	3310294	P2_1	SL	3.88	2.83	11.57	12.20	12.53	12.30	11.62
545410	3312106	P3_1	SL	3.34	2.51	10.10	10.64	10.99	10.96	10.38
552045	3314362	P12_1	SL	3.63	2.77	9.43	9.88	10.27	10.12	9.62
-	-	**Mean**	**SL**	**3.17**	**2.40**	**9.58**	**10.10**	**10.45**	**10.36**	**9.83**
-	-	**Stdev**	**SL**	**0.29**	**0.19**	**0.77**	**0.79**	**0.78**	**0.84**	**0.84**

Mean radiance values were plotted with band number to evaluated what bands shows the largest differences or similitude and use them later for statistical classification. The following figure shows the variability of ASTER radiance with soil textural type in the visible and shortwave infrared regions.

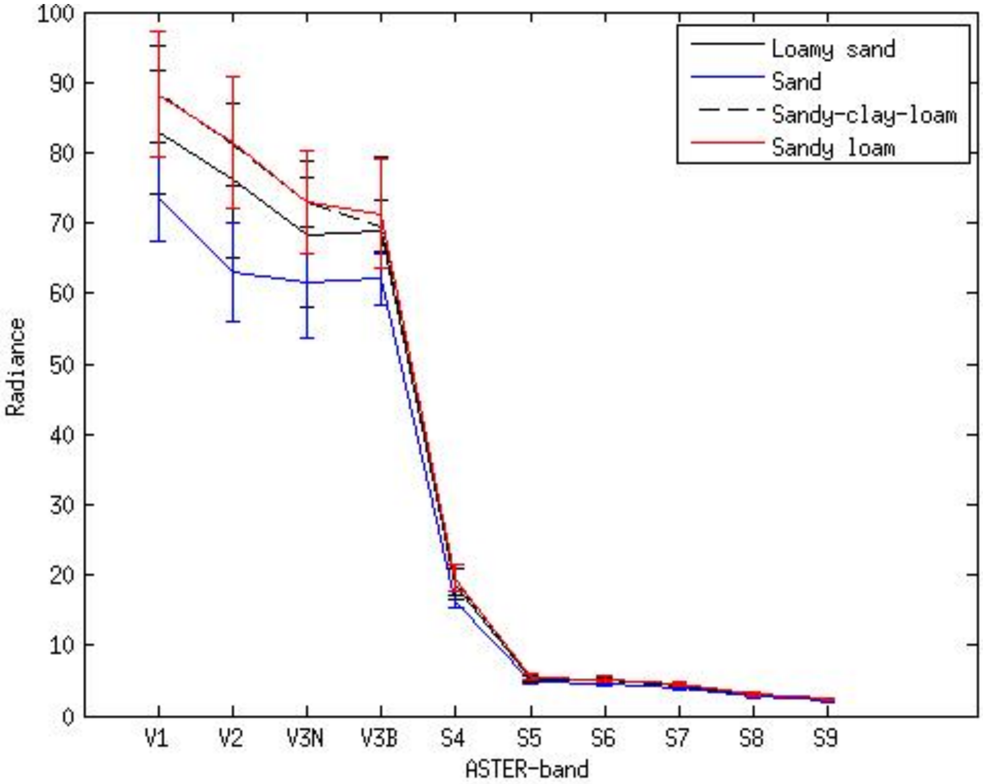

Figure D.1. Variability of ASTER Radiances With Soil Textural Classes. Larger Variations in Surface Radiance Were Found in Visible Bands (V1-V3).

The y-axis represents the value of radiance in W/m^2/sr*μm while the x-axis shows the ASTER band (V for visible regions and S for shortwave infrared). The following plot shows the variability of ASTER radiance on different textural soil types in the thermal bands. Larger differences in surface radiance among textural classes were found in the visible and near infrared region (bands 1-3) and the thermal bands (bands 12 and 13). This means that, soil textural properties have large impact in the emission of energy form the surface to the atmosphere an these differences were larger in the bands mentioned above.

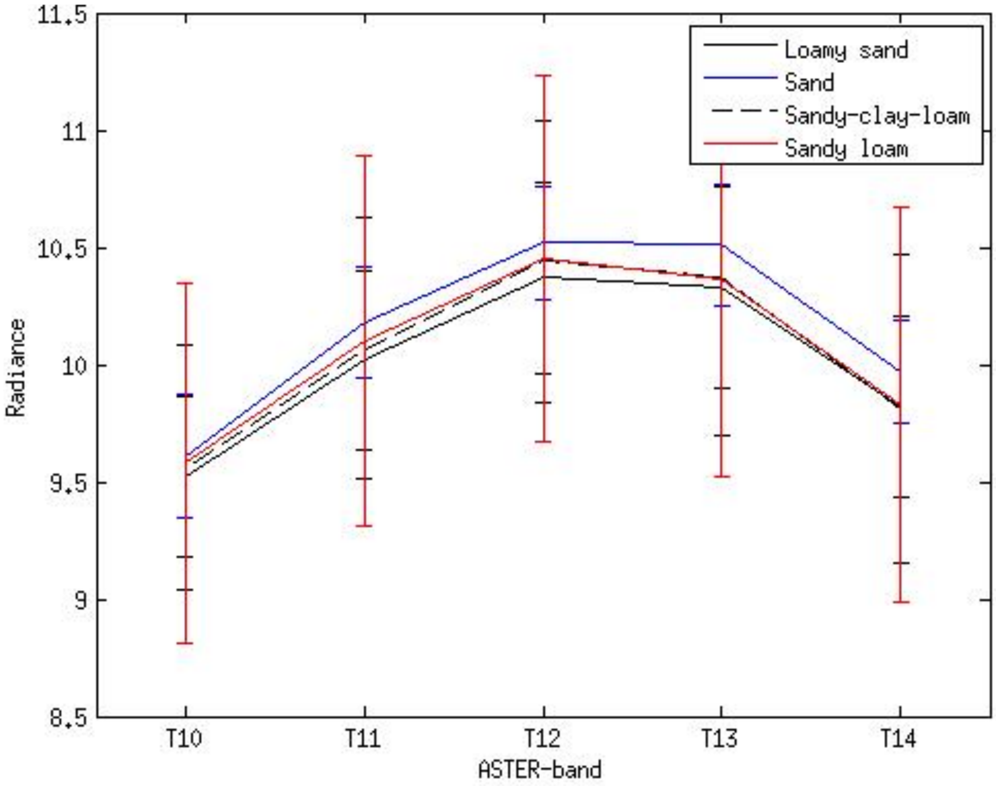

Figure D.2. Variability of ASTER Radiances With Soil Textural Classes in Thermal Bands. Larger Variations in Surface Radiance Were Found in Bands Twelve and Thirteen.

For this reason, radiance data of visible bands 1-3 and thermal bands 12 and 13 were used in a non-supervised classification algorithm to generate spatial maps of soil textural classes. These bands were used as input in clustering to determine natural groups in a multidimensional space. We utilized the isocluster method in ARCGIS 9.2 to determine class statistics. Isocluster tool can be accessed within Arctoolbox in the following way.

- Open Arctoolbox within ArcGIS 9.2 or later
- Click on Spatial Analyst tool, then click on Multivariate toolset
- Select the Isocluster tool to generate clustering statistics

The isocluster method (the initials iso are for Iterative Self Organizing) is a statistical clustering method that determines the natural grouping of pixels values in a multidimensional attribute space and stores the statistical information in a ASCII file known as signature file. Furthermore, this method is also known as modified iterative optimization clustering procedure or migrating mean technique. The algorithm separates all pixel values into a user-specified unimodal groups out of the multidimensional space or multiband raster. This statistical method is the most common used before unsupervised classification (Richards, 2013).

Finally, clustering statistical information contained in the signature file is used in the Maximum Likelihood Classification (unsupervised classification). This method is based on the Baye’s theorem of decision-making and uses the variance and covariances of the signature files to separate a raster into user defined number of classes. Maximum Likelihood Classification (MCL) approach assumes normal distribution within classes and incorporates the covariance. Then, MCL estimates the probability that a local pixel belongs to certain class (Richards, 2013).

APPENDIX E

FLOODPLAIN DELINEATION

The delineation of the floodplain in the San Miguel River Basin includes a combination of different approaches like remote sensing and previous geological data. The datasets used in the delineation include: 1) False color image s using ASTER's band 1(blue), band 2 (red) and band 3 (NIR). 2) 30-meters contour map generated form ASTER digital elevation model (DEM). 3) Geologic map from INEGI. 4) Lithology map generated from ASTER's thermal bands 10,11,12,13 and 14 according to the methods developed by Ninomiya et al. (2005). Topographic data included geologic maps from the Mexican organization INEGI (acronym in Spanish for National Institute of Statistics, Geography and Informatics) as well as 30 meters contour maps generated form ASTER's digital elevation model. In the following I will explain briefly how the floodplain for the Rio San Miguel was generated.

False-color images allow to separate very well different land features such as water bodies, vegetation, wet and dry bare soil and urban areas. I have selected a set of images during the dry season of the year 2006 in order to detect easily the riparian vegetation (natural and riparian crops) that will appears as a bright intense red color. In addition, dry sandy riverbanks will show as bright white color. The selected set of images were overpasses the region during April (15-30) 2006. Three-color composite (RGB) images were developed using band 3 =Red, band 2=Green and band 1=Blue. Figure 1, shows an example of the false color image generated with ASTER images. In the image, we can see that crops as well as riparian vegetation can be easily separated from the rest of the of the landscape.

A lithological map was created using ASTER thermal bands 10,11,12,13 and 14. Basically with these thermal bands we generated three different band ratios: 1) Carbonate Index (CI = band13/band14), 2) Quartz index (QI = band11*band11/band10*band12) and 3) Mafic index (MI = band12/band13). Finally, a composite image (RGB) was generated using QI= red, CI= green and MI = blue. Figure 2 shows the result of the compositing the band ratio values. Albeit the image has a lot of striping and noise (caused presumably by bad sensor calibration), we can clearly see differences in lithological formations. For example, the floodplain has a bluish color suggesting high presence of SiO2 (sandy soil) in contrast to surrounding landscape that mostly shows a quartz-rich material (red and reddish colors) and ultramafic material (magenta and purple). Hence, we can use this composite image to identify different geologic-soil materials that further support the delineation of the floodplain delineation.

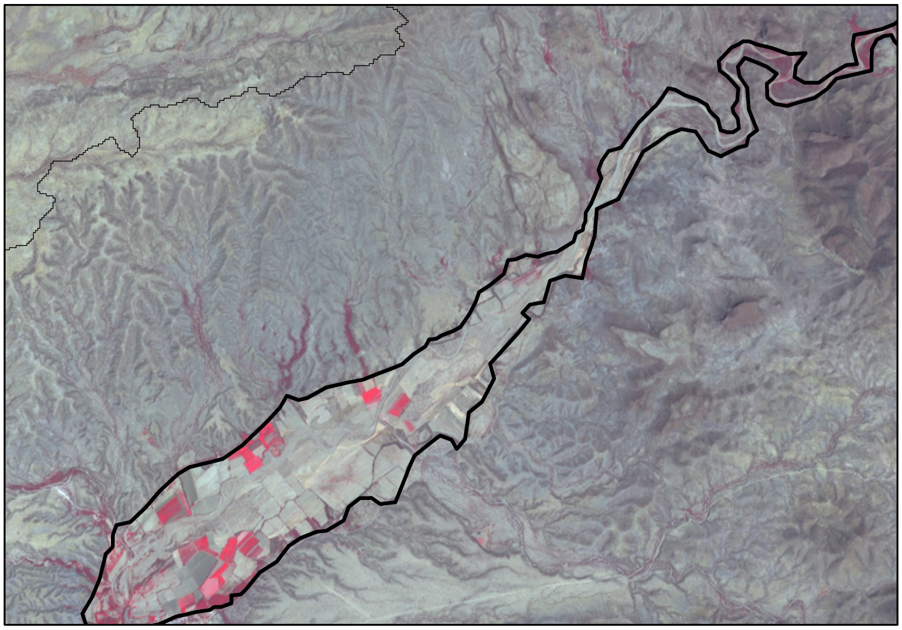

Figure E.1. Generated Floodplain Near San Miguel de Horcasitas, Sonora. The Solid Black Line Shows the Preliminary Result of The Floodplain Delineation Using a False Color Image.

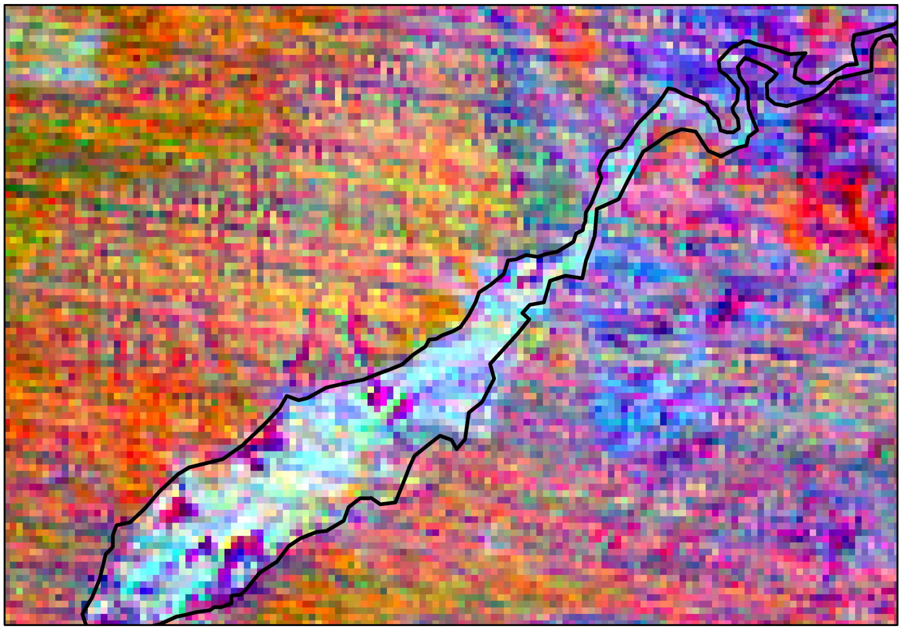

Figure E.2. Lithological Map of the Rio San Miguel Produced With ASTER's Thermal Bands. Bluish Color Suggests High Presence of SiO_2 (Sandy Soil), Red-Reddish Color Indicates Quartz-Rich Material and Magenta-Purple Color Suggests Mafic-Ultramafic Material.

Geologic maps from INEGI was used mainly to identify the spatial distribution of quaternary alluvium deposits (Qc) , as we know, these sediments are transported by fluvial processes, then we can infer the extension of the floodplain by the distribution of alluvial deposits. In addition, 30-meters contour map form ASTER digital elevation model was used to support the extension of the floodplain. Figure 3, shows the geologic-d map from INEGI overlaid by the contour map.

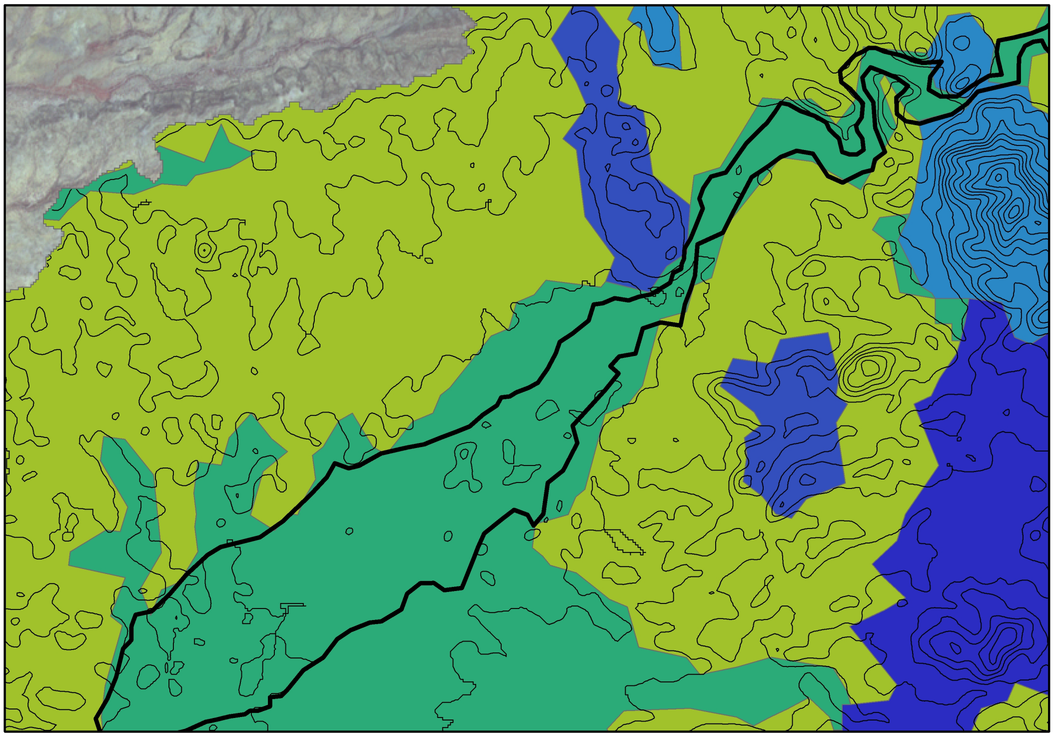

Figure E3. Geologic Map from INEGI Overlaid by 30-meters Contour Lines Generated from ASTER Digital Elevation Model.

There are some similarities between the INEGI map and the ASTER-based lithological map. However we can see discrepancies in the spatial distribution of quaternary alluvium. INEGI's map shows the alluvium deposits extending southwards while the ASTER-based map shows that this region is replaced by quartz-rich material. Although this quartz rich material can be transported by fluvial processes, it looks like it is transported from the east part of the floodplain and it is not carried by the main flood plain itself.

APPENDIX F

MODIS IMAGES PROCESSING

1) Download MODIS images from the Reverb-Echo web page:

http://reverb.echo.nasa.gov/reverb/#utf8=%E2%9C%93&spatial_map=satellite&spatial_type=rectangle

2) Install MRT software (MODIS Reprojection Tool) for Linux in the following web link:

https://lpdaac.usgs.gov/tools/modis_reprojection_tool

3) Once you have installed MRT in Ubuntu you need to put all your MODIS files in raw format .hdf in one folder. Let's assume that you have put all your files in the folder /home/lmendezb/MRT/bin. Along with the raw data files place the following files: mrtscript.sh and modis_ndvi.prm.

4) Open a terminal (Ctrl-Alt-t) and go to the folder where the files of part (2) are located. In this case is:

```
lmendezb@sese-lmendezb:~$ cd lmendez/MRT/bin
```

5) Change the permission of the mrtscript.sh folder in order to make it executable. In the terminal type the following command.

```
lmendezb@sese-lmendezb:~$ sudo chmod 755 mrscript.sh
```

5) Modify the mrtscript.sh in order to specify the input files, the output location, the mosaic information (in case you need it) and the new boundary limit for the images. In this example, the MODIS images will be mosaicked, and cut them in a smaller domain. We will process NDVI images for the year 2007. In the terminal modify the mrscript.sh with the following command.

```
lmendezb@sese-lmendezb:~$ nano mrscript.sh
```

The nano command allows modifying protected files. Change the list of files (dates) by updating the dates of the files located in the bin folder. Be sure that the resample and mosaic tools are located in the following path, /home/lmendezb/MRT/bin/resample or /home/lmendezb/MRT/bin/mrtmosaic. The upper left and lower right corner for the smaller domain will be taken from the modis_ndvi.prm file. Modify the corner if necessary.

```
=====================================================================

#!/bin/bash
# Modify the line above to the location of your BASH interpreter.

DATELIST="2006361
2007009
```

```
2007025
2007041
2007057
2007073
2007089
2007105
2007121
2007137
2007153
2007169
2007185
2007201
2007217
2007233
2007249
2007265
2007281
2007297
2007313
2007329
2007345
2007361
"
#Loop through the number of dates
for DATE in $DATELIST
do
# Collect all MODIS HDF files for a specific date
HDFFILES=$(ls MYD13Q1.A$DATE.*.hdf)
# Write these to a text file
echo $HDFFILES > mosaicinput.txt
# Run mrt mosaic and write output to HDF file (extension .hdf!)
/home/lmendezb/MRT/bin/mrtmosaic -i mosaicinput.txt -o TmpMosaic.hdf
# Call resample. Values for projection parameters are derived
# from the prm-file that was obtained using ModisTool. Input and
# output are specified using the -i and -o options.
/home/lmendezb/MRT/bin/resample -p modis_ndvi.prm -i TmpMosaic.hdf -o MYD_NDVI_$DA$
done
exit 0
======================================================================
```

6) After you modify the mrscript.sh press Ctrl-X to save the changes. Type “Yes” to agree.

7) To run the “sh” bash file, type the following instruction in the terminal.

```
lmendezb@sese-lmendezb:~$ ./mrtscript.sh
```

This process will take some time. This script transforms the native hdf format into geotiff and also mosaic and crop the original MODIS imagery.

APPENDIX G

MATLAB CODES TO TRANSFORM MODIS IMAGERY TO MODEL VEGETATION PARAMETERS

The following lines show the MATLAB code to transform MODIS-Leaf Area Index into optical transmission (kt):

```
% Read .tif files
clc
clear all;
a=dir(['/home/lmendezb/Documents/MODIS_VegPar/Input/2010/LAI/*.tif']);
[x,y] = size(a);
coeff = load('/home/lmendezb/Documents/land_use/kcoeff_1000m.txt');

% MODIS parameters
Scale_factor =0.1;
Fill_value = 255;


% 3-D matrix
% This loop reads the .tif files in the working folder and generates a 3D-matrix with NDVI values

for i=1:x
   filename=a(i).name;
A = geotiffread(filename);
F = double(A);
n = find(F>200);
F(n)= 0.5;
lai = F*Scale_factor;
B(:,:,i) = lai(:,:);
Z(:,:,i) = coeff(:,:);
kt(:,:,i) = exp(Z(:,:,i).*B(:,:,i));
%
kt(~isfinite (kt)) = -9999 ;
% %kt(:,:,i) = 0.5 * B(:,:,i);

end

% Linear interpolation of the 3-D matrix
% This function performs a linear interpolation in order to downscale from 8-days composites to daily time step. We need to include the mirt3D_mexinterp function in our working folder

[m n o] =size(kt);

t1 = kt(:,:,1:4);
t2 = kt(:,:,4:7);
t3 = kt(:,:,7:10);
t4 = kt(:,:,10:13);
t5 = kt(:,:,13:16);
t6 = kt(:,:,16:19);
t7 = kt(:,:,19:22);
t8 = kt(:,:,22:25);
t9 = kt(:,:,25:28);
t10 = kt(:,:,28:31);
```

```
t11 = kt(:,:,31:34);
t12 = kt(:,:,34:37);
t13 = kt(:,:,37:40);
t14 = kt(:,:,40:43);
t15 = kt(:,:,43:46);

% This function performs a linear interpolation in order to downscale from 8-days
composites to daily time % step. We need to include the mirt3D_mexinterp function in our
working folder

[xi,yi,zi] = meshgrid(1:n, 1:m, 1:0.126:4); % Period of 168 days for 22 images
kt1 = mirt3D_mexinterp(t15,xi,yi,zi);
[x2 y2 z2] = size(kt1);

%% File name with tRIBS format
% This part of the code generates the file name that follows thr tRIBS format

start = datenum(2010,12,03,0,0,0);
fin = datenum(2010,12,27,23,59,59);
date = datevec(start:fin);
fecha = [datestr(date,'mmddyyyyHH')];

%% Generation of ASCII files
% This loop generates the interpolated matrices as an individual files withthe tRIBS format


for k=1:z2

    name = ['OT' fecha(k,:) '.txt']
    H = kt1(:,:,k);

    % Add the names and values of the ASCII ESRI Grid format header
       fid2=fopen(['/home/lmendezb/Documents/MODIS_VegPar/Output/2010/OT/', name],'w+');
       fprintf(fid2,'%s\t %3d\n%s\t %3d\n','ncols', y2, 'nrows', x2);
       fprintf(fid2,'%s\t %10.3f\n%s\t %10.3f\n','xllcorner',505729.76,'yllcorner',3240551.66);
       fprintf(fid2,'%s\t %s\n','cellsize','1000');
       fprintf(fid2,'%s\t %s\n','NODATA_value','-9999');
       fclose(fid2);

       % Generate the files
   dlmwrite(['/home/lmendezb/Documents/MODIS_VegPar/Output/2010/OT/'
name],H,'delimiter','\t', '-append');

end
```

The following lines show the MATLAB code to transform MODIS-Leaf Area Index into canopy capacity (S):

```
% Read .tif files
clc
clear all
a=dir(['/home/lmendezb/Documents/MODIS_VegPar/Input/2010/LAI/*.tif']);
```

```
[x,y] = size(a);


%% MODIS parameters
Scale_factor =0.1;
Fill_value = 255;


%% 3-D matrix
% This loop reads the .tif files in the working folder and generates a 3D-
% matrix with NDVI values

for i=1:x
    filename=a(i).name;
A = geotiffread(filename);
F = double(A);
n = find(F==Fill_value);
F(n)=-9999;
lai = F*Scale_factor;
B(:,:,i) = lai(:,:);
kt(:,:,i) = 0.5*B(:,:,i);
%kt(:,:,i) = 0.5 * B(:,:,i);
[x y z] = size(kt);
for j=1:1:x
    for k = 1:1:y
        if kt(j,k,i) <0 %>1
            kt(j,k,i) = -9999;
        end
    end
end

end

%% Linear interpolation of the 3-D matrix
% This function performs a linear interpolation in order to downscale from 8-days
composites to daily time step. We need to include the mirt3D_mexinterp function in our
working folder
[m n o] =size(kt);

t1 = kt(:,:,1:4);
t2 = kt(:,:,4:7);
t3 = kt(:,:,7:10);
t4 = kt(:,:,10:13);
t5 = kt(:,:,13:16);
t6 = kt(:,:,16:19);
t7 = kt(:,:,19:22);
t8 = kt(:,:,22:25);
t9 = kt(:,:,25:28);
t10 = kt(:,:,28:31);
t11 = kt(:,:,31:34);
t12 = kt(:,:,34:37);
t13 = kt(:,:,37:40);
t14 = kt(:,:,40:43);
t15 = kt(:,:,43:46);
```

```
% This function performs a linear interpolation in order to downscale from 8-days
composites to daily time step. We need to include the mirt3D_mexinterp function in our
working folder

[xi,yi,zi] = meshgrid(1:n, 1:m, 1:0.126:4); % Period of 168 days for 22 images
kt1 = mirt3D_mexinterp(t15,xi,yi,zi);
[x2 y2 z2] = size(kt1);

%% File name with tRIBS format
% This part of the code generates the file name that follows thr tRIBS format

start = datenum(2010,12,03,0,0,0);
fin = datenum(2010,12,27,23,59,59);
date = datevec(start:fin);
fecha = [datestr(date,'mmddyyyyHH')];

%% Generation of ASCII files
% This loop generates the interpolated matrices as an individual files with the tRIBS
format

for k=1:z2

   name = ['CC' fecha(k,:) '.txt']
   H = kt1(:,:,k);

   % Add the names and values of the ASCII ESRI Grid format header
     fid2=fopen(['/home/lmendezb/Documents/MODIS_VegPar/Output/2010/CC/', name],'w+');
      fprintf(fid2,'%s\t %3d\n%s\t %3d\n','ncols', y2, 'nrows', x2);
      fprintf(fid2,'%s\t %10.3f\n%s\t %10.3f\n','xllcorner',505729.760,'yllcorner',3240551.660);
      fprintf(fid2,'%s\t %s\n','cellsize','1000');
      fprintf(fid2,'%s\t %s\n','NODATA_value','-9999');
      fclose(fid2);
      % Generate the files
    dlmwrite(['/home/lmendezb/Documents/MODIS_VegPar/Output/2010/CC/'
name],H,'delimiter','\t', '-append');

end
```

The following lines show the MATLAB code to transform MODIS-Leaf Area Index into Trough fall coefficient (p):

```
% Read .tif files
clc
clear all
a=dir(['/home/lmendezb/Documents/MODIS_VegPar/Input/2010/LAI/*.tif']);
[x,y] = size(a);


%% MODIS parameters
Scale_factor =0.1;
Fill_value = 255;
```

```
%% 3-D matrix
% This loop reads the .tif files in the working folder and generates a 3D-
% matrix with NDVI values

for i=1:x
    filename=a(i).name;
A = geotiffread(filename);
F = double(A);
n = find(F==Fill_value);
F(n)=-9999;
lai = F*Scale_factor;
B(:,:,i) = lai(:,:);
kt(:,:,i) = exp(-1.467*B(:,:,i));

kt(~isfinite (kt)) = -9999 ;
%kt(:,:,i) = 0.5 * B(:,:,i);
end

%% Linear interpolation of the 3-D matrix
% This function performs a linear interpolation in order to downscale from 8-days
composites to daily time step. We need to include the mirt3D_mexinterp function in our
working folder
[m n o] =size(kt);

t1 = kt(:,:,1:4);
t2 = kt(:,:,4:7);
t3 = kt(:,:,7:10);
t4 = kt(:,:,10:13);
t5 = kt(:,:,13:16);
t6 = kt(:,:,16:19);
t7 = kt(:,:,19:22);
t8 = kt(:,:,22:25);
t9 = kt(:,:,25:28);
t10 = kt(:,:,28:31);
t11 = kt(:,:,31:34);
t12 = kt(:,:,34:37);
t13 = kt(:,:,37:40);
t14 = kt(:,:,40:43);
t15 = kt(:,:,43:46);

% This function performs a linear interpolation in order to downscale from 8-days
composites to daily time step. We need to include the mirt3D_mexinterp function in our
working folder

[xi,yi,zi] = meshgrid(1:n, 1:m, 1:0.126:4); % Period of 168 days for 22 images
kt1 = mirt3D_mexinterp(t15,xi,yi,zi);
[x2 y2 z2] = size(kt1);

%% File name with tRIBS format
% This part of the code generates the file name that follows thr tRIBS format

start = datenum(2010,12,03,0,0,0);
fin = datenum(2010,12,27,23,59,59);
date = datevec(start:fin);
```

```
fecha = [datestr(date,'mmddyyyyHH')];

%% Generation of ASCII files
% This loop generates the interpolated matrices as an individual files withthe tRIBS format

for k=1:z2

    name = ['TF' fecha(k,:) '.txt']
    H = kt1(:,:,k);

    % Add the names and values of the ASCII ESRI Grid format header
%       fid2=fopen(name,'w+');
       fid2=fopen(['/home/lmendezb/Documents/MODIS_VegPar/Output/2010/TF/', name],'w+');
       fprintf(fid2,'%s\t %3d\n%s\t %3d\n','ncols', y2, 'nrows', x2);
       fprintf(fid2,'%s\t %10.3f\n%s\t %10.3f\n','xllcorner',505729.760,'yllcorner',3240551.660);
       fprintf(fid2,'%s\t %s\n','cellsize','1000');
       fprintf(fid2,'%s\t %s\n','NODATA_value','-9999');
       fclose(fid2);
       % Generate the files
dlmwrite(['/home/lmendezb/Documents/MODIS_VegPar/Output/2010/TF/' name],H,'delimiter','\t',
'-append');
  %dlmwrite(['/media/WD_VIV1/SONORA_NLDAS/2005/Nr/' newFileName],V_r,'delimiter','\t', '-
append');
end
```

The following lines show the MATLAB code to convert raw MODIS albedo data into white sky short-wave albedo

```
%% Read albedo.tif files
clc
clear all
a=dir(['/home/lmendezb/Documents/MODIS_VegPar/Input/2010/albedo/*.tif']);
[x,y] = size(a);


%% MODIS parameters
Scale_factor =0.001;
Fill_value = 32767;


%% 3-D matrix
% This loop reads the .tif files in the working folder and generates a 3D-
% matrix with NDVI values

for i=1:x
    filename=a(i).name;
A = geotiffread(filename);
F = double(A);
n = find(F==Fill_value);
F(n)=-9999;
z = F<0;
```

```
F(z)=-9999;
alb = F*Scale_factor;
B(:,:,i) = alb(:,:);
end

[x3,y3,z3] = size(B);
%% Linear interpolation of the 3-D matrix
% This function performs a linear interpolation in order to downscale from 8-days composites to
daily time step. We need to include the mirt3D_mexinterp function in our working folder

t1 = B(:,:,1:4);
t2 = B(:,:,4:7);
t3 = B(:,:,7:10);
t4 = B(:,:,10:13);
t5 = B(:,:,13:16);
t6 = B(:,:,16:19);
t7 = B(:,:,19:22);
t8 = B(:,:,22:25);
t9 = B(:,:,25:28);
t10 = B(:,:,28:31);
t11 = B(:,:,31:34);
t12 = B(:,:,34:37);
t13 = B(:,:,37:40);
t14 = B(:,:,40:43);
t15 = B(:,:,43:46);


[xi,yi,zi] = meshgrid(1:y3, 1:x3,1:0.126:4); %
B1 = mirt3D_mexinterp(t15,xi,yi,zi);
[x2 y2 z2] = size(B1);

%% File name with tRIBS format
% This part of the code generates the file name that follows thr tRIBS format

start = datenum(2010,12,03,0,0,0);
fin = datenum(2010,12,27,23,59,59);
date = datevec(start:fin);
fecha = [datestr(date,'mmddyyyyHH')];

%% Generation of ASCII files
% This loop generates the interpolated matrices as an individual files with the tRIBS
format

for k=1:z2

    name = ['ALB' fecha(k,:) '.txt']
    H = B1(:,:,k);

    % Add the names and values of the ASCII ESRI Grid format header
      fid2=fopen(['/home/lmendezb/Documents/MODIS_VegPar/Output/2010/albedo/', name],'w+');
       fprintf(fid2,'%s\t %3d\n%s\t %3d\n','ncols', y2, 'nrows', x2);
       fprintf(fid2,'%s\t %10.3f\n%s\t %10.3f\n','xllcorner',505729.760,'yllcorner',3240551.660);
       fprintf(fid2,'%s\t %s\n','cellsize','1000');
       fprintf(fid2,'%s\t %s\n','NODATA_value','-9999');
       fclose(fid2);
```

```
      % Generate the files
     dlmwrite(['/home/lmendezb/Documents/MODIS_VegPar/Output/2010/albedo/'
name],H,'delimiter','\t', '-append');

end
```

The following lines show the MATLAB code to transform MODIS-Normalized Difference Vegetation Index into vegetation fraction (vf)

```
% Read .tif files
clc
clear all
a=dir(['/home/lmendezb/Documents/MODIS_VegPar/Input/2010/NDVI/*.tif']);
[x,y] = size(a);

% MODIS parameters
Scale_factor =0.0001;
Fill_value = -3000;

%% 3-D Matrix
% This loop reads the .tif files in the working folder, generates a 3D-and calculates the
NDVI values.

for i=1:x
    filename=a(i).name;
A = geotiffread(filename);
F = double(A);
n = find(F==Fill_value);
F(n)=NaN;
u = find(F<0);
F(u)=0;
ndvi = F*Scale_factor;
B(:,:,i) = ndvi(:,:);
end

[x3,y3,z3] = size(B);

%% I have calculated the maximum and minimum for all years (2010 to 2010 including
2006 and 2007) %and the values were
%NDVImax =0.9977 (2010) y NDVImin=0
NDVIMAX = 0.9977;
NDVIMIN = 0;
DeltaNDVI = NDVIMAX-NDVIMIN;

% Estimation of VF
vf = ((B-NDVIMIN)./DeltaNDVI).^2;
nan_locations = find(isnan(vf));
vf(nan_locations)=-9999;

t1 = vf(:,:,1:4);
t2 = vf(:,:,4:7);
```

```
t3 = vf(:,:,7:10);
t4 = vf(:,:,10:13);
t5 = vf(:,:,13:16);
t6 = vf(:,:,16:19);
t7 = vf(:,:,19:22);
t8 = vf(:,:,22:23);


%% Linear interpolation of the 3-D matrix
% This function performs a linear interpolation in order to downscale from 16-days
composites to daily time step. We need to include the mirt3D_mexinterp function in our
working folder



[xi,yi,zi] = meshgrid(1:y3, 1:x3, 1:0.063:4); % Period of 48 days for 4 images
vf1 = mirt3D_mexinterp(t8,xi,yi,zi);
[x2 y2 z2] = size(vf1);


% %% File name with tRIBS format
% % This part of the code generates the file name that follows thr tRIBS format

start = datenum(2010,12,03,0,0,0);
fin = datenum(2010,12,18,23,59,59);
date = datevec(start:fin);
fecha = [datestr(date,'mmddyyyyHH')];

%% Generation of ASCII files
% This loop generates the interpolated matrices as an individual files withthe tRIBS format

for k=1:z2

   name = ['VF' fecha(k,:) '.txt']
   H = vf1(:,:,k);

   % Add the names and values of the ASCII ESRI Grid format header
     fid2=fopen(['/home/lmendezb/Documents/MODIS_VegPar/Output/2010_VF/', name],'w+');
     fprintf(fid2,'%s\t %3d\n%s\t %3d\n','ncols', y2, 'nrows', x2);
     fprintf(fid2,'%s\t %10.3f\n%s\t %10.3f\n','xllcorner',505729.76,'yllcorner',3240551.66);
     fprintf(fid2,'%s\t %s\n','cellsize','250');
     fprintf(fid2,'%s\t %s\n','NODATA_value','-9999');
     fclose(fid2);
     % Generate the files
   dlmwrite(['/home/lmendezb/Documents/MODIS_VegPar/Output/2010_VF/'
name],H,'delimiter','\t', '-append');

end
```

The following lines show the MATLAB code to transform MODIS-Leaf Area Index into empirical stomatal resistance (rs)

```
%% Read lai.tif files
clc
clear all
a=dir(['/media/TX_Drive/DYN_SLL/lai/kt/*.tif']);
[x,y] = size(a);


%% MODIS parameters
Scale_factor =0.1;
Fill_value = 255;


%% 3-D matrix
% This loop reads the .tif files in the working folder and generates a 3D-
% matrix with NDVI values

for i=1:x
   filename=a(i).name;
A = geotiffread(filename);
F = double(A);
n = find(F==Fill_value);
F(n)=-99990;
lai = F*Scale_factor;
B(:,:,i) = lai(62:216,20:149);
end

%% Linear interpolation of the 3-D matrix
% This function performs a linear interpolation in order to downscale from 8-days
composites to daily time step. We need to include the mirt3D_mexinterp function in our
working folder

[xi,yi,zi] = meshgrid(1:130, 1:155, 1:0.125:8); % Period of 168 days for 22 images
B1 = mirt3D_mexinterp(B,xi,yi,zi);
[x2 y2 z2] = size(B1);

%% Read f_par.tif files
a=dir(['/media/TX_Drive/DYN_SLL/fpar/f_par/*.tif']);
[x,y] = size(a);


%% MODIS parameters
Scale_factor =0.01;
Fill_value = 255;


%% 3-D matrix
% This loop reads the .tif files in the working folder and generates a 3D-
% matrix with NDVI values

for i=1:x
   filename=a(i).name;
A = geotiffread(filename);
F = double(A);
n = find(F==Fill_value);
```

```
F(n)=-999900;
fpar = F*Scale_factor;
C(:,:,i) = fpar(62:216,20:149);
end

%% Linear interpolation of the 3-D matrix
% This function performs a linear interpolation in order to downscale from 8-days
composites to daily time step. We need to include the mirt3D_mexinterp function in our
working folder

[xi,yi,zi] = meshgrid(1:130, 1:155, 1:0.125:8); % Period of 168 days for 22 images
C1 = mirt3D_mexinterp(C,xi,yi,zi);
[x2 y2 z2] = size(C1);

%% Prepare ISWR from NLDAS

n = dir(['/media/TX_Drive/NLDAS_2004/Nr/*.txt']);

for i=5390:24:6734  %14:00 from 4/22 to 10/06/2004
    filename=n(i).name;
    [a1 a2 a3 a4 a5 a6 a7 a8 a9 a10]=textread(filename,'%f %f %f %f %f %f %f %f %f
%f','headerlines',6);
    nldas(:,:,(i-2702)/24+1)=[a1 a2 a3 a4 a5 a6 a7 a8 a9 a10];
    nldas1(:,:,(i-2702)/24+1) = resizem(nldas(:,:,(i-2702)/24+1),[155 130],'nearest');
end

%% Calculate rs with LAI, F-PAT and ISWR from NLDAS
s=113
e=168
for i=s:1:e
    rs(:,:,i)= ((((nldas1(:,:,i)*0.45*4.6).*C1(:,:,(i-s+1))+80)/34.16)./(nldas1(:,:,i).*C1(:,:,(i-
s+1))*0.45*4.6))./B1(:,:,(i-s+1))*1000;
    for j=1:1:155
        for k =1:1:130
            if rs(j,k,i)>1000
                rs(j,k,i)=-9999;
            end
        end
    end
end



%% File name with tRIBS format
% This part of the code generates the file name that follows thr tRIBS format

start = datenum(2004,8,13,0,0,0);
fin = datenum(2004,10,6,23,59,59);
date = datevec(start:fin);
fecha = [datestr(date,'mmddyyyyHH')];

%% Generation of ASCII files
% This loop generates the interpolated matrices as an individual files withthe tRIBS format

for k=1:1:(e-s+1)
```

```
    name = ['RS' fecha(k,:) '.txt']
    H = rs(:,:,(k+s-1));

    % Add the names and values of the ASCII ESRI Grid format header
      fid2=fopen(name,'w+');
      fprintf(fid2,'%s\t %3d\n%s\t %3d\n','ncols', y2, 'nrows', x2);
      fprintf(fid2,'%s\t %10.3f\n%s\t %10.3f\n','xllcorner',503451,'yllcorner',3265266);
      fprintf(fid2,'%s\t %s\n','cellsize','926.625');
      fprintf(fid2,'%s\t %s\n','NODATA_value','-9999');
      fclose(fid2);
      % Generate the files
    dlmwrite(name,H,'delimiter','\t', '-append')

end
```

APPENDIX H

EDDY COVARIANCE PROCESSING AND FLUX CORRECTIONS

The software required for high frequency processing of eddy-covariance data is EddyPro®. This software was developed by Licor and can be downloaded at:

http://www.licor.com/env/products/eddy_covariance/software.html

EddyPro® is compatible with Windows. There are no versions for Linux or mac. Ubuntu users can run this application on a virtual machine.

1. PROJECT CREATION

Open project: C:/Desktop/Raw_data/encino_test. There is a another file for Rayon site (rayon_test).

Select the Input raw data as TOB1. The binary format TOB1 is often used for storing raw data obtained from Campbell Scientific® dataloggers. These files are customizable, as one can select the format of each individual variable (e.g. integer, single precision, etc.).

Chose the Metadata file (encino_test.metadata). This file contains the physical characteristics of towers and the sensors.

Set up the acquisition frequency in 20Hz although some towers could sample at 10Hz.

Canopy height: 9m

Displacement height: 6.03m

Roughness length: 1.03

Altitude: 1300-m (Elevation of the Encino site).

Lat Long: 29 57'36", 110 27'36" (location of the Encino site).

2. BASIC SETTINGS

Raw data format: TOB1_2310.ts_data_yyyy_mm_dd_HHMM.dat

Anemometer: CSAT-3

Sensor of for CO2 and H2O are available.

3. ADVANCE SETTINGS

Rotation method: Planar fit (Wilczak et al., 2001)

Detrend Method: Block average

Time lag detection method: covariance maximization with default

Quality check: Mauder and Foken, 2004

Footprint method; Kljun et al., 2004

Compensation for density fluctuations: Webb et al 1980 (open path)

3.1 SPECTRAL CORRECTIONS

Low pass filtering: Moncrieff et al., 1997

High pass fileting Moncrieff et al., 2004

3.2 STATISTICAL ANALYSIS

It includes spike count removal, Amplitude resolution, absolute limits and skewness-kurtosis

4. OUTPUT

Results according to the AmeriFlux format.

Metadata

APPENDIX I

MODEL SET UP AND DATA

This appendix show the location of the files used for the hydrological simulations. All the files and folder are stored in the hard drive “FreeAgent_2Tb”.

FOLDER	DESCRIPTION
Simulations_Luis	This folder contains the model setup as well as a modified version of tRIBS. Model modifications include the improvement in reading NLDAS and reduced number of outputs. This folder also contains the hydro-meteorological data use for the calibration and validation of the model
Rayon2004	Contains the point scale simulation at the Rayon EC tower during the summer season 2004. This folder contains model set up, outputs, observations and MATLAB codes to visualize outputs
Rayon2006	Contains the point scale simulation at the Rayon EC tower during the summer season 2006. This folder contains model set up, outputs, observations and MATLAB codes to visualize outputs
Rayon2007	Contains the point scale simulation at the Rayon EC tower during the summer season 2007. This folder contains model set up, outputs, observations and MATLAB codes to visualize outputs
Rayon2008	Contains the point scale simulation at the Rayon EC tower during the summer season 2008. This folder contains model set up, outputs, observations and MATLAB codes to visualize outputs
Rayon2009	Contains the point scale simulation at the Rayon EC tower during the summer season 2009. This folder contains model set up, outputs, observations and MATLAB codes to

	visualize outputs
SLLocos2008	Contains the point scale simulation at the Sierra Los Locos EC tower during the summer season 2008. This folder contains model set up, outputs, observations and MATLAB codes to visualize outputs
SLLocos2009	Contains the point scale simulation at the Sierra Los Locos EC tower during the summer season 2009. This folder contains model set up, outputs, observations and MATLAB codes to visualize outputs
SLL_Tiantian	Contains the catchment scale simulation at Sierra Los Locos during the summer season 2004, based on the previous work of Xian et al. 2014. This folder contains model set up, outputs, observations and MATLAB codes to visualize outputs. It also contains the different soil thickness and soil texture data.
Sites	Contains the rainfall data for the Hydrometeorological Network in Sonora. Dataset ranges from 2004 to 2010.
EC_Observations	Contains the processed EC data from the Rayon and the Encino towers in Sonora. Dataset ranges from 2004 to 2010 for Rayon and 2008 to 2010 for Encino.